AFRL-RW-EG-TR-2012-096

Efficient Cryosolid Positron Moderators

Mario E. Fajardo
C. Michael Lindsay
Christopher D. Molek

Air Force Research Laboratory
Munitions Directorate/Ordnance Division
Energetic Materials Branch (AFRL/RWME)
Eglin AFB, FL 32542-5910

August 2012

Final Report

Distribution A: Approved for public release; distribution unlimited. Approval Confirmation: 96 ABW/PA # 96ABW-2012-0348, dated September 6, 2012

AIR FORCE RESEARCH LABORATORY, MUNITIONS DIRECTORATE

Air Force Materiel Command ■ United States Air Force ■ Eglin Air Force Base

NOTICE AND SIGNATURE PAGE

AFRL-RW-EG-TR-2012-096 HAS BEEN REVIEWED AND IS APPROVED FOR PUBLICATION IN ACCORDANCE WITH ASSIGNED DISTRIBUTION STATEMENT.

FOR THE DIRECTOR:

WHITE.HOWAR
D.G.1230779062
Digitally signed by
WHITE.HOWARD.G.1230779062
DN: c=US, o=U.S. Government,
ou=DoD, ou=PKI, ou=USAF,
cn=WHITE.HOWARD.G.1230779062
Date: 2012.09.10 08:07:56 -05'00'

HOWARD G. WHITE, PhD
Technical Advisor
Ordnance Division

VARNER.CHRISTO
PHER.L.126566454
3
Digitally signed by
VARNER.CHRISTOPHER.L.1265664543
DN: c=US, o=U.S. Government, ou=DoD,
ou=PKI, ou=USAF,
cn=VARNER.CHRISTOPHER.L.1265664543
Date: 2012.09.07 07:02:53 -05'00'

CHRISTOPHER L. VARNER
Branch Chief
Energetic Materials Branch

FAJARDO.MARI
O.E.1230489889
Digitally signed by
FAJARDO.MARIO.E.1230489889
DN: c=US, o=U.S. Government, ou=DoD,
ou=PKI, ou=USAF,
cn=FAJARDO.MARIO.E.1230489889
Date: 2012.09.07 06:58:15 -05'00'

MARIO E. FAJARDO, PhD
Project Manager
Energetic Materials Branch

This page intentionally left blank

REPORT DOCUMENTATION PAGE	*Form Approved* *OMB No. 0704-0188*

1. REPORT DATE *(DD-MM-YYYY)* 08-2012	**2. REPORT TYPE** Final	**3. DATES COVERED** *(From - To)* 1 October 2005 – 1 August 2012

4. TITLE AND SUBTITLE

Efficient Cryosolid Positron Moderators

5a. CONTRACT NUMBER

5b. GRANT NUMBER

5c. PROGRAM ELEMENT NUMBER
62602F

6. AUTHOR(S)

Mario E. Fajardo, C. Michael Lindsay, Christopher D. Molek

5d. PROJECT NUMBER
2502

5e. TASK NUMBER
10

5f. WORK UNIT NUMBER
15

7. PERFORMING ORGANIZATION NAME(S) AND ADDRESS(ES)

Air Force Research Laboratory
Munitions Directorate
Ordnance Division
Energetic Materials Branch
Eglin AFB, FL 32542-5910

8. PERFORMING ORGANIZATION REPORT NUMBER

AFRL-RW-EG-TR-2012-096

9. SPONSORING / MONITORING AGENCY NAME(S) AND ADDRESS(ES)

Air Force Research Laboratory, Munitions Directorate
Ordnance Division
Energetic Materials Branch (AFRL/RWME)
Eglin AFB FL 32542-5910
Technical Advisor: Dr. Jennifer L. Jordan

10. SPONSOR/MONITOR'S ACRONYM(S)
AFRL-RW-EG

11. SPONSOR/MONITOR'S REPORT NUMBER(S)
AFRL-RW-EG-TR-2012-096

12. DISTRIBUTION / AVAILABILITY STATEMENT

Distribution A: Submitted for public release; distribution unlimited. Approval Confirmation 96 ABW/PA # 96ABW-2012-0348, dated September 6, 2012

13. SUPPLEMENTARY NOTES

DISTRIBUTION STATEMENT INDICATING AUTHORIZED ACCESS IS ON THE COVER PAGE AND BLOCK 12 OF THIS FORM.

14. ABSTRACT

This report documents an in-house experimental effort to improve upon the $\varepsilon \sim 1\%$ efficiency of state-of-the-art cryogenic solid neon positron moderators. We detail our rationale for why we expected an order-of-magnitude higher positron moderation efficiency from Rapid Vapor Deposited cryogenic parahydrogen solids. We describe our integration of a Matrix Isolation Spectroscopy capability into our Positron Moderation apparatus, which enables spectroscopic characterization of the cryogenic moderators. Despite all our hopes and expectations to the contrary, solid parahydrogen is not a positron moderator. Indeed, a ≈ 15-nm-thick layer of solid normal hydrogen is sufficient to kill half the flux of slow positrons emerging from a working solid neon moderator. We also report results from experiments on other rare gas solid positron moderators, on moderators overcoated with layers of other molecular solids, and on moderators containing deliberately included isolated dopants. We present our methods and data in great detail to facilitate the continuation and extension of these experiments by other researchers.

15. SUBJECT TERMS

positron moderation, matrix isolation spectroscopy, cryogenic solid, ,rapid vapor deposition, solid parahydrogen

16. SECURITY CLASSIFICATION OF:			**17. LIMITATION OF ABSTRACT**	**18. NUMBER OF PAGES**	**19a. NAME OF RESPONSIBLE PERSON**
					Mario E. Fajardo
a. REPORT	**b. ABSTRACT**	**c. THIS PAGE**			**19b. TELEPHONE NUMBER** *(include area code)*
UNCLASSIFIED	UNCLASSIFIED	UNCLASSIFIED	UL	105	850-882-9067

Standard Form 298 (Rev. 8-98)
Prescribed by ANSI Std. Z39.18

This page intentionally left blank

PREFACE

This report was prepared at the Energetic Materials Branch (AFRL/RWME) of the Air Force Research Laboratory, Ordnance Division, Munitions Directorate, Eglin Air Force Base, Florida 32542-5910.

ACKNOWLEDGEMENTS

We gratefully acknowledge the technical inspiration and hands-on assistance of Mr. Kenneth M. Edwards at the inception of this project.

We also thank Profs. A.P. Mills Jr., K.G. Lynn, C.M. Surko, and D.M. Schrader for their patient explanations and helpful conversations. Any remaining misconceptions are the fault of the Authors.

We also express our gratitude to our colleagues as follows:

Mr. William Harrison, Mr. Chuck Thames, Mr. Aaron Howell, and Mr. Roy Larsen for infrastructure and equipment support.

Mrs. Karen Clayton for administrative support.

Mr. Byron Allmon for critical administrative support in the areas of formatting, editing, collating and publishing of the technical report.

Mr. Mac Belton for financial tracking.

This page intentionally left blank

TABLE OF CONTENTS

TABLE OF CONTENTS (continued)

Section **Title** **Page**

LIST OF FIGURES

LIST OF FIGURES (continued)

LIST OF FIGURES (continued)

LIST OF TABLES

Table **Title** **Page**

LIST OF ACRONYMS

ALARA	as low as reasonably achievable
ALI	annual limit of intake
CEM	channel electron multiplier
FTIR	fourier transform IR
HEDM	high energy density matter
HPGe	high purity germanium
KE	kinetic energies
KED	kinetic energy distribution
MIS	matrix isolation spectroscopy
PIRAS	polarized IR absorption spectroscopy
RPA	retarding potential analyzer
RVD	rapid vapor deposition
UHV	ultrahigh vacuum
SS	stainless steel
VUV	vacuum ultraviolet

This page intentionally left blank

1. INTRODUCTION

1.A. Positrons

The positron (e^+) is the antimatter counterpart to the electron (e^-) [1-4]. It has the same rest mass (m_e) and intrinsic spin (½) as the electron, but it carries an opposite (positive) electrical charge. Positrons are inherently stable particles and do not decay in isolation; however, any positron which finds itself in our normal matter world will quickly annihilate with one of the many readily available electrons, converting the combined positron+electron mass into energy. This energy usually appears as gamma radiation (photons), with the sum of the gamma ray energies (measured in the center-of-mass rest frame) given by $E = 2\, m_e\, c^2 \approx 1.02$ MeV.

Positrons are used routinely in dozens of laboratories worldwide as the basis of a number of diagnostic techniques for characterizing a wide variety of materials [1-3]. The gamma rays emitted by electron-positron annihilation encode a wealth of information about the environment in which the annihilation process takes place. Positrons tend to scatter from, and localize and annihilate at, defects in materials. Since voids and other defects in energetic materials (*e.g.* explosives) are postulated to serve as "hot spots" influencing initiation sensitivities [5], positron-based diagnostics may prove valuable in the development and evaluation of new insensitive energetic materials. This application provides a near term payoff for our investments in improving our ability to produce and control positrons.

An intriguing mid-term payoff is described in proposals for an electron-positron stimulated annihilation tabletop gamma ray laser [6-13]. One scheme begins with the production and cooling of positronium "atoms" (Ps, a bound electron-positron pair) in a sub-micron cavity in an insulating material. At sufficiently high concentrations and low temperatures, some of the surviving positronium atoms are expected to form a Bose-Einstein condensate; a necessary first step towards stimulated annihilation. The recent successful demonstration of the production of di-positronium (Ps_2) [13] bodes well for this effort.

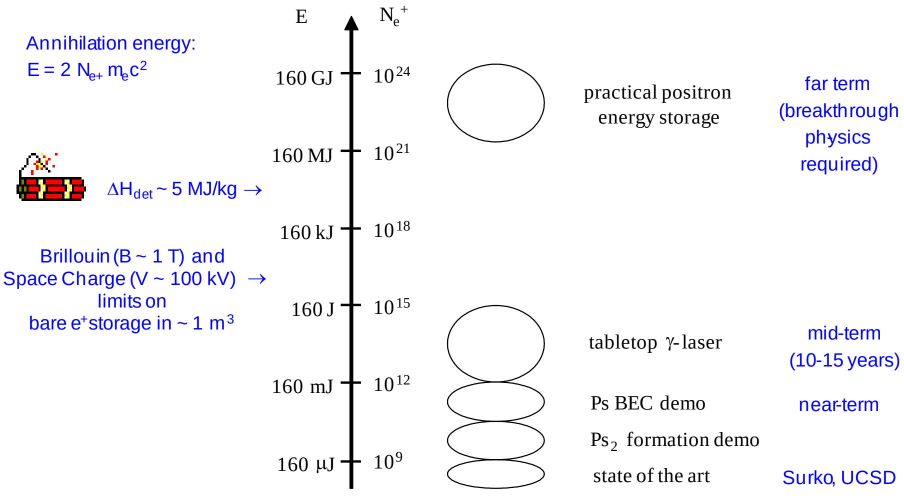

e^+ = positron; Ps = positronium (e^+/e^- bound pair);

Figure 1. Reality check c2003

Finally, the energy density available from electron-positron annihilation is simply astonishing: $E/m_e = 2\,c^2 \approx 1.8\text{x}10^{17}$ J/kg = 180 MJ/μg; which is more than ten orders of magnitude larger than the energy densities of chemical explosives or propellants (!) [5]. Since this annihilation energy is released primarily as low energy gamma rays, in a manner which does not produce any radioactive waste or induce secondary radioactivity in the surroundings, it is especially attractive for future munitions, propulsion, and power applications [4].

However, as depicted in Figure 1, we recognize that many (over a dozen) orders-of-magnitude improvements in our ability to produce, manipulate, and store antimatter will be required before practical antimatter energy storage becomes a reality. This will require the discovery of new approaches to positron production and storage [14-16], and we expect that any such applications lay many decades (if not centuries) in the future. This Report describes our (unsuccessful) effort to provide one of those dozen order-of-magnitude improvements.

1.B. Positron Moderation

As shown in Figure 2, positrons are produced in the laboratory by either: (a) electron-positron pair production in high atomic number targets bombarded by energetic electrons, or (b) β^+ decay of radioisotopes such as ^{22}Na [1]. Both approaches produce fast positrons with a wide range of kinetic energies (KEs), typically several hundred keV. An integral step in every low energy positron trapping scheme is the “moderation” or slowing down of the fast nascent positrons to KEs ~ 1 eV [1]. Tightening up the positron kinetic energy distribution (KED) is required so that the electromagnetic fields employed in subsequent manipulation and trapping steps act upon all positrons as equally as possible. We note that electromagnetic trapping of positrons as a non-neutral single component plasma is problematic, with the energy invested in the trapping fields necessarily always exceeding the rest mass energy of the trapped positrons [14-16]. These limitations have motivated considerable interest in novel approaches to stabilize and trap electrically neutral positronium atoms in crossed electric and magnetic fields [17-19].

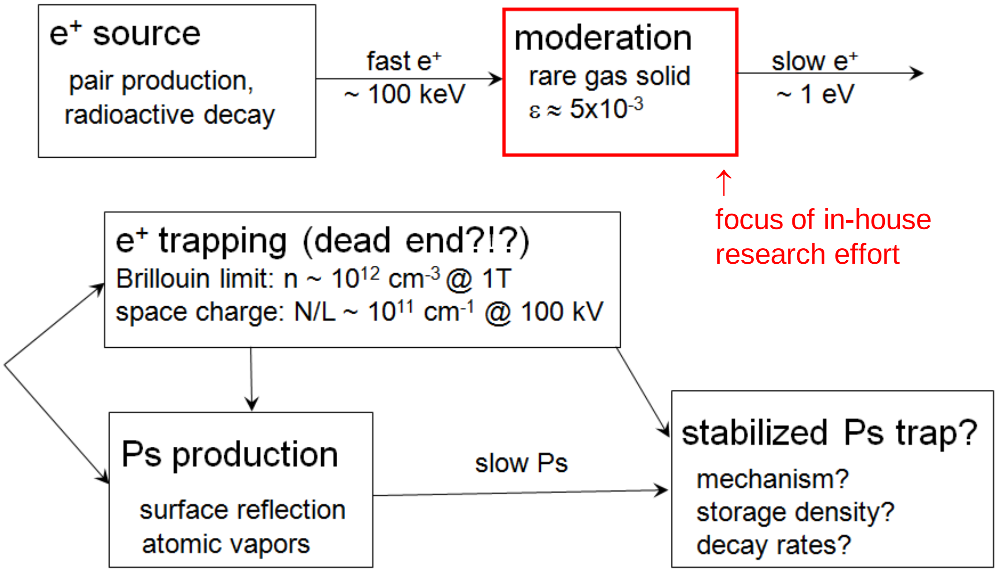

Figure 2. Generic positron production/moderation/storage scheme

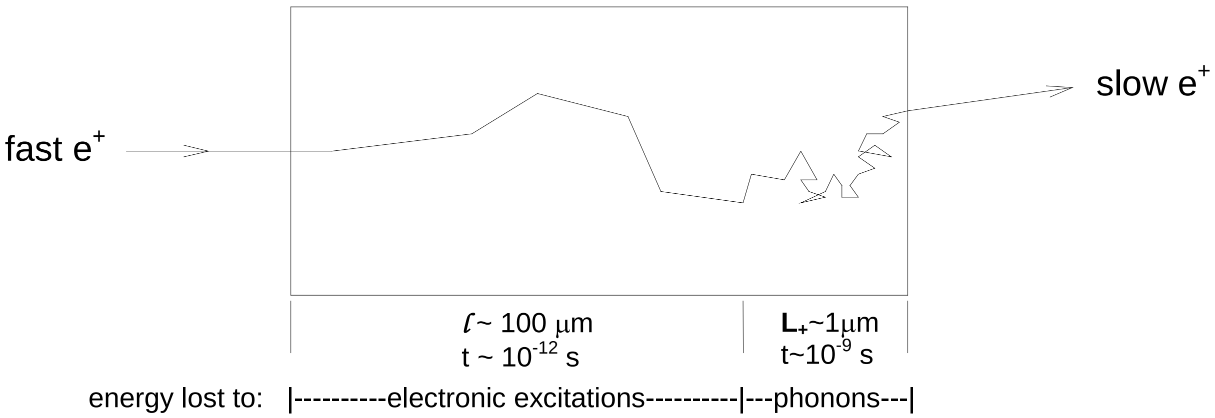

Figure 3. Positron moderation physics cartoon

We decided early on to narrow the scope of this in-house research project to improving the efficiency of the positron moderation step. The best positron moderators presently known are thin cryogenic rare gas solid films [20-26]; efficiencies of $\varepsilon \sim 1$ % have been demonstrated for solid neon (Ne) -- the other 99 % of the nascent fast positrons are wasted. As shown in Figure 3, fast positrons rapidly lose most of their KE in any material by inelastic collisions producing ionization and electronic excitations. However, in an insulator such as solid Ne, such events become impossible when the positron KE drops below a threshold energy comparable to the valence/conduction band gap [22]. The resulting “epithermal” positrons can only lose energy *via* the relatively inefficient creation of phonons (lattice vibrations), leading to a period of “hot diffusion” during which they can travel a distance $L_+ \sim 1$ μm [1]. Positrons that approach the surface of the solid with sufficient energy to overcome the moderator’s positron work function (Φ^+) can escape into vacuum.

Early experiments indicated that solid Ne is an intrinsically superior positron moderator than the heavier rare gases (Rg) [20]. However, more recent work has demonstrated *nearly* as good moderation efficiencies for properly prepared argon (Ar), krypton (Kr), and xenon (Xe) films [23-26]. Our conjecture is that the key factor in determining the positron moderation efficiency is the crystalline quality of the deposit, which depends strongly on sample preparation conditions and annealing history. Epithermal positrons can scatter from impurities and crystal defects, lowering their characteristic diffusion length, and hence their probability of reaching the solid surface and escaping into vacuum. Nearly thermalized positrons can localize and annihilate at gross defects, such as crystallite grain boundaries, further reducing their survival probability. In hindsight, the apparent superiority of Ne as a moderator is probably due to the relative ease of preparation of better quality (poly)crystalline Ne solids *via* the highly non-equilibrium vapor deposition process. This follows from the greater mobility of Ne atoms during sample condensation, which is due to their smaller mass and weaker interatomic forces; all these comparisons being relative to the heavier Rg. However, experiments on the structure of Ne solids grown under similar conditions indicate a crystallite grain size ~ 100 nm, with voids of up to 100 nm size also present [27]. Thus, even these supposedly “superior” Ne solids include gross defects at high enough concentrations to potentially impede the transport of the epithermal positrons along their $L_+ \sim 1$ μm long hot diffusion path to the moderator surface.

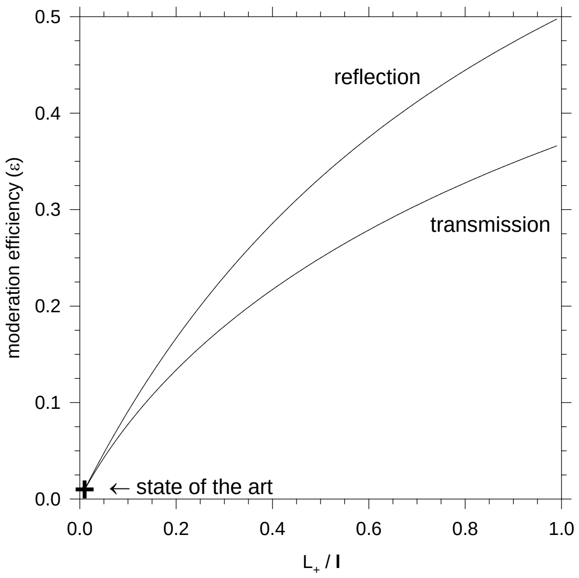

Figure 4. Theoretical positron moderation efficiencies *vs.* L_+/ℓ

We have performed a theoretical analysis of the potential for improvement in positron moderation efficiency (see Appendix A), extending a simple one-dimensional reflection geometry moderation model [1] which includes the characteristic implantation depth (**ℓ**) for fast positrons and the characteristic hot diffusion length (L_+) for epithermal positrons. In summary: Figure 4 shows that nearly two orders-of-magnitude higher positron moderation efficiencies are theoretically possible in a material for which the range of the epithermal positrons can be made comparable to the fast positron implantation depth. We thus focus our attention towards finding a new moderator material which is similar to the current champion, solid Ne, but which can be prepared as a lower-defect-concentration vapor deposited solid; minimizing the undesired trapping and annihilation of the positrons and correspondingly increasing their ability to reach the moderator surface and escape. Nature provides us with one particularly intriguing candidate: solid parahydrogen (pH_2) [28].

1.C. The Case for Solid pH_2 as a Candidate Positron Moderator

This project builds upon previous Air Force Research Laboratory (AFRL) in-house research on the production and spectroscopic characterization of low-defect-concentration vapor-deposited cryogenic pH_2 solids; work performed within the High Energy Density Matter (HEDM) program [29]. To the best of our knowledge, solid pH_2 has never been investigated as a positron moderator (although both Rg and hydrogenic solids have been used successfully to moderate energetic muons [30-32]). At the beginning of this project (c2003), we proposed that the unique properties of solid pH_2 may yield significant advantages in this role.

Table 1 compares some structural and dynamical properties of the Rg solids and solid pH_2, including: atomic number Z [33], molecular mass M [33], molar volume V_m [34], bulk density ρ_0 [35], number density n_0 [36], nearest neighbor separation r_{nn} [34,35], and the Debye temperature Θ_D [34,35]; unattributed quantities are calculated using a value of $N_A = 6.022 \times 10^{23}$ for Avogadro's constant.

Table 1. ***Comparison of structural and dynamical properties of Rg and pH$_2$ solids; a = [33], b = [34], c = [35]***

solid	**Z**	**M (amu)**	**V_m (cm^3/mol)**	**ρ_0 (g/cm^3)**	**n_0 (cm^{-3})**	**r_{nn} (Å)**	**Θ_D (K)**
pH$_2$	2[a]	2.02[a]	23.16[b]	0.087	2.60x10^{22}	3.79[b]	120[b]
Ne	10[a]	20.18[a]	13.8	1.51[c]	4.36x10^{22} [c]	3.16[c]	75[c]
Ar	18[a]	39.95[a]	22.6	1.77[c]	2.66x10^{22} [c]	3.76[c]	92[c]
Kr	36[a]	83.80[a]	27.8	3.09[c]	2.17x10^{22} [c]	4.00[c]	72[c]
Xe	54[a]	131.29[a]	36.7	3.78[c]	1.64x10^{22} [c]	4.34[c]	64[c]

Solid pH$_2$ is the lowest mass density and lowest atomic number crystalline solid material which can support a free vacuum surface (neither ^{3}He nor ^{4}He solidify at zero pressure even at T = 0 K [35]). At liquid helium (lHe) temperatures (*i.e.* 1 < T < 5 K), essentially all the H$_2$ molecules in a pH$_2$ solid exist in their ground electronic ($^1\Sigma_g^+$), vibrational (v=0), and rotational (J=0) states [34]. The free rotation and hence spherical nature of the pH$_2$ molecule is nearly perfectly preserved in the solid state [36]. Thus, solid pH$_2$ more closely resembles an atomic Rg solid rather than a molecular van der Waals solid such as solid nitrogen (N$_2$), solid oxygen (O$_2$), or solid carbon monoxide (CO).

The resulting absence of permanent molecular electrostatic multipoles contributes to very weak attractive pH$_2$-pH$_2$ intermolecular interactions. The weak intermolecular interactions and the small H$_2$ mass result in solid pH$_2$ existing as a "translational quantum solid" in which the pH$_2$ molecules experience large zero-point excursions in a very flat anharmonic potential about their lattice positions [34]. The small restoring forces holding the pH$_2$ molecules to their lattice positions translate into unusually low lattice vibration frequencies for such a low mass oscillator, embodied by the relatively low Debye temperature. Solid pH$_2$ is thus an extraordinarily compressible and "soft" [37] solid, relative to the Rg solids or other molecular van der Waals solids. For example: for a typical van der Waals solid applying a pressure of P ≈ 10 kbar results in a few percent change in density; for solid pH$_2$ applying P ≈ 10 kbar results in a <u>doubling</u> of the density [34].

During the sample vapor deposition process, the mobility of pH$_2$ molecules far exceeds even that of Ne atoms, facilitating the production of well-ordered crystallites. Solid pH$_2$ is also supposed to possess "self-healing" [38] properties by which damage to the crystal incurred during local high-energy deposition events (*e.g.*: photodissociation of dopant molecules) is automatically repaired. Indeed, pH$_2$ solids have been shown to retain their quality even under ~ MRad exposures to gamma radiation [39]. All these factors support the fundamental premise underlying our approach: <u>the preparation and maintenance of low-defect-concentration crystals should be substantially easier for solid pH$_2$ than for any of the solid Rg, including solid Ne</u>.

In fact, shadowgraph images of vapor deposited pH$_2$ solids reveal crystallite diameters ~ 100 μm [40], which is three orders-of-magnitude larger than the ~ 100 nm crystallites observed in vapor deposited Ne solids [27]. <u>Thus, if scattering of epithermal positrons at crystallite grain boundaries is in fact the dominant scattering mechanism, we anticipate up to a ~ 1000x increase in the range of epithermal positrons (L_+) in solid pH$_2$ compared to solid Ne!</u>

Table 2. ***Comparison of electronic properties of Rg and pH_2 solids***
a = [44], b = [45], c = [46], d = [47], e = [48], f = [49], g = [50], h = [51]

solid	E_g (eV)	E_x (eV)	W_{max} [37 keV] (eV)	κ @ T(K)	S [200 keV] (MeV cm^2/g)	l_{CSDA} [200 keV] (μm)
pH_2	14.5^a	10.9^c	14.0^e	1.297 @ $2K^f$	5.9^h	2460^h
Ne	21.7^b	17.4^d	17.8^e	1.51 @ 4 K^g	2.3^h	360^h
Ar	14.2^b	12.1^d	12.5^e	1.63 @ $20K^g$	2.0^h	360^h
Kr	11.6^b	10.2^d		1.88 @ 20 K^g	1.8^h	240^h
Xe	9.3^b	8.4^d		2.19 @ 20 K^g	1.6^h	210^h

The only other fundamental difference between epithermal positron transport in solid Ne *vs*. solid pH_2 is the possible excitation of low lying rotational (≈ 0.04 eV) and vibrational (≈ 0.5 eV) energy levels in solid pH_2 [34]. Such effects were found to be minor for epithermal positrons in solid N_2 [41]; however, the inelastic cross section for vibrational excitation of H_2 by positrons is ~ 30 times larger than for N_2, and each collision typically transfers ~ 10 times the energy [42,43]. Thus, we were unsure at the start of this project whether these low lying rotational and vibrational states in solid pH_2 would have either detrimental (*e.g.* providing additional localization and annihilation channels) or beneficial (*e.g.* narrower energy distribution for moderated positrons) consequences. As discussed further below in the Results section, the surprisingly poor positron moderation performance of pH_2 solids points to the former.

Table 2 compares some electronic properties of Rg and pH_2 solids, including: the valence-conduction band gap E_g [44,45], the energy of the lowest lying (n = 1) exciton state E_x [46,47], the energy of the first maximum in the electron energy loss spectrum for fast (KE = 37 keV) electrons W_{max} [48], the zero-frequency dielectric constant κ [49,50], the stopping power for fast (KE = 200 keV) electrons S [51], and the implantation depth for a 200 keV electron calculated in the continuous slowing down approximation l_{CSDA} [51-53]. Like the Rg solids, solid pH_2 is a wide band-gap insulator; its ultraviolet absorption spectrum shows excitonic and valence-conduction band gap features very similar to those for the Rg solids [44-47]. Electron energy loss measurements on moderately fast (KE = 37 keV) electrons also show strong similarities [48]. The values of l_{CSDA} listed in Table 2 are calculated using an on-line version of the ESTAR program [51].

All these factors indicate that the basic mechanism for moderation of fast charged particles in Rg solids, depicted above in Figure 3 and assumed throughout the analysis summarized in Figure 4, should hold for solid pH_2 as well. The low solid pH_2 electron density ($n_e = Z\ n_0 = 5.2\text{x}10^{22}\ cm^{-3}$) results in an increased implantation depth for fast electrons (and positrons), which is expected to increase by a factor of ≈ 7x over that in solid Ne [51]. However, we gladly sacrifice this 7x increase in ℓ in return for the prospect of a 1000x increase in L_+. Thus, the quotient $L_+/\ \ell$ is conservatively expected to increase from $L_+/\ \ell \sim 0.01$ for solid neon to at least $L_+/\ \ell \sim 0.1$ for solid pH_2, leading to an order-of-magnitude improvement in positron moderation efficiency, again provided that epithermal positron scattering and annihilation at crystallite grain boundaries is indeed the major loss mechanism. We describe below side-by-side comparisons of pure solid pH_2 and pure solid Ne positron moderators to test this hypothesis.

1.D. Project Goals and Objectives

The primary goal of this project is to develop improved efficiency (ε) cryogenic solid positron moderators capable of a 10x performance improvement over the state-of-the-art solid Ne moderator ($\varepsilon_{Ne} \sim 1$ %). Secondary goals include determining the relative positron moderation efficiencies of different moderator microstructures, and determining the mechanism(s) responsible for the observed decrease in performance of working moderators.

The corresponding primary objective is thus to design, construct, validate, and exploit a working positron moderation apparatus capable of providing a direct comparison between solid Ne and other candidate cryogenic solid positron moderators. Achieving the secondary goals requires the integration of diagnostics capable of characterizing moderator microstructure, to include the buildup of radiation damage and the presence of surface and bulk impurities.

1.E. Technical Challenges and Approaches

A fundamental technical challenge is the manipulation of fast and slow positrons. We employ a standard approach to obtaining fast positrons from an ultrahigh vacuum (UHV) compatible sealed radioactive ^{22}Na source which emits positrons through a thin (5 μm) titanium (Ti) window [1-3]. After a long regulatory permitting process [54], we acquired two such sealed sources, with nominal initial activities of 1.0 mCi and 0.1 mCi measured at their January 2007 production date. Typical practice to maximize the yield of slow positrons is to incorporate the ^{22}Na source into a recess in the cryogenic moderator deposition apparatus [20,21]. The Rg moderator is grown by vapor deposition directly onto the Ti window, as well as onto the interior surfaces of the hollow recess, resulting in positron moderation *via* combined transmission and reflection processes. We instead adopt a pure reflection moderation geometry, with the room temperature ^{22}Na source capable of independent motion relative to the cryogenic moderator deposition substrate, which greatly simplifies the interpretation of our experimental results.

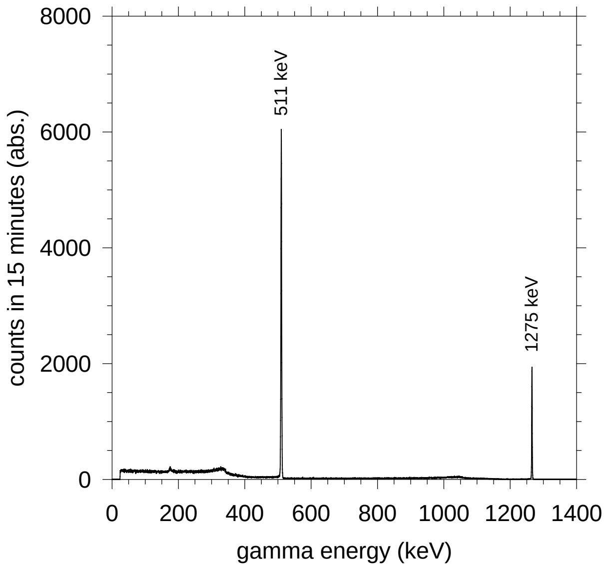

Figure 5. HPGe gamma spectrum of 1 μCi ^{22}Na check source [MF10141D]

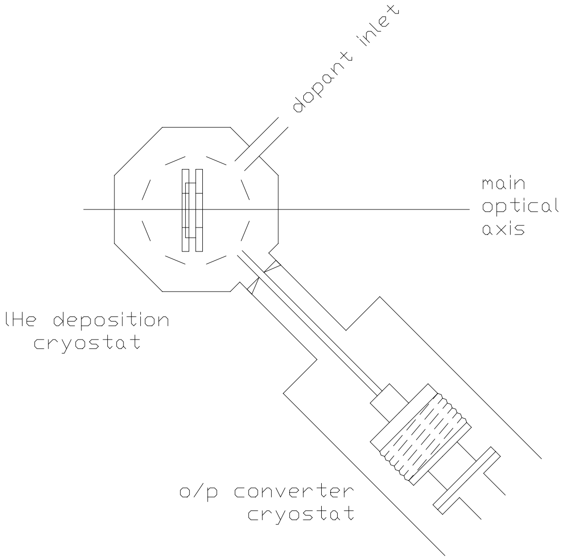

Figure 6. Solid pH_2 Rapid Vapor Deposition experimental schematic [55,56]

Another technical challenge is the unambiguous detection of successfully moderated slow positrons. Figure 5 shows the high-resolution gamma ray spectrum of a 1 μCi ^{22}Na check source measured using a high-purity germanium (HPGe) detector. The peak at 511 keV is due to positron annihilation and the peak at 1275 keV to the decay of the excited ^{22}Ne nucleus formed in the positron emission process [1]. This spectrum points out the difficulty in detecting slow positrons in the vicinity of the ^{22}Na source. Our approach is to separate the slow positrons using weak electromagnetic fields that have minimal effect on fast positrons, and to transport the slow positrons to a “quieter” radiation environment for detection.

We address the technical challenges of producing and characterizing our positron moderators by adapting the cryogenic solid vapor deposition scheme with open optical access pictured in Figure 6. In our prior HEDM research effort, we learned to produce very high quality (poly)crystalline pH_2 solids by Rapid Vapor Deposition (RVD) [55] of pre-cooled pH_2 gas produced in an ortho/para (o/p) converter [56] onto a $\approx$ 2 K substrate in vacuum. The excellent optical transparency of our pH_2 solids enables their detailed spectroscopic characterization *via* analysis of the condensed-phase-induced infrared (IR) absorption and Raman scattering spectra. We speculate that the good (poly)crystallinity of our samples is due to local heating and annealing of the accreting surface layers during the extraordinarily fast rapid vapor deposition process [57].

Figure 7 shows a notional experimental schematic which summarizes the various elements of our approach: an independently moveable ^{22}Na source of fast positrons, RVD production and IR spectroscopic characterization of cryogenic solid moderators, electrostatic collection and magnetically guided transport of slow moderated positrons, detection of slow positrons in a separate annihilation chamber. Figure 8 shows the evolution of this notional design showing explicitly the long, bent slow positron transport tube scaled to fit onto a 4x4-foot optical table. The sharp 90° bend in this tube is intended to cause fast unmoderated positrons to impact the tube wall, thus preventing them from reaching the annihilation chamber.

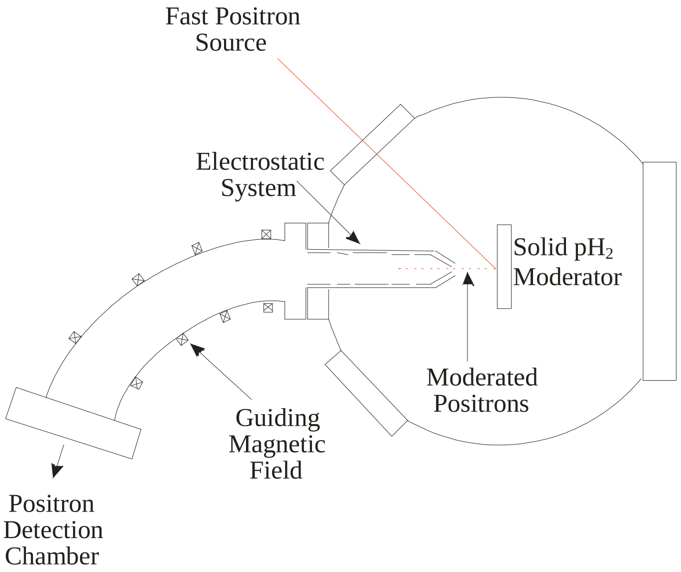

Figure 7. Notional experimental schematic diagram

Other remaining technical challenges (*i.e.* known unknowns) arise from our initial assumptions, and can be stated as questions to be answered over the course of this project. Is the range of hyperthermal positrons really limited by crystal defects, or is it instead limited by positron-phonon scattering [22]? Will the low lying rotational and vibrational states in solid pH_2 prove beneficial or detrimental to efficient positron moderation? Will the chosen spectroscopic diagnostics be capable of distinguishing between the incorporation of bulk impurities, the buildup of surface impurities, and the accumulation of radiation damage? Will our non-standard positron moderation experimental configuration, with its open optical access to the moderator, introduce unanticipated artifacts that will interfere with our measurements?

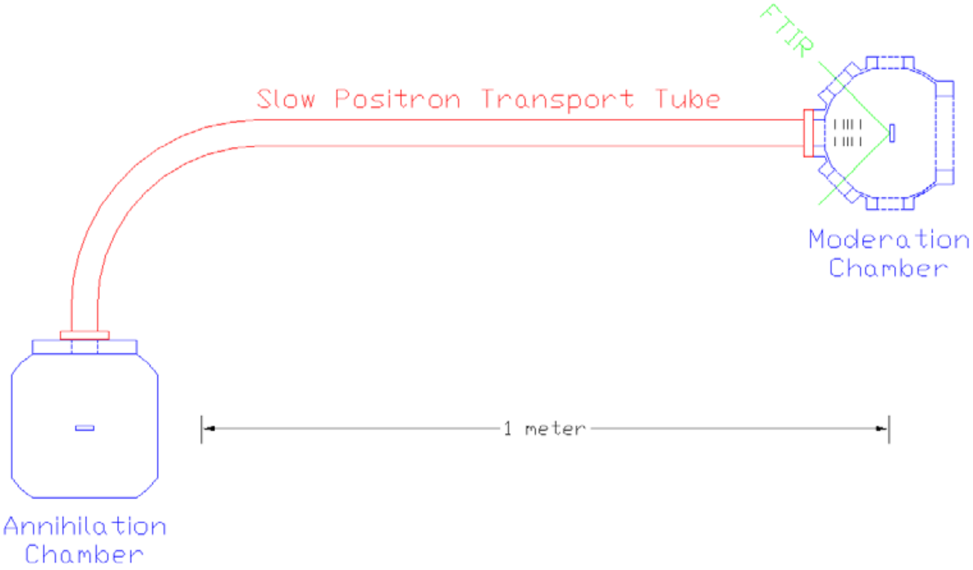

Figure 8. Evolving notional experimental schematic

2. EXPERIMENTAL

2.A. ^{22}Na Positron Sources

Figure 9 shows sketches of the ^{22}Na source manipulator assembly in “Storage” *(i.e.* source retracted) and “Active” modes. The source is attached to an electric-motor-driven translation stage which is controlled manually with a handheld control switch.

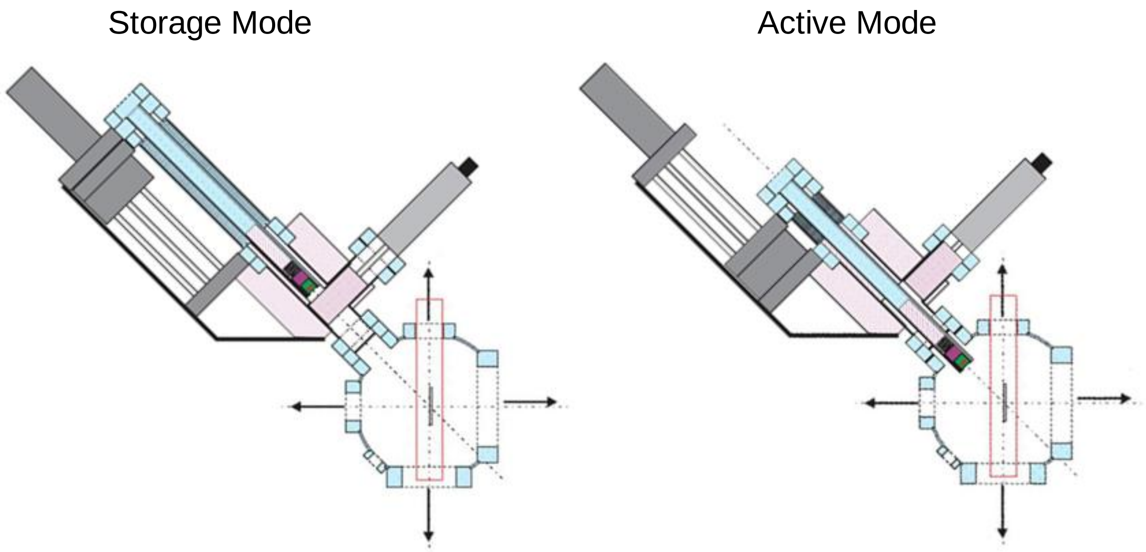

Figure 9. ^{22}Na source manipulator schematic

Figure 10 shows a photo of the Elkonite tungsten/copper alloy shielding which completely surrounds the ^{22}Na source in Storage mode. Although unnecessary from an

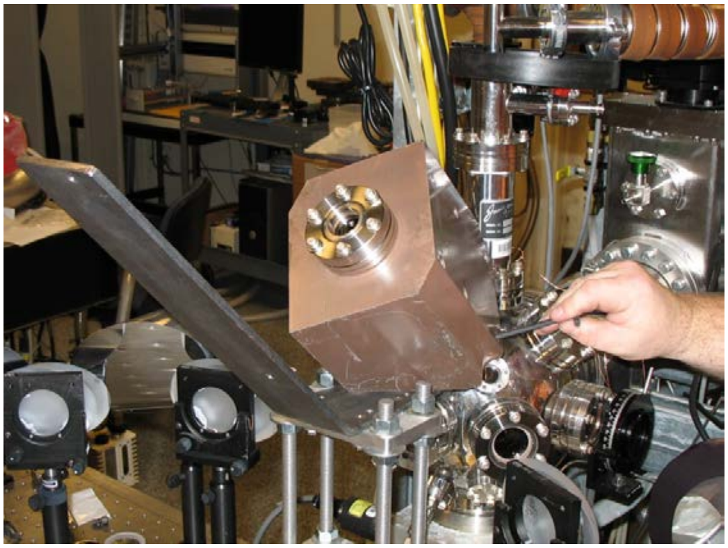

Figure 10. Photo of Elkonite shielding surrounding ^{22}Na source manipulator

occupational safety standpoint, we included this extra gamma radiation shielding under the ALARA (as low as reasonably achievable) operating philosophy [58]. The half-life of ^{22}Na is $t_{½}$ = 2.60 years [1], and the fractional remaining activity of a radioactive source is given by:

$$A(t) / A_0 = \exp[-t/(1.44\ t_{½})] \qquad (1)$$

We performed all our positron moderation experiments with the ^{22}Na source having a nominal original activity A_0 = 1.0 mCi (January 2007). We installed the source into our apparatus in September 2010, by which time its activity had decayed to ≈ 370 μCi. Note that this is less than the 400 μCi annual limit of intake (ALI) for oral ingestion of ^{22}Na [59]. Most of our positron moderation experiments were performed in September and October 2010; with the remainder taking place in September 2011, when the ^{22}Na source activity had decayed to ≈ 280 μCi.

2.B. Production of Cryogenic Solid Moderators

As shown above in Figures 7-9, the cryogenic solid moderator deposition substrate is located at the center of the UHV Moderation chamber. The deposition substrate is cooled by a lHe transfer cryostat, the top of which is visible in the photo in Figure 10, just behind and to the right of the Elkonite shielding block. The top right corner of Figure 10 shows our provision for pumping on the gaseous He exhaust, which allows us to cool the cryostat cold-tip to T ≈ 2 K.

Figure 6 above shows our scheme for RVD of pH_2 solids onto a transparent substrate; developed at Edwards AFB during the HEDM program. The room-temperature normal-H_2 (nH_2) gas passes through an o/p-converter cooled by an independent closed-cycle He refrigerator [56]. The o/p-converter contains a catalyst which speeds the kinetics of the ortho-para conversion process so that the H_2 gas comes to equilibrium at the temperature of the converter. Figure 11 shows the residual oH_2 fraction in equilibrated-H_2 (eH_2) as a function of temperature, calculated for an ensemble of non-interacting rigid rotors [28] with rotational constant $B(H_2)$ = 59.3 cm^{-1}.

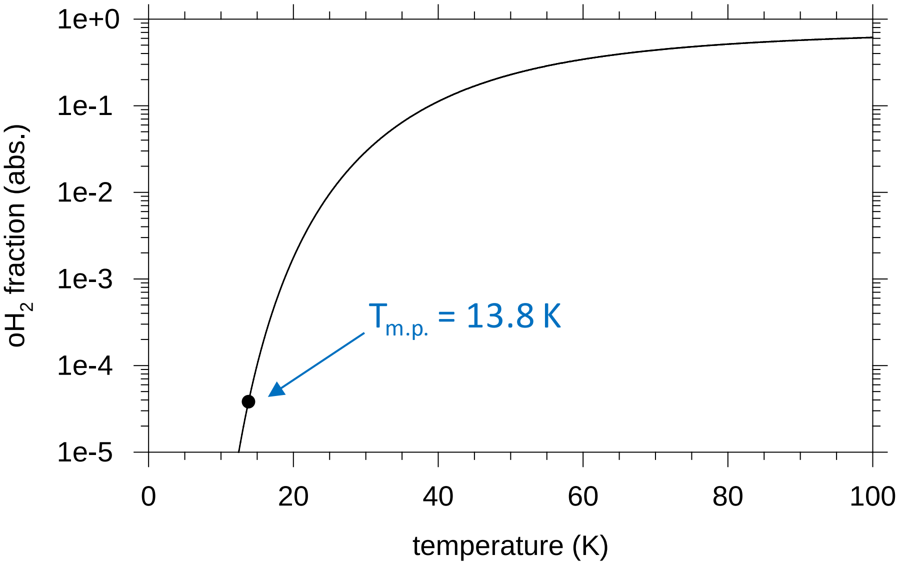

Figure 11. Residual oH_2 fraction *vs.* T [28]

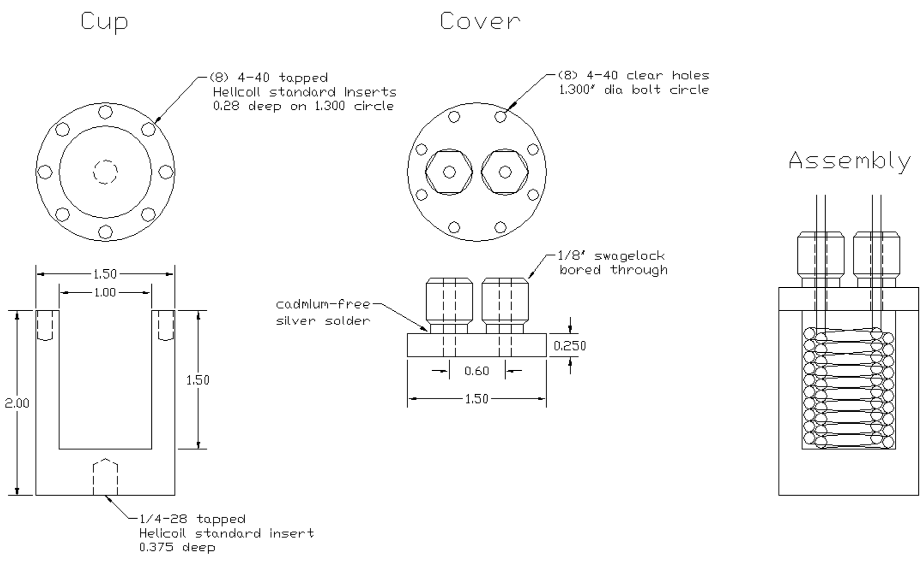

Figure 12. UHV compatible o/p-converter drawings

Figure 12 shows drawings of the UHV compatible o/p converter we designed and constructed specially for our positron moderation experiments. Using glass wool plugs, we constrain ≈ 1 g of APACHI catalyst [34] to the central 0.6 m portion of a 0.8-m-long section of 1/8-inch diameter Cu refrigeration tubing. We wind this catalyst-packed tubing into a double coil and extend the open ends through the compression fittings in the converter's cover. We pot the coils into the cup with silver-filled epoxy, and seal the cover onto the cup with an indium foil gasket. This arrangement seals the epoxy within the converter, exposing only metal surfaces to the vacuum chamber. Figure 13 shows a photo of the assembled o/p converter, attached to the closed-cycle cryostat cold-tip, and with nH_2 inlet and original Cu pH_2 delivery tubing in place.

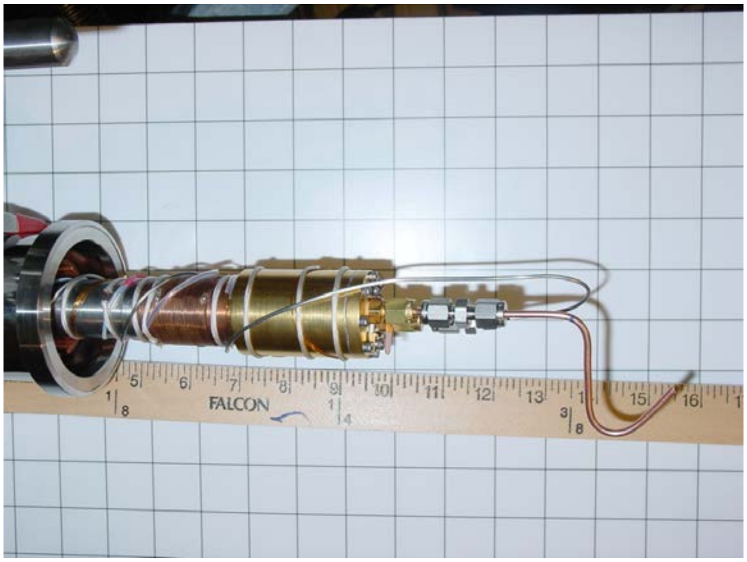

Figure 13. Photo of UHV compatible o/p-converter mounted on closed-cycle cryostat insert

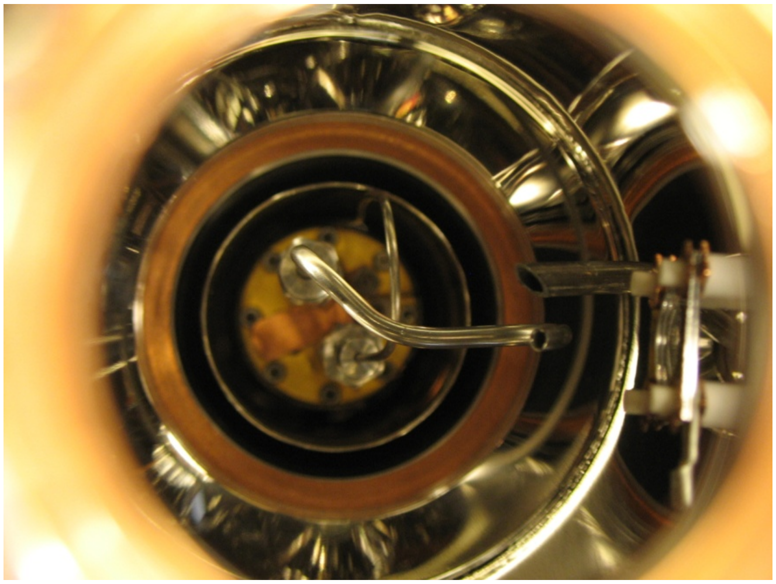

Figure 14. Photo of Moderation chamber interior showing gas delivery tubes

Figure 14 shows a top view of the interior of the Moderation chamber, with the o/p converter in place and sporting the final stainless steel (SS) pH_2 delivery tube. The slightly larger diameter SS tube visible just above the pH_2 delivery tube is connected through a fine metering valve to an independent dopant gas handling manifold.

Disposing of H_2 gas used in our experiments raises certain safety concerns [60]. Since mixtures of H_2 + air + N_2 containing less than 5 % O_2 are not flammable regardless of the H_2 content [61], as shown in Figure 15 we purge the mechanical vacuum pump inlets and exhaust lines with gaseous N_2 having a maximum permissible O_2 concentration of 3 %.

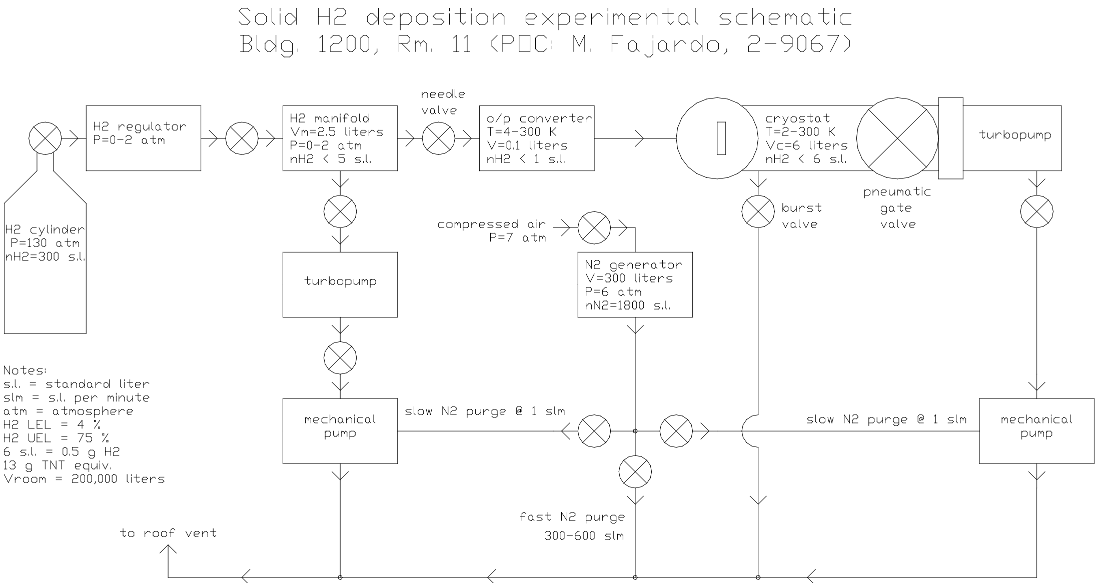

Figure 15. Schematic of N_2 purge gas system

2.C. High Resolution IR Spectroscopic Characterization

We have already reported most of the novel results on IR spectroscopic characterization of pH_2 solids obtained during this project in two peer-reviewed journal articles [62,63] and in a book chapter [64]. Here, we briefly summarize those results most relevant to the experimental determination of sample thicknesses, dopant concentrations, and sample microstructure.

2.C.1. Solid pH_2 thickness determinations

Figure 16 shows the condensed-phase-induced IR absorption spectrum of a nominally pure 2.8-mm-thick pH_2 solid deposited on a transparent BaF_2 substrate at T = 2.4 K [64], obtained in transmission geometry using the apparatus depicted above in Figure 6. We have previously reported on the use of these absorptions to determine the thicknesses of our solid pH_2 samples [64,65]. Table 3 summarizes various functions of the $Q_1(0) + S_0(0)$ and $S_1(0) + S_0(0)$ absorption band integrated intensities, abbreviated as: $\int A_{Q+S} d\bar{\nu}$ and $\int A_{S+S} d\bar{\nu}$, respectively.

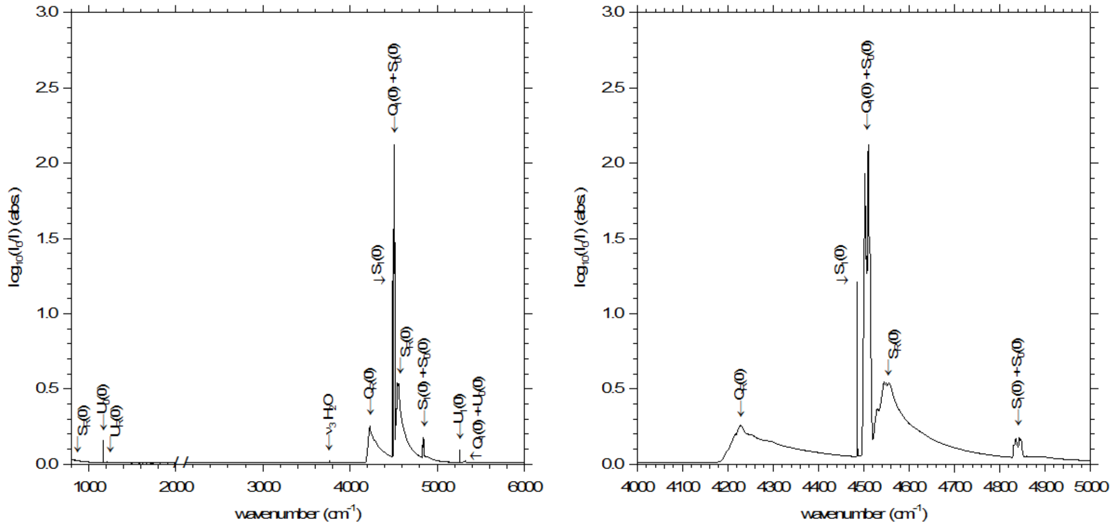

Figure 16. Condensed-phase-induced IR absorptions in pure solid pH_2 [64]

Table 3. ***Solid pH_2 optical path length determination***
"Q+S" = $Q_1(0) + S_0(0)$; 4495 to 4520 cm^{-1}. "S+S" = $S_1(0) + S_0(0)$; 4825 to 4855 cm^{-1}.
$\Delta A_{10}[Q_R(0)] \equiv A_{10}(4228.5\ \text{cm}^{-1}) - A_{10}(4100\ \text{cm}^{-1})$.
The stated uncertainties indicate the 95% confidence limits

Quantity	Old value from Ref. [65]	Recommended value [64]
$\int A_{Q+S}\, d\bar{\nu}\ /\ \int A_{S+S}\, d\bar{\nu}$	13.0 ± 0.4	12.9 ± 0.2
$\int A_{Q+S}\, d\bar{\nu}\ /\ d$	82 ± 3 cm^{-2}	90 ± 2 cm^{-2}
$\int A_{S+S}\, d\bar{\nu}\ /\ d$	6.3 ± 0.3 cm^{-2}	7.0 ± 0.2 cm^{-2}
$\Delta A_{10}[Q_R(0)]\ /\ d$	---	0.90 ± 0.03 cm^{-1}

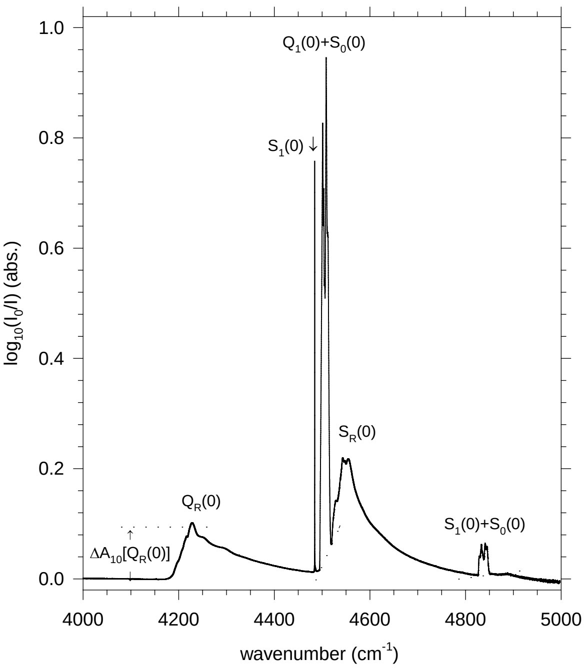

Figure 17. Integration baselines for determining pH_2 sample thickness [ML01129.9]

Figure 17 shows an absorption spectrum obtained by combined reflection/transmission at 45° incidence through a pure pH_2 solid deposited on the Au coated Cu (Au/Cu) substrate in our Moderation chamber. The lineshapes are very similar, but not identical, to those shown in Figure 16. We *have* confirmed that the *integrated intensities* of the Q+S and S+S features are relatively insensitive to deposition-condition-dependent microstructure and IR diagnostic polarization effects. Thus, we can safely adopt the results from our old single-pass transmission geometry experiments to our new reflection/transmission setup. Figure 17 also illustrates that our chosen integration baselines for the Q+S and S+S features are *not* simply $A_{10} = 0$; rather, they are sloping line segments drawn between the values of $A_{10}(\bar{\nu})$ at the integration endpoints listed in Table 3.

2.C.2. Detection of intentional dopants and unintentional impurities

The spectrum in Figure 16 also shows a very weak absorption at 3765.5 cm^{-1}, indicating the presence of isolated H_2O molecules as an unintentional impurity at the 200 ppb concentration level [64]. Clearly, direct absorption spectroscopy in the open 800-4200 cm^{-1} spectral region is an effective way to detect the presence of IR active impurities. We can move from simple detection to quantification of impurity concentrations by suitable application of the Beer-Lambert Law [65]. However, we have not completed this analysis for most of our IR absorption data from positron moderators, and so report nominal dopant concentrations calculated from the amounts of dopant and host gases introduced during the codeposition process.

Figure 18 shows the IR activity induced in the pH_2 host by the presence of various electrically neutral and charged species. Trace (a) is for the pure 2.8-mm-thick pH_2 sample depicted above in Figure 16; (b) is for a 3.6-mm-thick 2500 ppm oH_2 sample; (c) is for a 2.6-mm-thick 1000 ppm Ar sample, (d) is for a 2.8-mm-thick 1000 ppm N_2 sample; (e) is for a

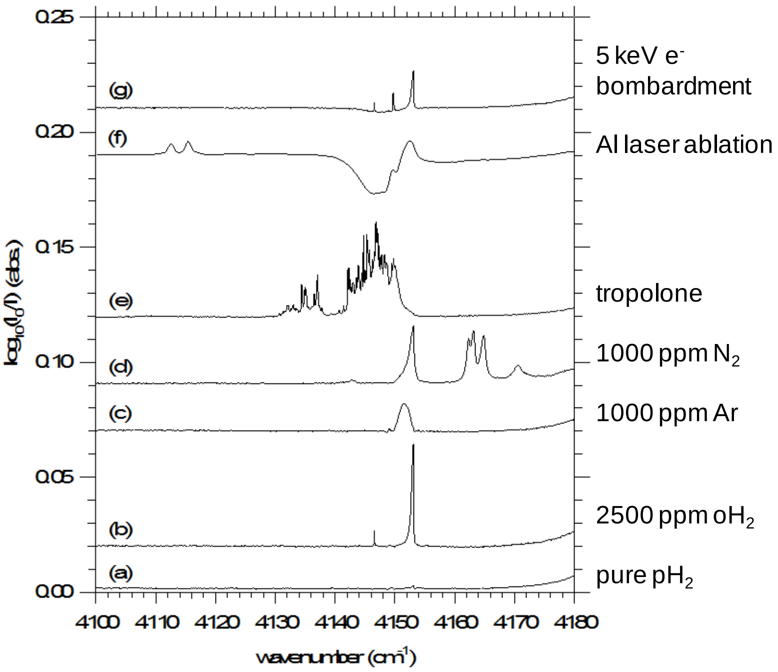

Figure 18. Dopant-induced IR absorptions in doped solid pH_2 [64]

1.6-mm-thick tropolone-doped sample; (f) is for a 1.4-mm-thick sample doped by laser ablation of solid aluminum; (g) is for an electron-bombarded 0.7-mm-thick pH_2 sample. The spectra are presented at 0.1 cm^{-1} resolution, except for trace (f) which is shown at 1.0 cm^{-1} resolution. Traces (a)-(f) are single-pass absorptions, trace (g) is a 45°-incidence double-pass absorption of a sample deposited onto the Au/Cu metal substrate under bombardment by 5 keV electrons. All samples included in Figure 18 are shown as-deposited at T = 2.4 K, except for trace (d) which is undergoing annealing at T = 4.8 K. These spectra demonstrate our ability to detect the presence of relatively large (> 100 ppm) concentrations of even IR-inactive impurities, and perhaps also the accumulated products of radiation damage, in our solid pH_2 moderators.

2.C.3. Solid pH_2 microstructure from polarized IR spectra

We have reported extensively on the fact that our as-deposited pure RVD pH_2 solids have a mixed hexagonal-close-packed/face-centered-cubic (hcp/fcc) structure, which anneals to nearly pure hcp upon warming to $T \approx 4.5$ K; with the hcp crystal c-axis roughly aligned with the substrate surface normal [64]. However, we still do not have any information about the sizes of the hcp and fcc regions produced by the RVD method; they might be visible with polarized optical microscopy [40], or intermingled at the molecular level, or anything in between.

As depicted in Figure 19, the single-substitutional trapping sites in hcp and fcc solid pH_2 are of D_{3h} and O_h symmetry, respectively [66,67]. The most obvious differences between these trapping environments is the reduced symmetry of the D_{3h} site, and the existence of a unique direction associated with the hcp c-axis. This results in dopants in hcp sites experiencing a much more anisotropic crystal field perturbation, and in a clear polarization dependence for certain dopant rovibrational transitions relative to the hcp c-axis [62-64,66,67].

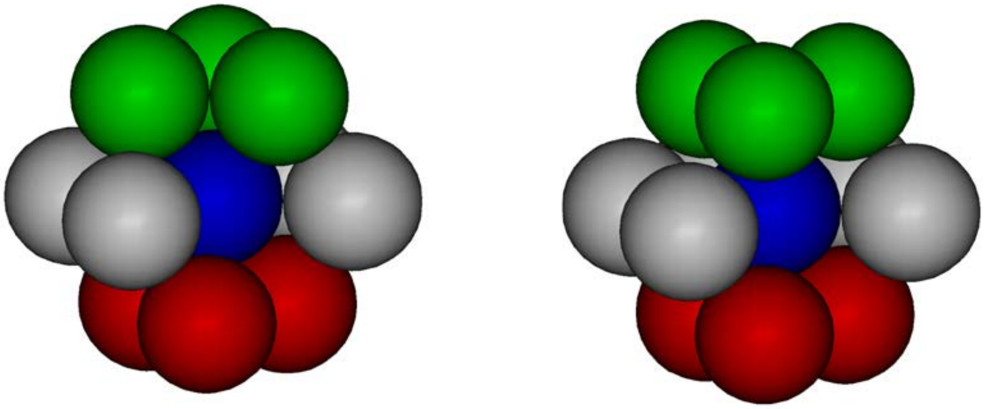

"face-centered cubic"
fcc ⇒ O_h site symmetry,
nearly isotropic

"hexagonal close-packed"
hcp ⇒ D_{3h} site symmetry,
unique c-axis

Figure 19. Cartoon of fcc and hcp single-substitutional trapping sites

Figure 20 shows a sketch of our Polarized IR Absorption Spectroscopy (PIRAS) setup [62,63] integrated with our cryogenic solid moderator deposition scheme, and a graphical depiction of the "p-polarized" (in the plane of reflection) and "s-polarized" components of the IR beam [68]. We designed the system so that we rotate the two polarizers together to eliminate the effects of any depolarization during the reflection/absorption process. However, we have never observed this effect, and a single polarizer placed after the sample would probably suffice.

Appendix B presents a naïve analysis of the anticipated spectroscopic consequences in the special case of perfect alignment of the hcp crystal c-axis with the substrate surface normal.

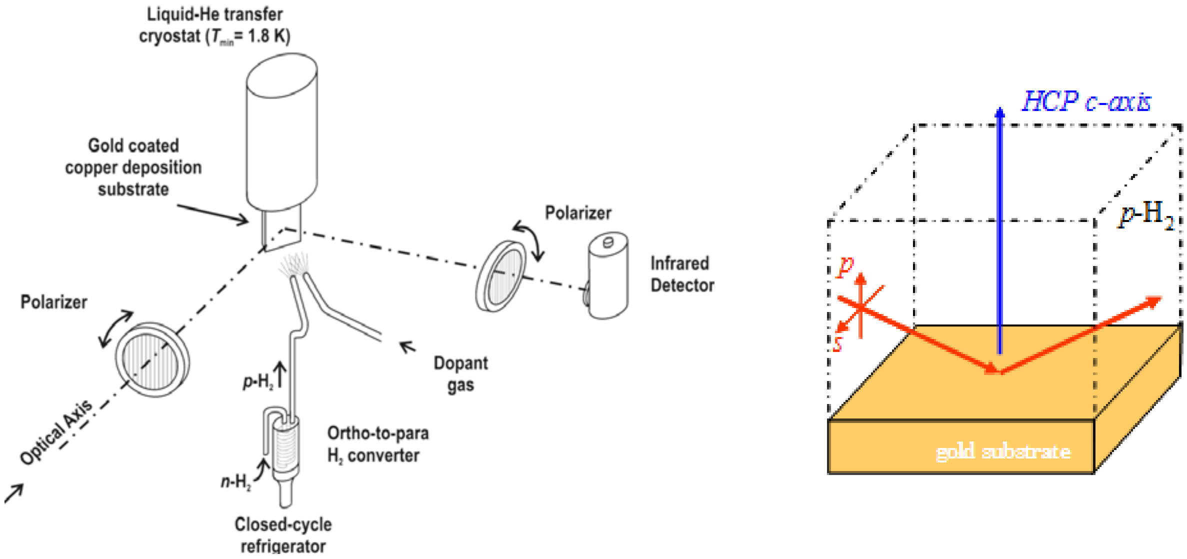

Figure 20. Deposition and PIRAS schematics

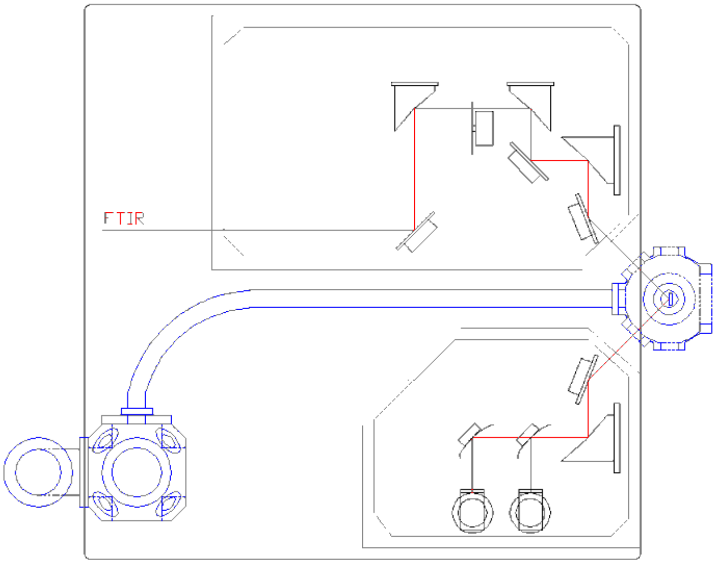

Figure 21. 4x4-foot optical table layout

Figure 21 shows the integration of the IR spectroscopy optics with the positron Moderation and Annihilation vacuum chambers on the 4x4-foot optical table. The IR beam from our Bruker IFS120HR high-resolution Fourier Transform IR (FTIR) spectrometer enters from the left, is brought to a secondary focus supplied with aperture and filter wheels, is recollimated and then focused onto the deposition substrate by a combination of an off-axis paraboloid and a plane mirror, is recollimated again and sent to a detector farm where moveable elliptical mirrors focus it onto one of several (HgCdTe, InSb, GaAs, or Si) IR detectors. We operate the FTIR spectrometer under vacuum ($P \sim 10^{-5}$ torr) and the remainder of the optical path is purged to minimize interference from atmospheric water vapor and CO_2. The IR polarizers depicted in Figure 20 are located in the convergent/divergent parts of the IR beam just inside the purge boxes and adjacent to the Moderation vacuum chamber.

2.C.4. Thin film reflection/transmission at 45° incidence

For the simple normal-incidence single-pass transmission geometry depicted above in Figure 6, the optical path length through the cryogenic solid is virtually the same as the physical thickness. The multi-pass contribution to the transmitted beam intensity due to the weak Fresnel reflections [68] at the moderator-substrate and moderator-vacuum interfaces is ~ (5%) x (5%) ≈ 0.003, which we neglect.

Figure 22 shows the relationship between optical path length, ℓ_{opt}, and moderator thickness, d_{mod}, for the $\theta_0 = 45°$ incidence combined reflection/transmission geometry through a cryogenic solid moderator deposited on the Au/Cu substrate in our Moderation chamber. Refraction at the moderator-vacuum interface causes the IR beam to bend towards the surface normal to an internal angle, θ_i, given by Snell's Law [68]:

$$\theta_i = \sin^{-1}[(n_0/n_i)\sin(\theta_0)] \qquad (2)$$

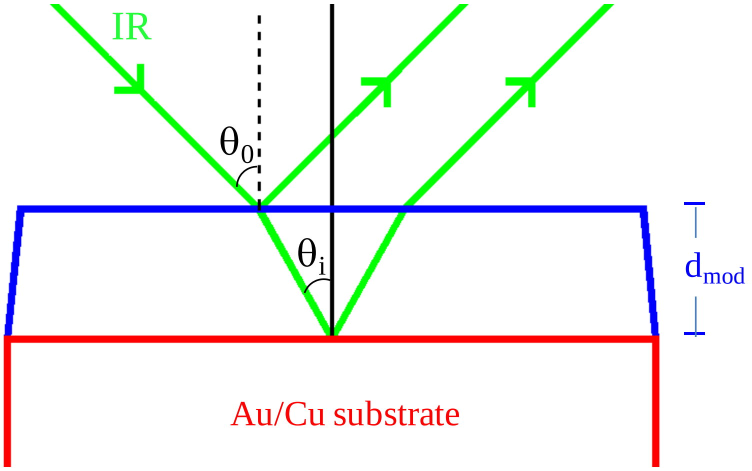

Figure 22. Reflection/transmission cartoon

where: $n_0 \equiv 1.000$ is the index of refraction of vacuum, and n_i is the index of refraction of the moderator. The moderator thickness and optical path length are related by:

$$d_{mod} = \tfrac{1}{2} \cos(\theta_i)\, \ell_{opt} \tag{3}$$

The portion of the IR beam reflecting from the moderator-vacuum surface interferes with the reflection from the moderator-substrate interface causing an oscillatory modulation in the IR spectrum [68]. Counting the number of fringes, $m_{fringes}$, separating two wave numbers (in cm^{-1}), $\bar{v}_1$ and $\bar{v}_2$, we can calculate the interferometric thickness of the moderator:

$$\begin{aligned} d_{Int}(\mu m) &= 10000(\mu m/cm)\, m_{fringes} / [2\, n_i \cos(\theta_i)\, (\bar{v}_1 - \bar{v}_2)] \\ &= C_{Int}\, m_{fringes} / (\bar{v}_1 - \bar{v}_2). \end{aligned} \tag{4}$$

Table 4 shows various useful path length parameters calculated for different cryogenic solids for $\theta_0 = 45°$ incidence.

Table 4. ***Reflection/transmission optical path length parameters for cryogenic solids a = [69], b = [70], c = [71], d =same as N_2 data***

solid	n_i	θ_i	$\cos(\theta_i)$	$2/\cos(\theta_i)$	C_{Int}
H_2	1.14[a]	38.34°	0.7844	2.550	5592
D_2	1.16[a]	37.56°	0.7927	2.523	5437
N_2	1.22[b]	35.42°	0.8149	2.454	5029
Ne	1.23[b]	35.09°	0.8182	2.444	4968
Ar	1.29[b]	33.24°	0.8364	2.391	4634
Kr	1.37[b]	31.08°	0.8565	2.335	4261
Xe	1.49[b]	28.33°	0.8802	2.272	3812
CO	1.22[d]	35.42°	0.8149	2.454	---
H_2O	1.26[c]	34.14°	0.8277	2.416	---

2.D. Electrostatic/Magnetostatic Manipulation of Moderated Positrons

2.D.1. Magnetically-guided slow positron transport through bent tube

We employ two different software tools to simulate the trajectories of slow positrons around a 90° bend in our magnetically-guided transport tube. The first is a home-made code written in BASIC that calculates the magnetic field of a series of multisided polygonal current loops *via* the Law of Biot and Savart [72] then integrates the equations of motion for electrons subjected to the velocity-dependent Lorentz force equation. Appendix C presents an *ad-hoc* numerical integration scheme with improved energy conservation we developed during this effort.

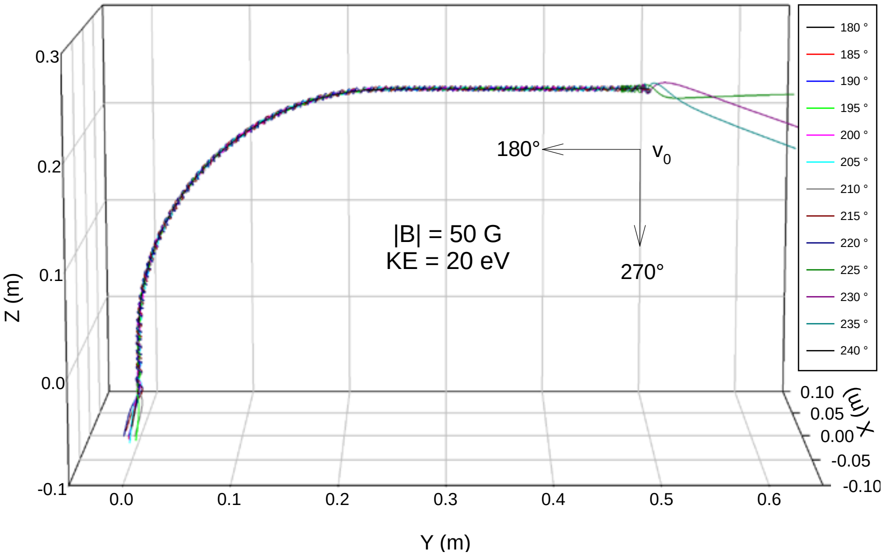

Figure 23. Acceptance angle for 20 eV electrons entering 50 G solenoid

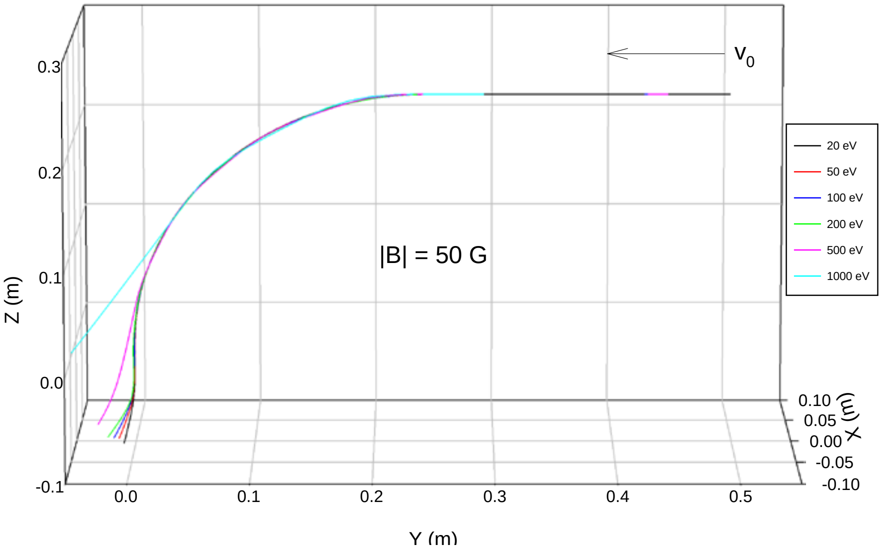

Figure 24. Transport of slow and fast electrons by 50 G solenoid

Figure 23 shows trajectories calculated for KE = 20 eV electrons entering a bent 40-mm-diameter solenoid with a |B| = 50 G centerline magnetic field. Electrons entering at angles up to 225° are successfully transmitted to the far end of the bent solenoid; the three steeper entry angles result in electrons being reflected back out the solenoid entrance.

Figure 24 shows the successful transport of slow electrons (KE ≤ 200 eV) which enter along the solenoid centerline, and the failure of the |B| = 50 G magnetic field to guide faster electrons around the 90° bend. We exploit this phenomenon to distinguish between successfully moderated slow positrons and unmoderated fast positrons.

2.D.2. Ion-optics for slow positron collection/injection

We also performed numerous simulations using the SIMION v8.0 software package [73]. Figure 25 shows a schematic of the first generation complete positron moderation apparatus, including an electrostatic potential surface and a solenoidal magnetic field calculated by SIMION, and our provision for electrically biasing the moderator deposition substrate.

Figure 26 shows a close-up view of the ion optics package in relation to the moderator deposition substrate. We provide an initial repulsive potential for the moderated positrons by biasing the deposition substrate to a typical voltage $V_1 = +40$ V. We bias the first element in the ion optics package to an attractive negative potential to collect and accelerate the positrons. The next three elements constitute a Retarding Potential Analyzer (RPA) with the outermost elements held at a constant potential while the voltage of the central element, V_4, is scanned to block or pass the positrons. The last element serves to focus the positrons into the entrance of the solenoid. Figures 27 and 28 show slow positron trajectories through the ion optics package for a range of starting positions in the moderator, and with the RPA in “On” and “Off” states.

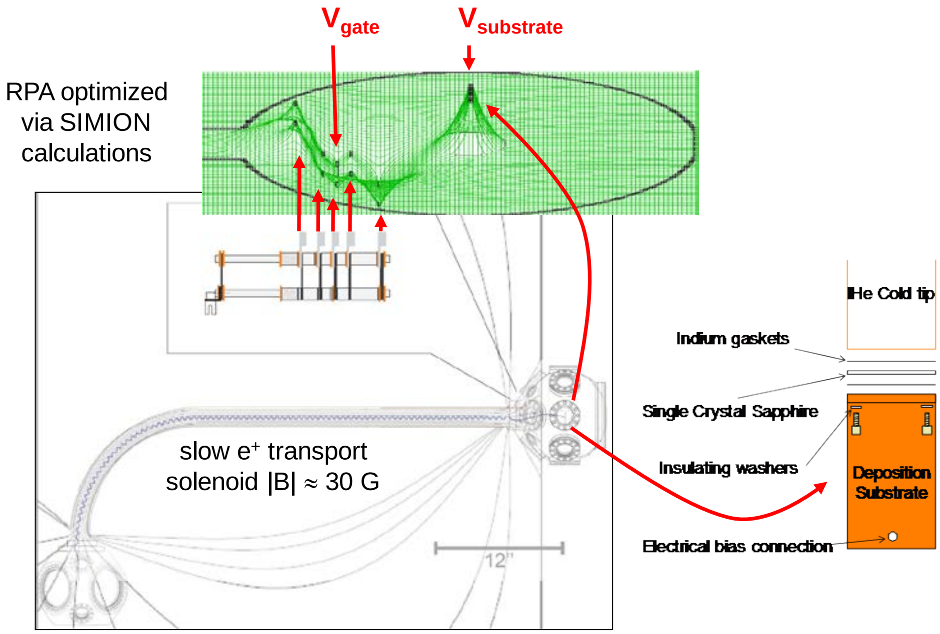

Figure 25. First generation complete experimental schematic

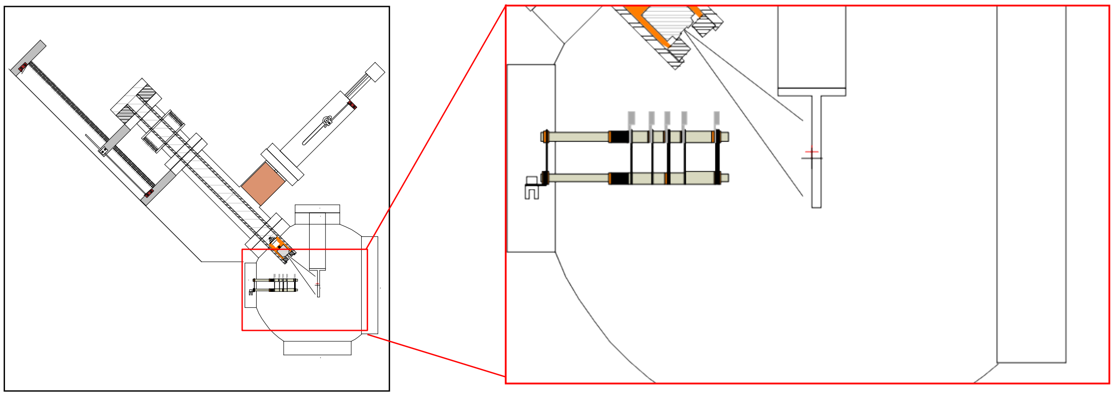

Figure 26. Ion optics package schematic

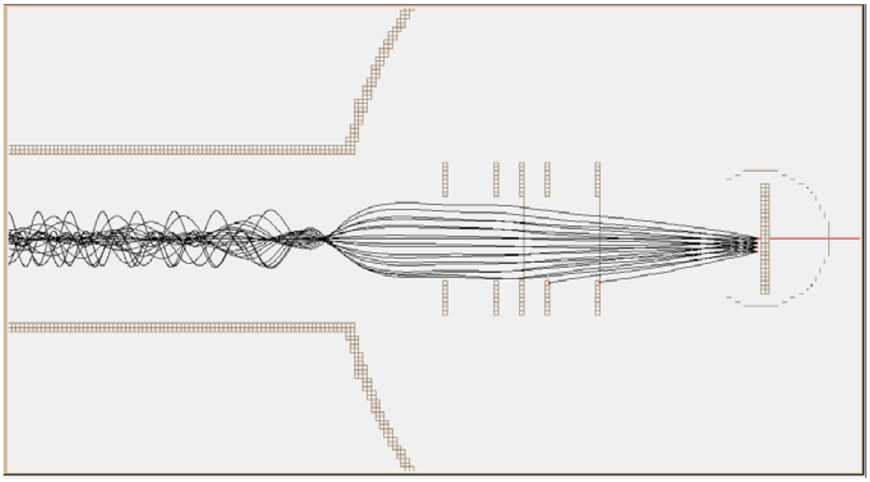

Figure 27. SIMION trajectories, RPA “On”
KE = 2 eV, V_1 = 40 V, V_2 = -40 V, V_3 = 15 V, V_4 = 30 V, V_5 = 15 V, V_6 = -30 V, |B| ≈ 50 G

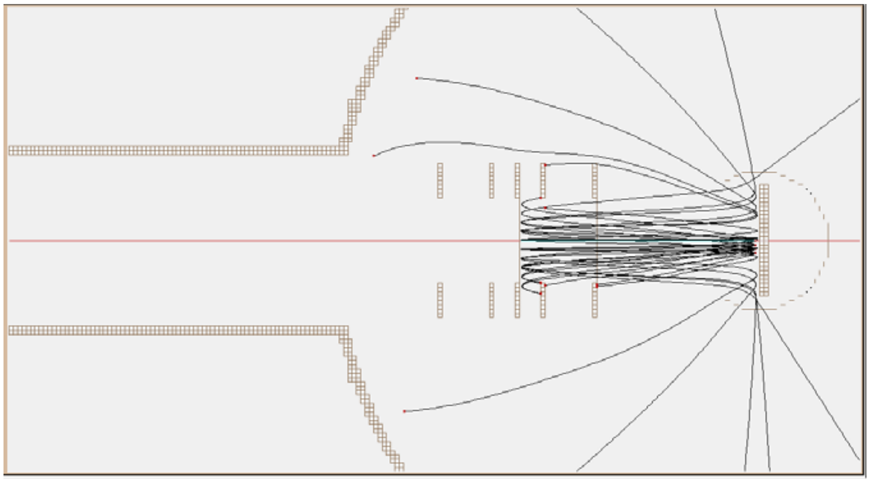

Figure 28. SIMION trajectories, RPA “Off”
KE = 2 eV, V_1 = 40 V, V_2 = -40 V, V_3 = 15 V, V_4 = 40 V, V_5 = 15 V, V_6 = -30 V, |B| ≈ 50 G

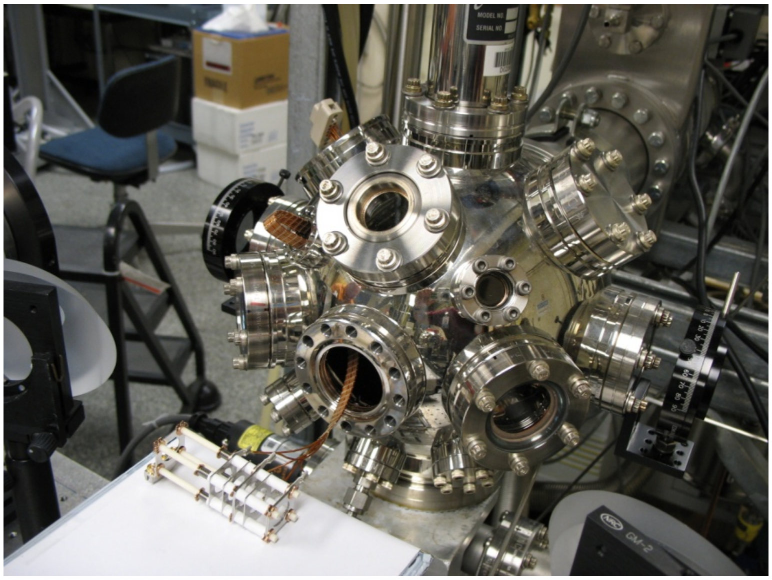

Figure 29. Photo of ion optics package installation

Our ion optics package design started with five equally spaced elements, and evolved by trial-and-error with the SIMION simulations providing the performance feedback. Initially, we just pursued the most efficient collection and transport of positrons from the largest moderator area. However, we found this to be incompatible with acceptable RPA energy resolution, which requires perpendicular positron trajectories across the central blocking element. Indeed, the RPA only measures the positron momentum component ($p_\perp$) perpendicular to the blocking electrode surface, so V_4 actually measures the positron "perpendicular KE" defined as $KE_\perp \equiv p_\perp^2 / 2m_e$. Our final design is a compromise between positron collection efficiency and RPA resolution. Figures 29 and 30 are photos of the ion optics package during and after installation.

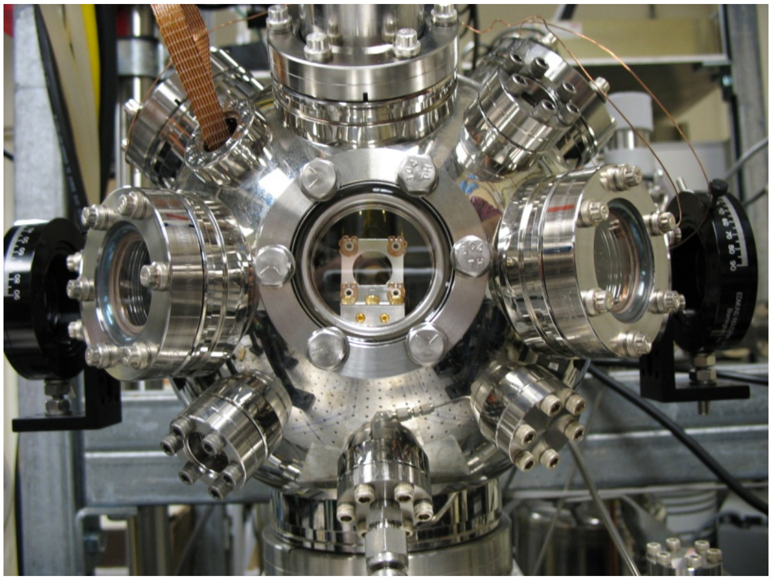

Figure 30. Photo of ion optics package in place

2.E. Slow Positron Detection in a Separate Annihilation Chamber

We detect the slow moderated positrons arriving in the Annihilation chamber by two independent techniques: single charged particle detection with a channel electron multiplier (CEM), and γ–γ coincidence detection of the annihilation radiation with a pair of NaI(Tl) detectors. The CEM approach has a much higher detection efficiency, but the γ–γ coincidence signal is an unambiguous fingerprint for positrons. Figure 31 shows the CEM bias circuit we built to facilitate switching between detecting positive and negative particles. Figure 32 shows the energy spectrum from one of our NaI(Tl) detectors; for the coincidence measurements we set the discriminators to accept signals in the 100-600 keV energy range.

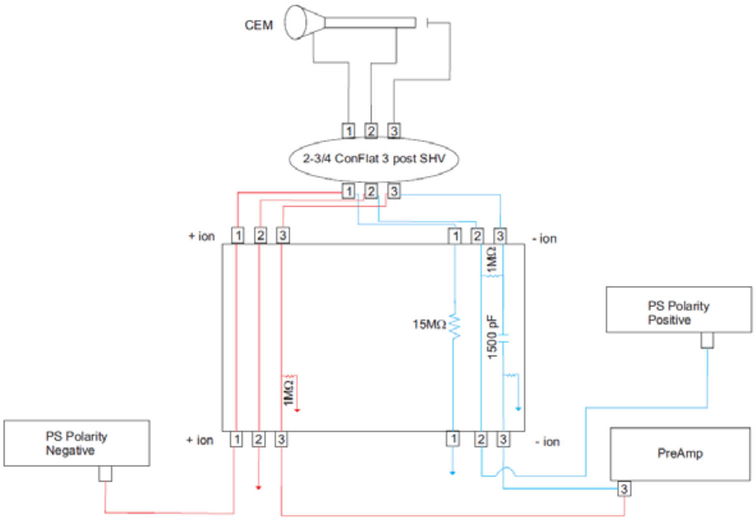

Figure 31. Reversible polarity CEM bias circuit schematic

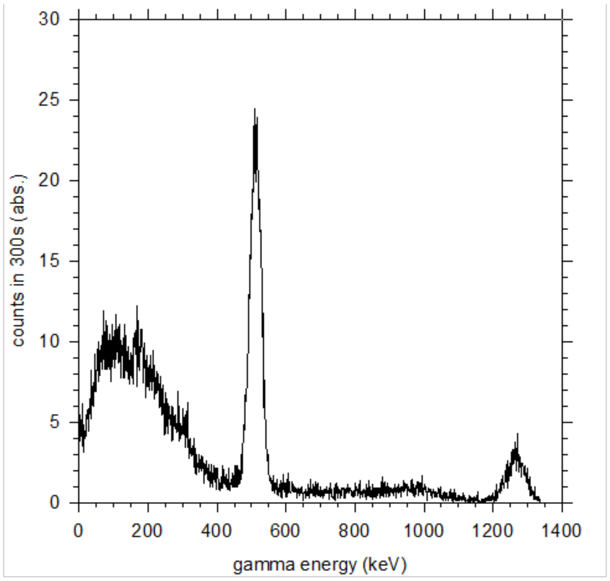

Figure 32. NaI(Tl) gamma spectrum of 1 μCi ^{22}Na check source [MF12067D]

2.F. Listing of Apparatus Configurations

Our apparatus has existed in five different configurations: (1) an isolated Moderation chamber for production and spectroscopic characterization of cryogenic solids, (2) a connected Moderation-Transport-Annihilation vacuum system with a hot filament electron source in the Moderation chamber, (3) a nearly complete apparatus sans ^{22}Na source for photoelectron transport experiments, (4) the first complete positron moderation apparatus with ^{22}Na source shown in Figure 33, and (5) the final configuration shown in Figure 34 with a small Annihilation chamber to improve the γ–γ coincidence signals by bringing the NaI(Tl) detectors closer.

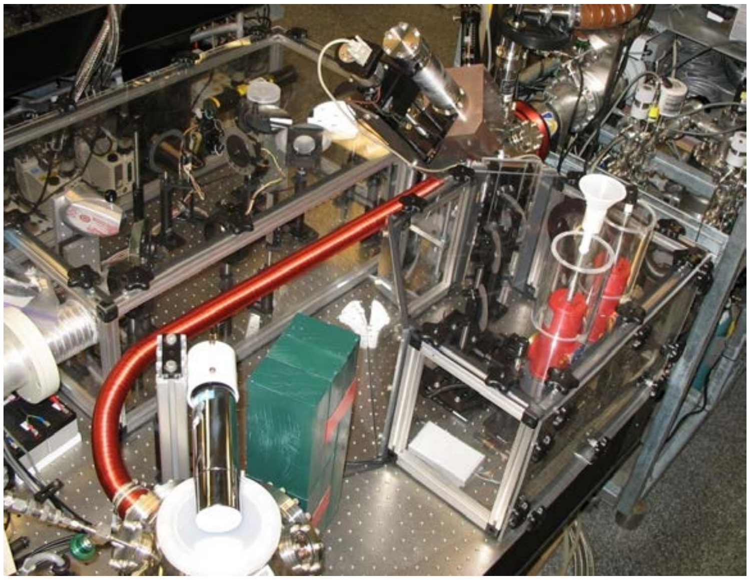

Figure 33. Photo of first complete positron moderation apparatus

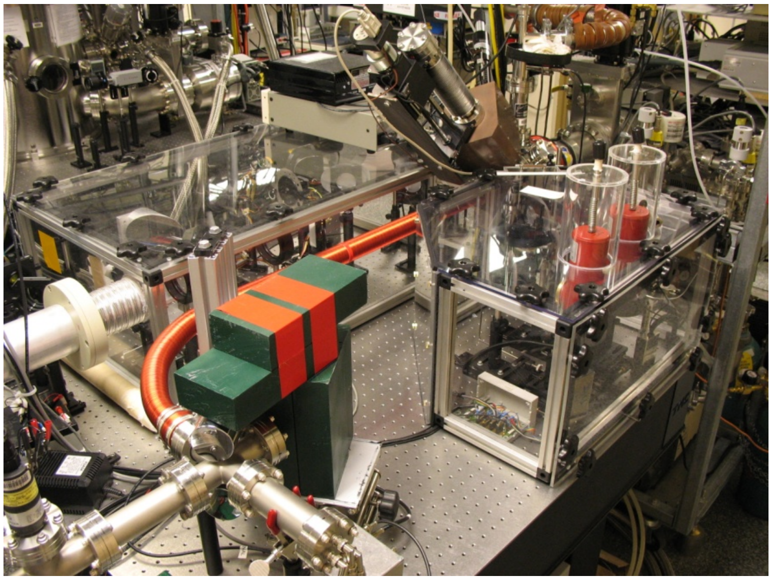

Figure 34. Photo of final positron moderation apparatus

3. RESULTS

3.A. Production and Characterization of cryogenic pH_2 Solids

3.A.1. Comparison of CO/pH_2 solids grown on BaF_2 and Au/Cu substrates

Our earliest solid pH_2 deposition experiments were performed to compare the samples produced in our new apparatus with those from our earlier Edwards AFB HEDM program studies. Figure 35 shows a direct comparison of IR absorption spectra for two such samples. The small vertical arrows in traces (a) in both figures indicate features due to CO molecules in metastable fcc trapping sites, which have disappeared from the spectra of the annealed samples shown in the upper (b) traces. The slightly higher deposition substrate temperature in our new apparatus (2.9 K *vs*. 2.4 K) apparently results in slightly sharper spectral features for the as-deposited samples. Overall, the observed changes are minor and easily understood, and should allow us to carry over most if not all the lessons learned in our earlier studies.

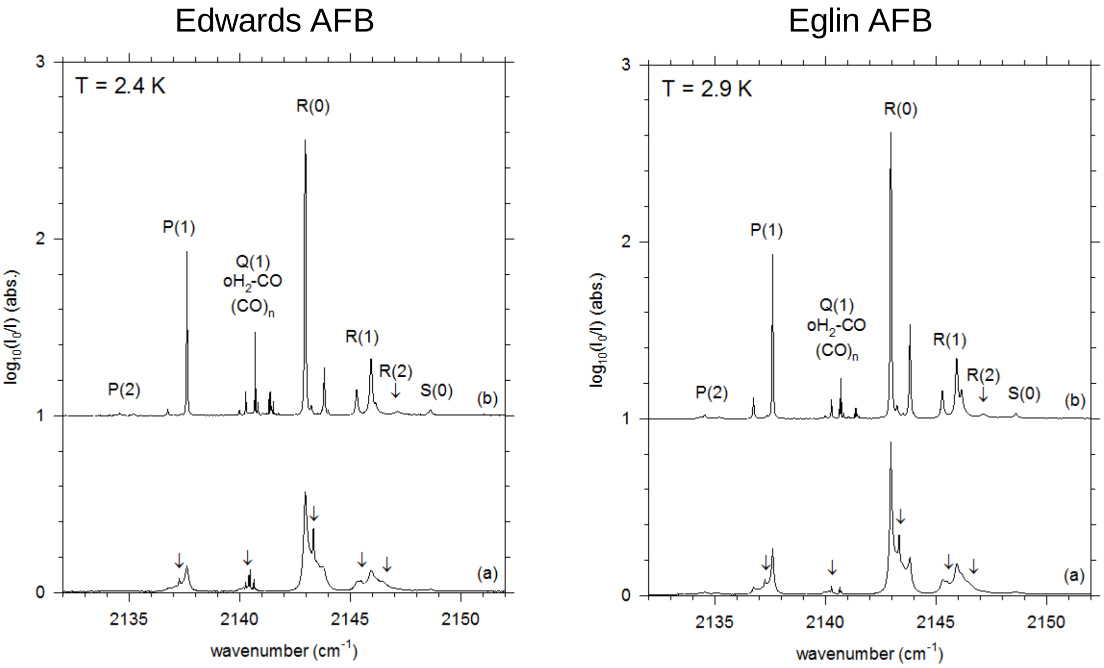

Figure 35. Comparison of spectra of CO/pH_2 samples grown on BaF_2 and Au/Cu [63] [ST27017, MF11093]

3.A.2. PIRAS data for pH_2 solids grown on Au/Cu substrate

PIRAS spectra of the R(0) lines in Figures 36 and 37 show equal positive and negative intensity, implying good alignment of the hcp crystallite axes with the deposition substrate surface normal, as discussed in detail in Appendix B. One possible explanation for this alignment is that the as-deposited pH_2 crystallites have "sintered" together during annealing to form larger crystallites. We had initially hoped that this would result in even greater positron moderation efficiencies for annealed pH_2 samples.

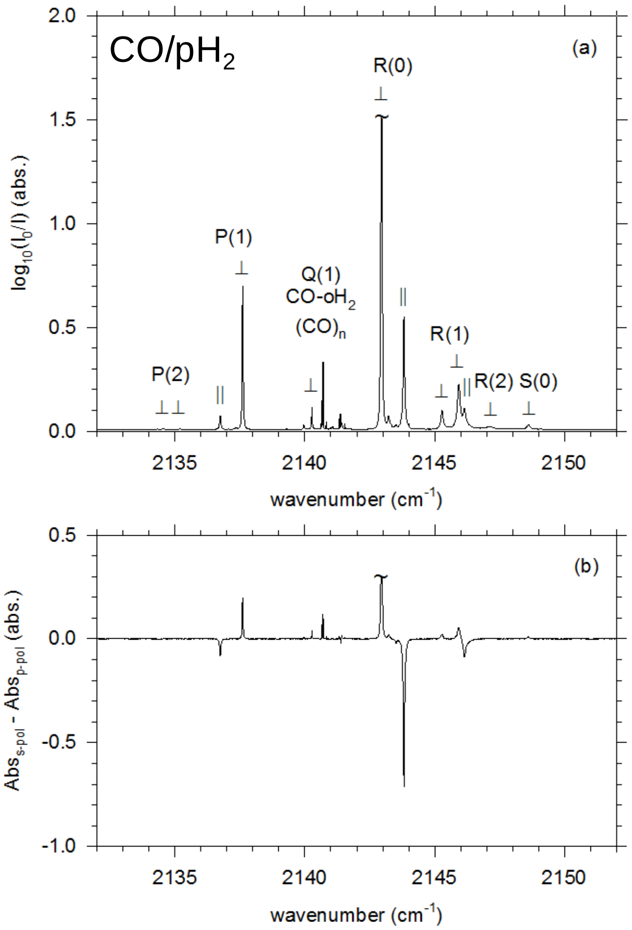

Figure 36. PIRAS spectra of annealed CO/pH$_2$ sample [63] [ML01107]

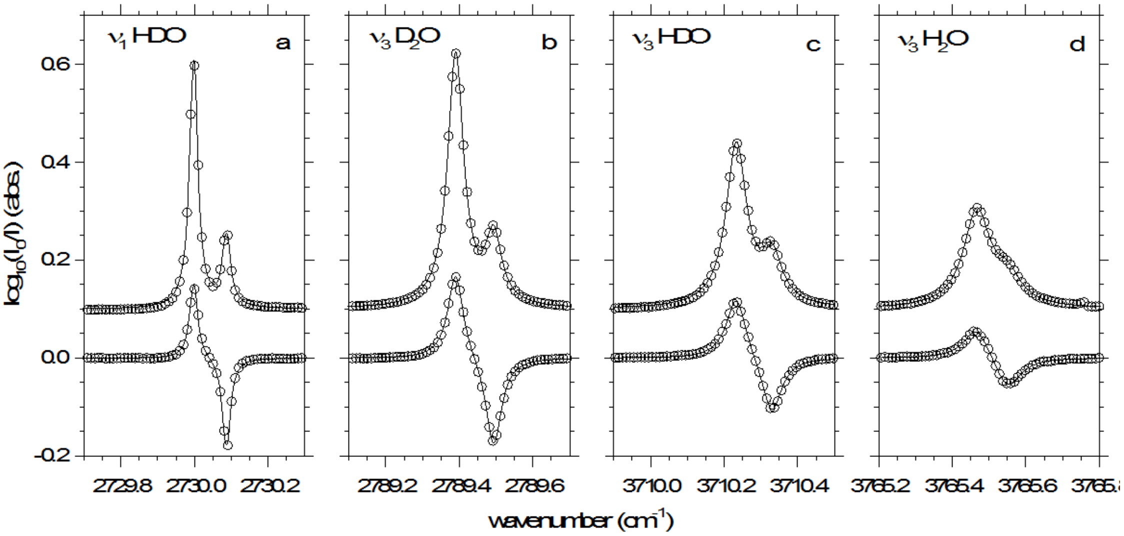

Figure 37. PIRAS spectra of annealed water/pH$_2$ sample [62] [ML02007]

3.A.3. Polarized optical microscopy of pH_2 solids

Since the hcp pH_2 crystallites are weakly birefringent, we tried to photograph them in polarized light. Figure 38 shows photomicrographs of a 2.53-mm-thick pH_2 solid as-deposited on a T = 2.7 K Au/Cu substrate. We pass diffused light from a 20 W tungsten-halogen lamp through a linear polarizer, reflect off the substrate at near normal incidence, then through a second polarizer just before the CMOS camera. The camera lens is focused at the Au/Cu surface, and surface pits and scratches are readily visible through the pH_2 solid. We see no structures attributable to microcrystallites, although macroscopic (~100 μm) "bubbles" in the pH_2 solid are clearly visible as "double images," seen directly and reflected off the substrate.

Figure 39 is a side view through crossed polarizers (see Figures 29 & 30) during the growth of a 2.43-mm-thick pH_2 solid at T = 2.7 K. It is worth noting that the variation in sample thickness across the field of view is due to the upward-facing orientation of the cold pH_2 gas delivery tube, and we expect that a similar variation is present in all our cryogenic solids.

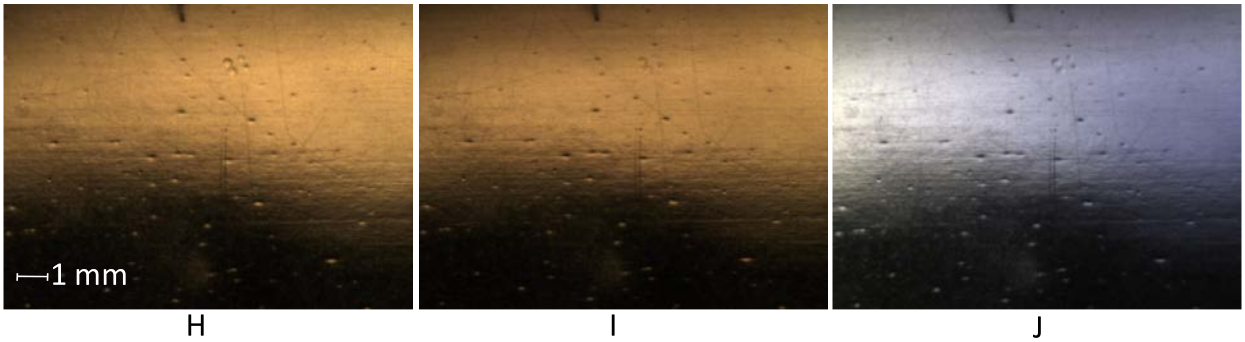

Figure 38. Micrographs of 2.53-mm-thick pH_2 solid in polarized light at near-normal incidence H = s & s; I = p & p, and J = p & s polarizer orientations, respectively [CM01051H-J]

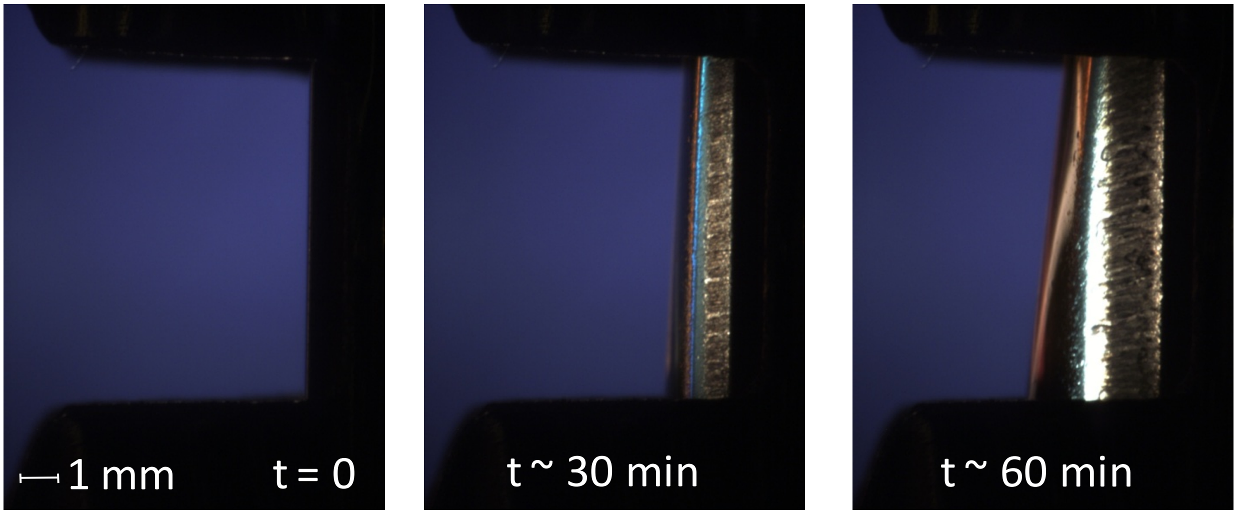

Figure 39. Micrographs of growth of pH_2 solid in crossed-polarizers [MF11113C2, MF11113C180, MF11113C360]

3.B. Electron Transport and Detection Experiments

3.B.1. Picoammeter detection

Figure 40 shows results of magnetically-guided electron transport experiments through the bent tube joining the Moderation and Annihilation chambers. A 6.0 A solenoid current yields a centerline magnetic field |B| ≈ 30 G. A Faraday plate collects the electrons arriving in the Annihilation chamber, and we measure this current with a picoammeter. In the left panel of Figure 40, we induce thermionic electron emission by running ≈ 2 A through a bent 130-μm-diameter tungsten wire cathode, heating it to a bright yellow visible emission. We bias the cathode to a repulsive potential $V_1 = -20$ V. This configuration exhibited several artifacts, likely due to space-charge effects, which should be irrelevant to our low-flux positron experiments.

The right panel of Figure 40 shows the photocurrent in the Annihilation chamber during illumination of the Au/Cu substrate with an unfiltered Hg/Ar penlamp placed just outside the MgF_2 window located at the end of the positron source manipulator chamber (see Figure 10). In this case, the substrate bias was - 40 V, and we used a 10.0 A solenoid current for |B| ≈ 50 G.

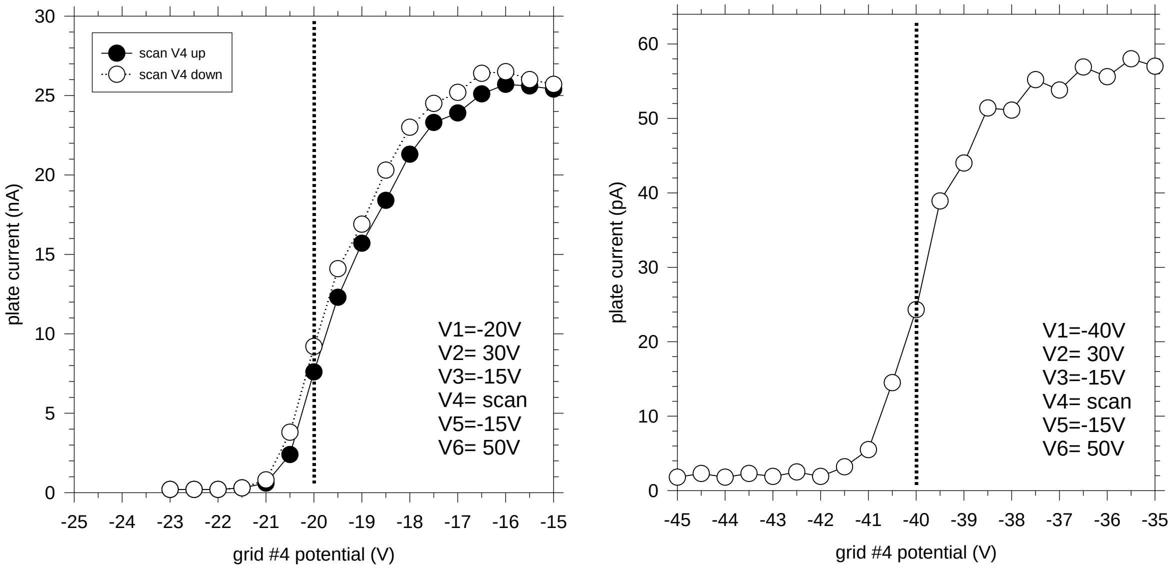

Figure 40. Picoammeter detection of thermionic & photo-electrons [CM02081, CM02107]

3.B.2. Apparatus fine tuning

We performed an extensive search over the ion optics voltage and solenoid current parameter space to find optimum operating conditions. We found that our signals were sensitive to a variety of environmental effects; *e.g.*: opening and closing a nearby steel-core door resulted in ≈ 10% changes to the measured current. Figure 41 shows SIMION calculations of magnetic fields and electron trajectories with and without an additional solenoid intended to straighten out the field at the entrance to the bent tube "magnetic funnel." Its addition helped to alleviate some problems; however, the SIMION calculations suggest the new troubling possibility of electron trajectories entering the solenoid after bypassing the ion optics package.

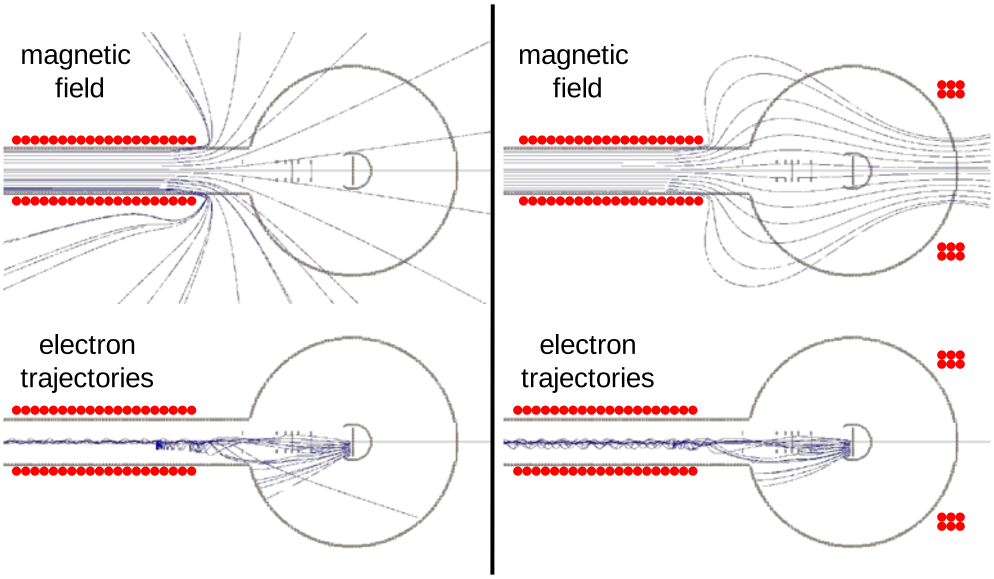

Figure 41. SIMION calculations of electron trajectories in solenoid "magnetic funnel"

As shown in Figure 42, we also found that we could increase our signals by placing small permanent magnets: (1) just inside the bend of the magnetically-guided transport tube, and (2) axially at the back end of the Annihilation chamber to mimic the field-straightening effects shown for the Moderation chamber in Figure 41. Finally, when we eventually switched to detecting slow positrons we found that we had to reverse the direction of the currents in all the solenoids, as well as reverse the orientations of the permanent magnets. These modifications combined increased the slow positron signal levels by a factor of 2-3. We speculate that this asymmetry is introduced by the left-hand turn made by the particles as they spiral down the magnetically-guided transport tube.

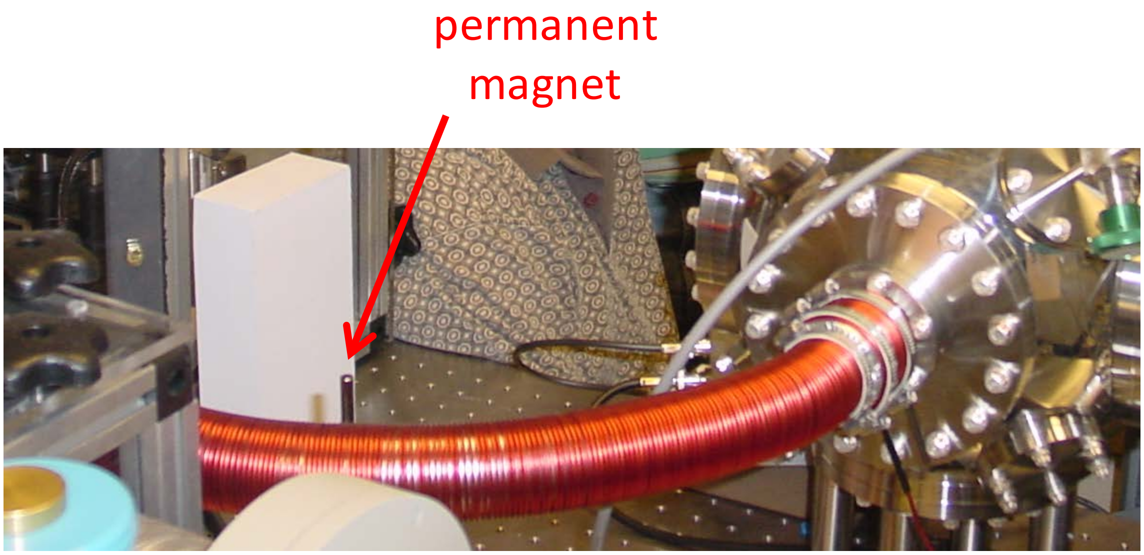

Figure 42. Photo of small permanent magnet at solenoid bend

3.B.3. CEM Detection

For the endgame of our operating parameter optimization, we switched to single charged particle detection of the photoelectrons using a CEM biased to detect negative particles, as shown in Figure 31. Figure 43 shows photoelectron RPA scans in which we used notch-bandpass optical filters to isolate individual lines from the Hg/Ar penlamp. We also used small pinhole apertures (1.0-mm-diameter for 253.73 nm, and 0.20-mm-diameter for 184.95 nm) to bring the signal levels down to ≈ 3000 cps in the RPA "On" state.

These data raise a few peculiar issues worthy of comment. First, the upper limit to the KE of the photoelectrons is given by [74]:

$$KE_{max} = hc / \lambda_{vac} - \Phi^{-}_{Au} \quad (5)$$

where: h is Planck's constant, c is the speed of light in vacuum, λ_{vac} is the vacuum wavelength of the Hg emission line, and Φ^{-}_{Au} is the electron work function of gold. Since the 253.73 nm Hg line (with a photon energy of 4.89 eV) apparently produces copious numbers of photoelectrons from a gold surface, for many decades the work function of gold was given as somewhere in the 4.0 to 4.8 eV range [75]. The modern value for a clean, freshly deposited gold surface under UHV conditions is $\Phi^{-}_{Au} \approx 5.4$ eV, and the lower historical values are attributed to adsorption of oxygen and other gases [76]. Second, it is very difficult to extract the 6.70 - 4.89 = 1.81 eV difference in photon energies for the 184.95 and 253.73 nm lines from the data in Figure 43. The conventional method [74] of extrapolating a plot of $(\text{signal})^{½}$ vs. V to find the threshold yields a difference of ≈ 1.5 eV. This is probably due to the fact that the angular distribution of the photoelectrons is very different for the two wavelengths. Finally, we note that even with the near-threshold 253.73 nm, the voltage difference between 10% and 90% signal levels (ΔV_{10-90}) is about 1.2 eV, which is an upper bound to the instrumental resolution for our apparatus.

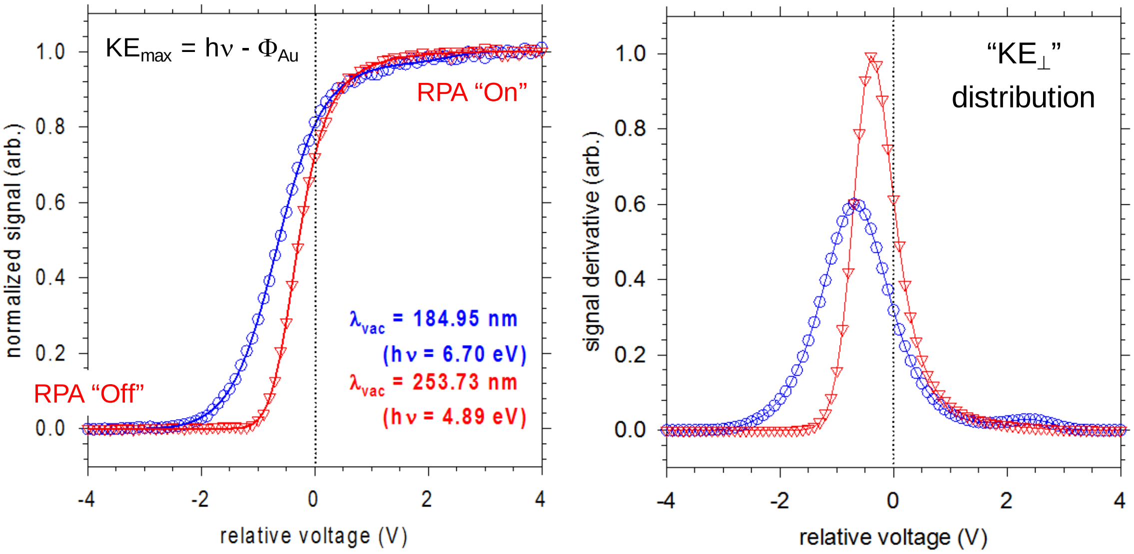

Figure 43. Photoelectrons from Au/Cu substrate with two Hg lines [CM03039CG & CH]
V_1 = -40 V, V_2 = 30 V, V_3 = -10 V, V_4 = scan, V_5 = -10 V, V_6 = 40 V, |B| ≈ 30 G

3.C. Positron Moderation Experiments in Nominally "Pure" Moderators

3.C.1. Solid Ne

Our first few attempted positron moderation experiments were plagued by a number of unexpected problems, including: a thermal short caused by the detachment of an internal mechanical alignment insert in the lHe transfer cryostat, an electrical short between the deposition substrate and the lHe cryostat cold tip caused by a rogue sliver of indium metal foil, a pathologically intermittently faulty single-channel analyzer in the CEM detection electronics that took several days to identify and replace, and poor vacuum levels due to the repeated venting of the vacuum chambers to atmosphere for troubleshooting.

As shown in Figure 44, we eventually managed to fix these problems, seal up the UHV system and pump down long enough to establish a pre-cooldown residual water vapor level of $4\text{x}10^{-7}$ torr, and deposit a (barely) functional solid Ne moderator. As we repeat several times in the data presented below, the upper panel shows the scanning of the RPA blocking element with the initial bias potential for the deposition substrate shown as a horizontal line. Unless stated otherwise, all our positron moderation experiments were performed with the RPA configuration: V_1 = 40 V, V_2 = -45 V, V_3 = 15 V, V_4 = scan, V_5 = 15 V, V_6 = -40 V, and a solenoid field |B| = 30 G. The middle panel shows the absolute CEM counts with the counting time interval specified in the vertical axis label. The bottom panel shows the substrate temperature which responds sensitively to the varying deposition heat load. Note that in this experiment the poor vacuum results in a strong dependence of the moderation efficiency on the rate of Ne deposition; *i.e*. faster deposition correspond to a "cleaner" moderator and stronger slow positron signals.

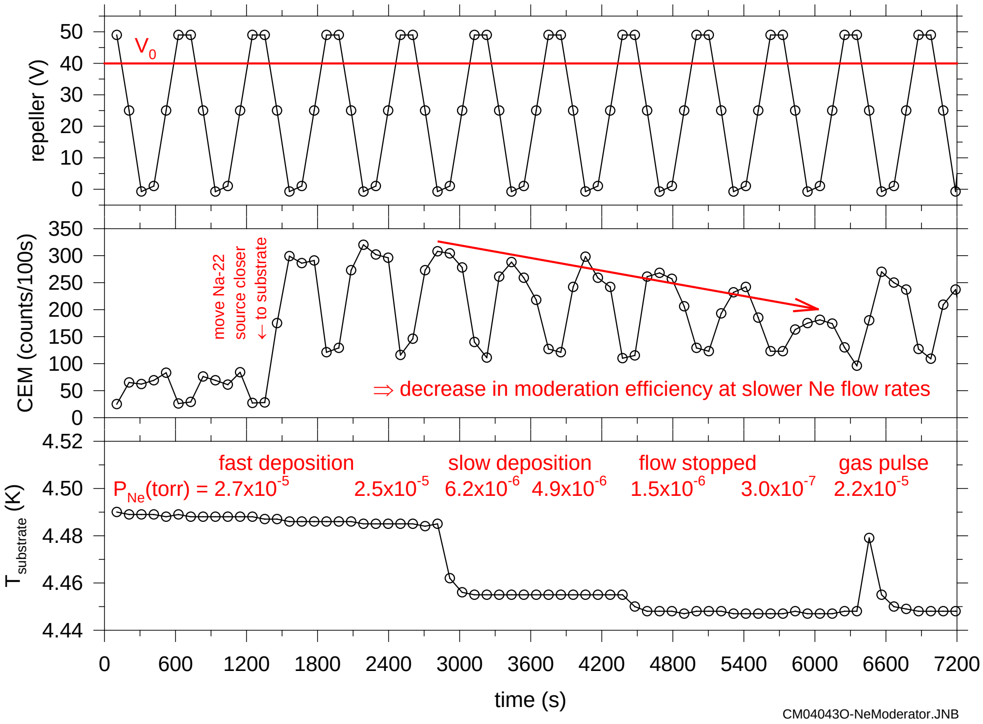

Figure 44. First plausible positron moderation signals [CM04043O]

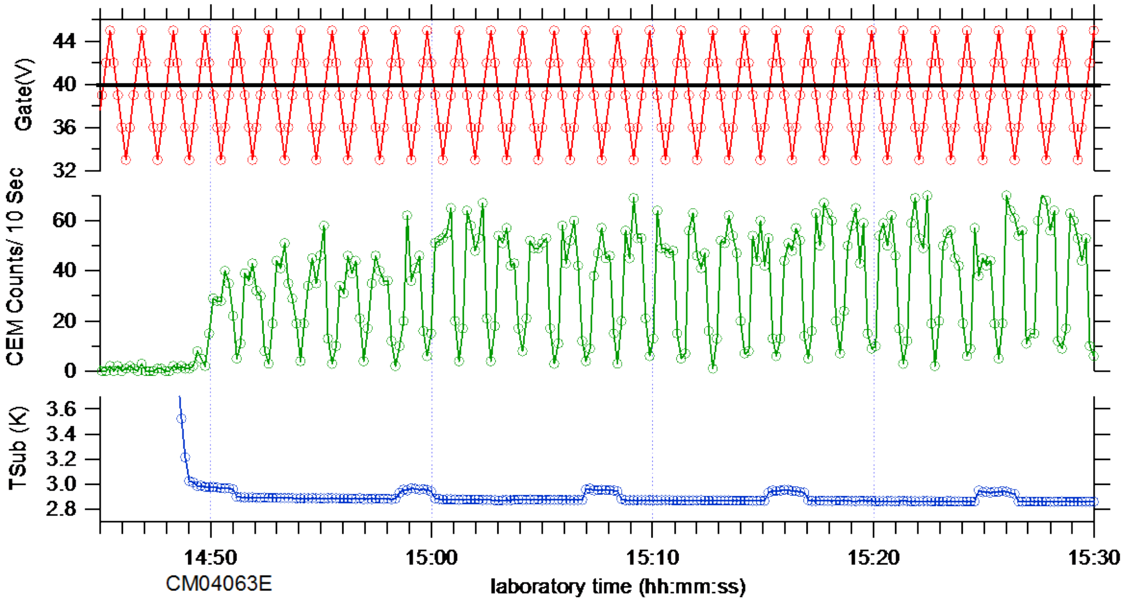

Figure 45. 13.5-µm-thick Ne moderator deposited from dopant manifold T_{sub} = 2.9 K, $T_{o/p}$ = 6.4 K, 2.1 mmol Ne, $\Sigma t_{dep} \approx$ 8 min [CM04063E]

Figure 45 shows subsequent results for a somewhat "cleaner" Ne moderator grown by depositing Ne gas from the dopant manifold, and with the Moderation chamber at a pre-cooldown vacuum of 1×10^{-8} torr. Figure 46 shows the interference fringes used to calculate the 13.5 µm sample centerline thickness, as well as absorption features due to water monomers and small clusters isolated in the solid Ne [62,77]. The distribution of $(H_2O)_n$ cluster sizes inferred from the intensities of the absorption features suggests a water concentration in the 100-1000 ppm range.

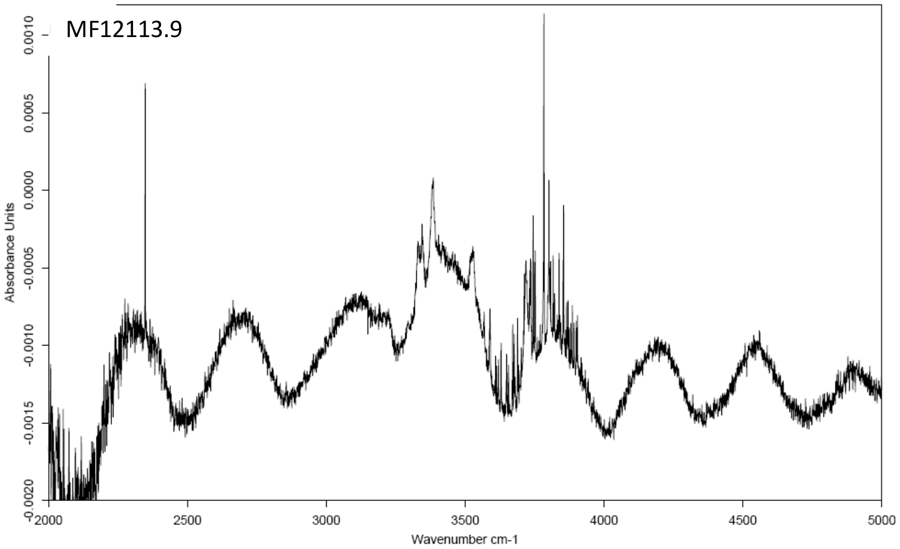

Figure 46. IR absorbance spectrum of sample depicted in Figure 45 [MF12113.9]

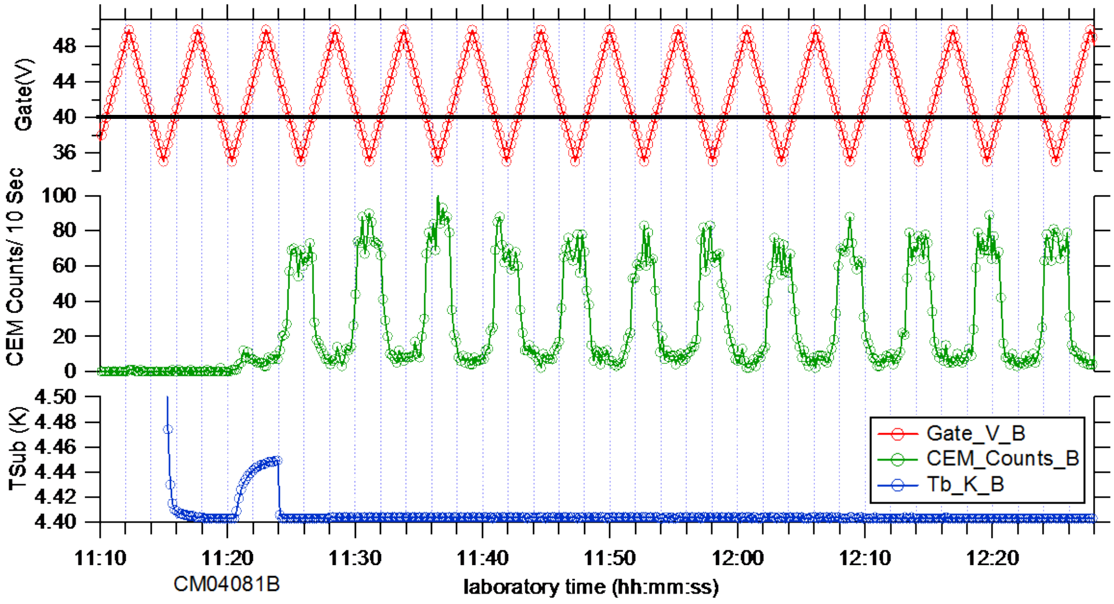

Figure 47. 8.3-µm-thick Ne moderator deposited through cold o/p-converter T_{sub} = 4.4 K, $T_{o/p}$ = 27.0 K, 1.38 mmol Ne (11:20:30 to 11:24:00) [CM04081B]

Figure 47 shows data for a much cleaner, thin Ne moderator grown by flowing the Ne gas through the cold o/p converter at $T_{o/p}$ = 27.0 K to remove any condensable impurities (*e.g.* H_2O, CO_2, N_2, O_2). By this time, the vacuum system had been sealed for roughly a month, and the pre-cool down residual water vapor level had reached its floor of $\approx 1\times10^{-9}$ torr. Figure 48 shows very weak trapped water monomer absorptions, which are hidden in the ± 0.003 absorbance noise. This moderator retains constant moderation efficiency for the ≈ 1 hour duration of the experiment.

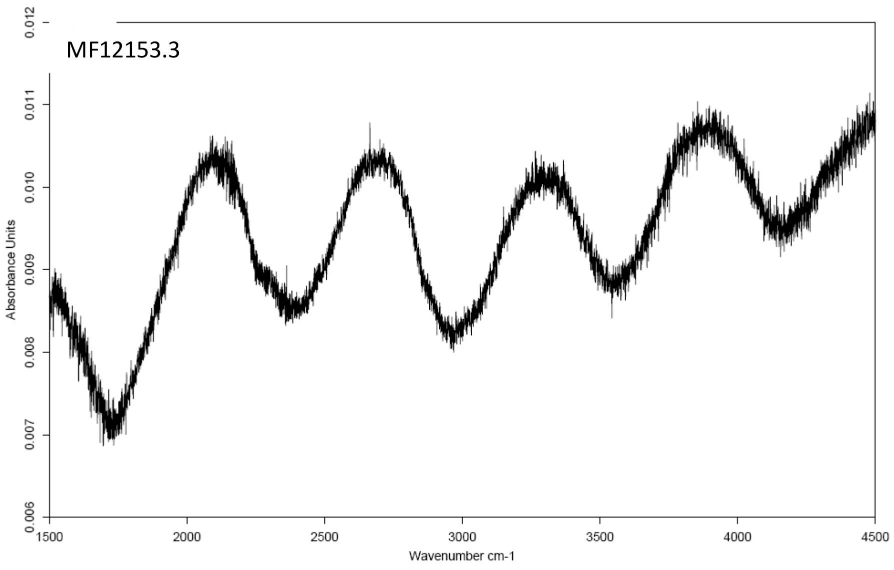

Figure 48. IR absorbance spectrum of sample depicted in Figure 47 [MF12153.3]

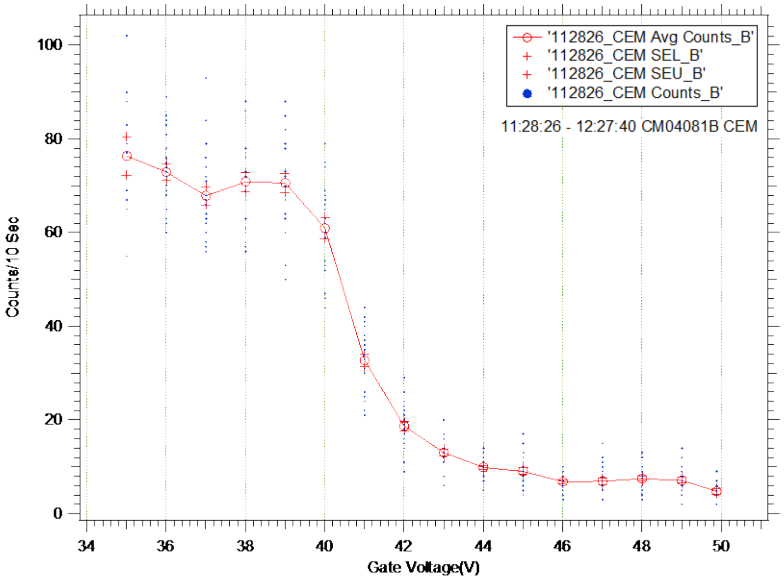

Figure 49. Compiled RPA scans from data shown in Figure 47 [CM04081B]
<On> = 7.3 cps, <Off> = 0.5 cps, 50% @ 40.6 V, $\Delta V_{10\text{-}90}$ = 3.1 V

Figure 49 shows the CEM data from Figure 47 plotted *vs*. the RPA blocking electrode potential, V_4. Each datum appears as a blue dot; open red circles show the CEM signal averages, and red crosses show the standard errors of the mean. The caption gives the average counting rates in the RPA On and Off states, the "50%" point halfway between these asymptotes, and the voltage difference between 10% and 90% signal levels, $\Delta V_{10\text{-}90}$. Lacking an analytical expression for the RPA curve, we estimate these parameters graphically, *i.e*. with pen and paper.

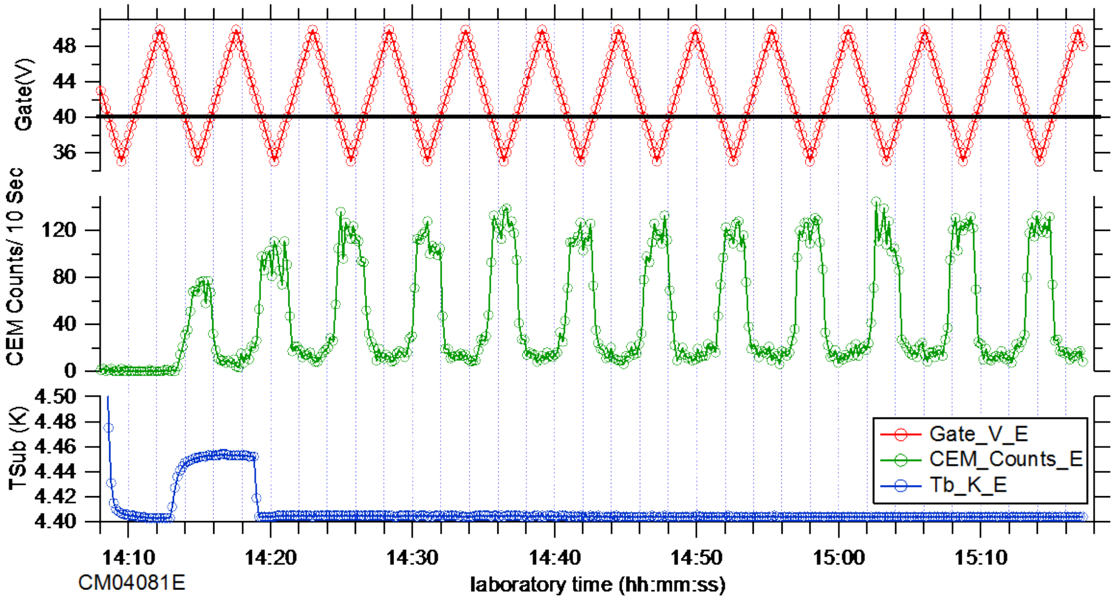

Figure 50. 17.9-µm-thick Ne moderator deposited through cold o/p-converter
T_{sub} = 4.4 K, $T_{o/p}$ = 27.0 K, 2.62 mmol Ne (14:13 to 14:19) [CM04081E]

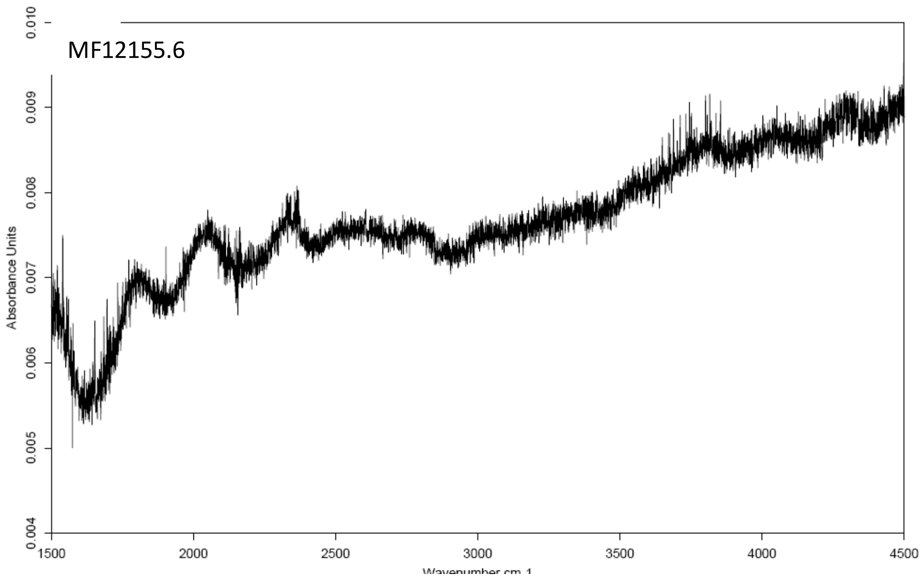

Figure 51. IR absorbance spectrum of sample depicted in Figure 50 [MF12155.6]

Figure 50 shows results for a clean, medium thickness Ne moderator grown through the cold o/p converter. This moderator also retains its as-deposited moderation efficiency for the 1 hour duration of the experiment. Figure 51 still retains some helpful interference fringes for determining the moderator centerline thickness, and only very weak trapped dopant absorptions. Figure 52 shows the compiled and averaged RPA scans, with the difference in RPA On and Off absolute counting rates reaching the 10 cps level.

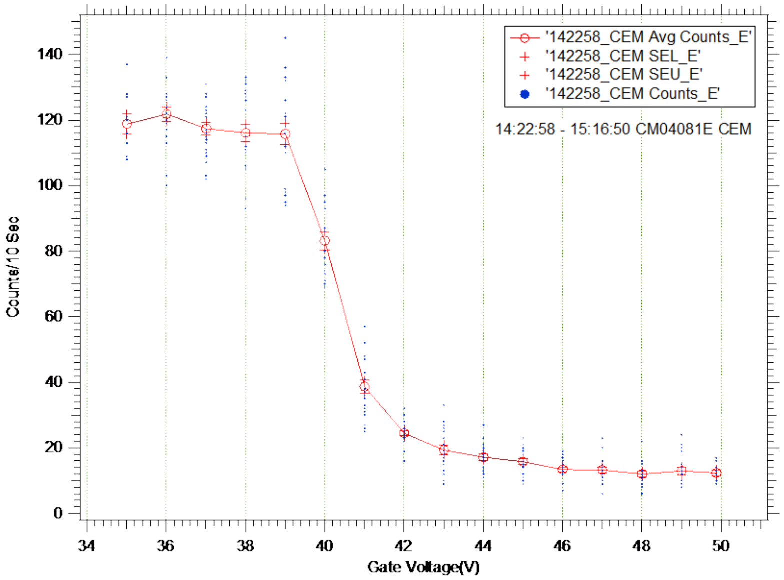

Figure 52. Compiled RPA scans from data shown in Figure 50 [CM04081E]
<On> = 11.9 cps, <Off> = 1.2 cps, 50% @ 40.4 V, $\Delta V_{10\text{-}90}$ = 2.8 V

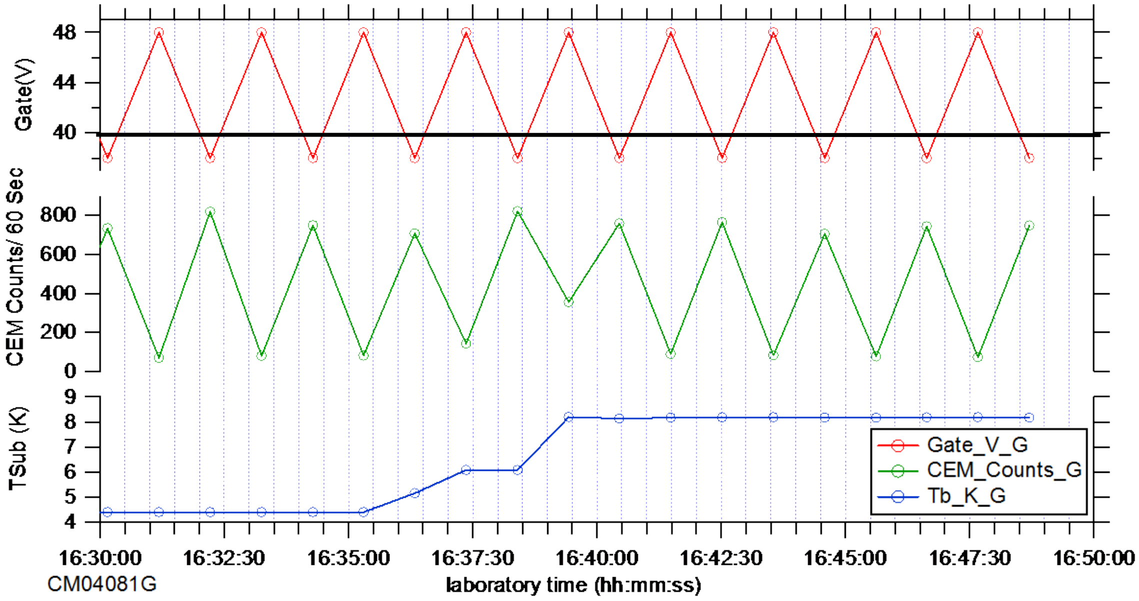

Figure 53. Ne moderator from Figure 50 during annealing at T ≈ 8 K [CM04081G]

Figure 53 shows annealing of the clean 17.9-µm-thick Ne moderator from Figure 50 to T ≈ 8 K. No significant changes to the RPA On or Off signals occur upon warm up. Figure 54 shows the acquisition of the RPA scan data compiled in Figure 55. While we might have expected some noticeable changes to, say, the width of the On-Off transition, or to the position of the midpoint, these data compare well with those for the as-deposited sample shown above in Figure 52.

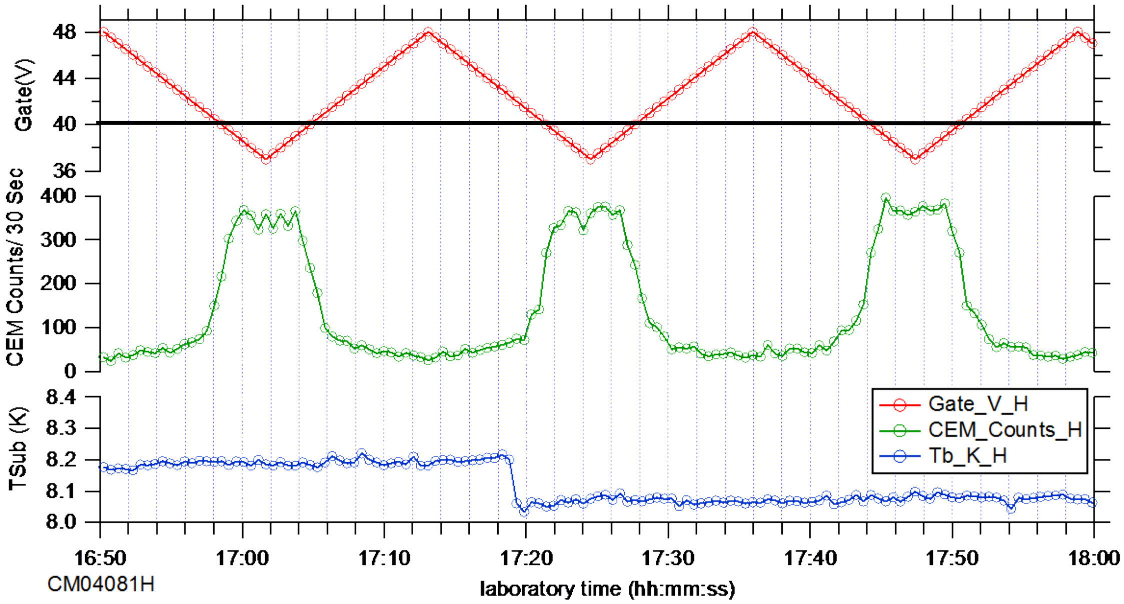

Figure 54. Ne moderator from Figure 50 after annealing [CM04081H]

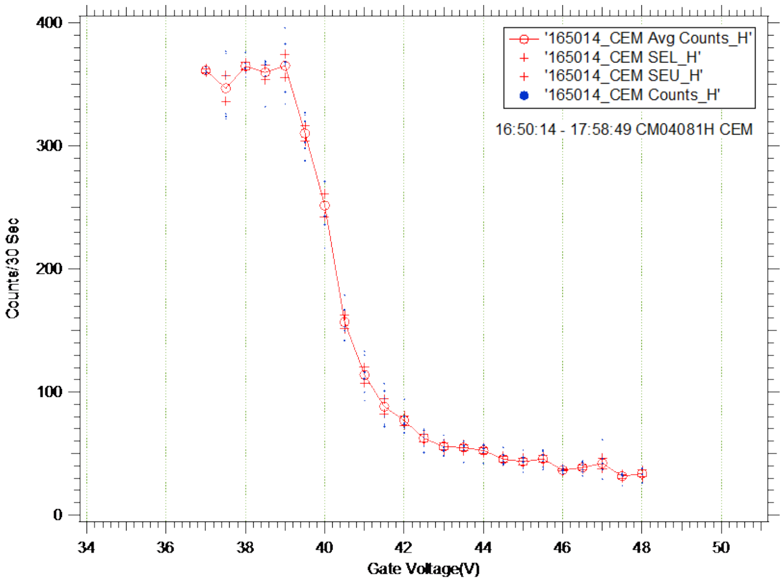

Figure 55. Compiled RPA scans from data shown in Figure 54 [CM04081H]
<On> = 12.0 cps, <Off> = 1.1 cps, 50% @ 40.2 V, ΔV_{10-90} = 2.8 V

Figure 56 shows the strongest slow positron signals observed in this study, with the difference in the RPA On and Off counting rates exceeding 20 cps. Figure 57 shows only vestigial transmission interference fringes, which makes any interferometric sample thickness determination suspect. Nonetheless, if we count five fringes separating the absorption maxima at 1867 and 2265 cm^{-1}, Equation. (4) yields a thickness of 62.4 μm, which agrees with the 60-65 μm thickness estimated from the amount of Ne gas deposited.

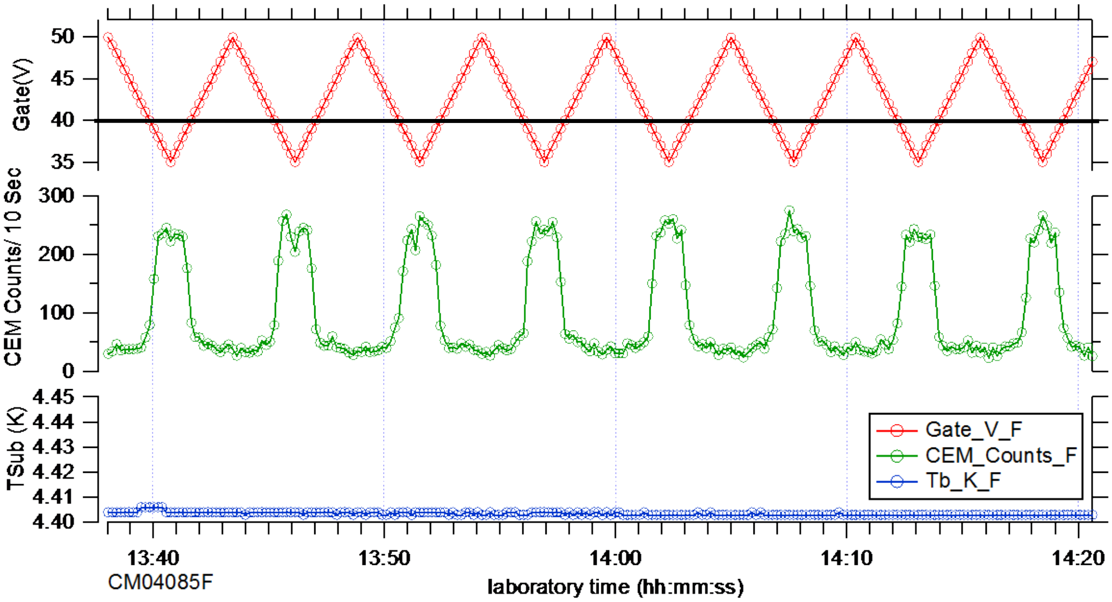

Figure 56. Strongest CEM signal observed from a Ne moderator [CM04085F]
d_{mod} = 62.4 μm, T_{sub} = 4.4 K, $T_{o/p}$ = 27.0 K, 8.79 mmol Ne (12:49 to 13:20).

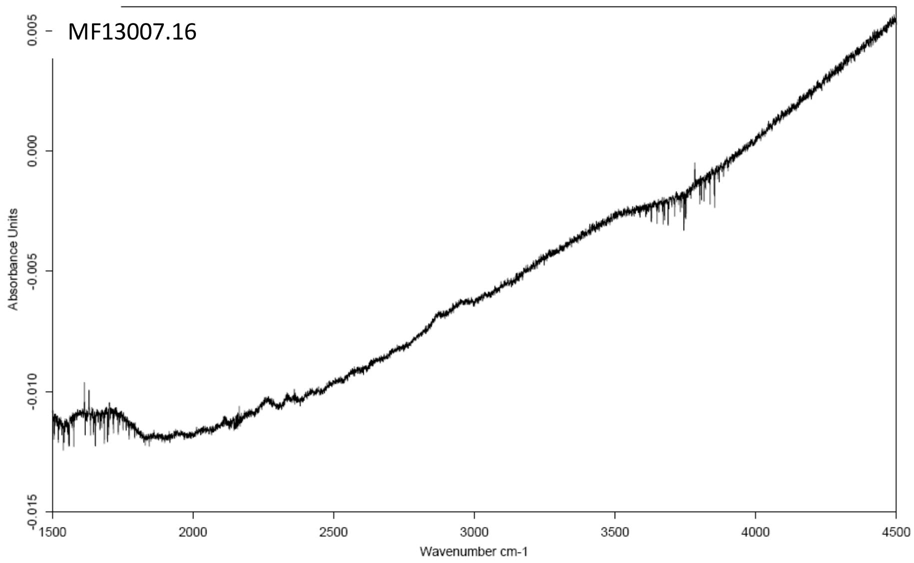

Figure 57. IR absorbance spectrum of sample depicted in Figure 56 [MF13007.16]

The compiled RPA scan data in Figure 58 appear to confirm two trends seen with increasing moderator thickness for the thin and medium thickness clean Ne moderators depicted above in Figures 47 and 50, *i.e.*: a shift in the 50% point to lower blocking potential, and a sharpening of the On-Off transition. One possible explanation for this is surface or bulk charging of the moderator by the accumulated radiation damage products produced by the fast positrons and gamma rays from the ^{22}Na source [78,79].

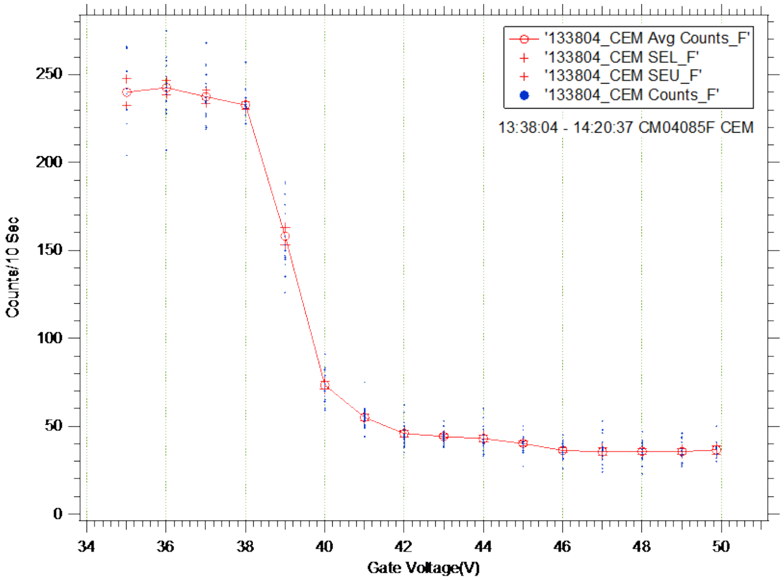

Figure 58. Compiled RPA scans from data shown in Figure 56 [CM04085F]
<On> = 24.0 cps, <Off> = 3.7 cps, 50% @ 39.2 V, $\Delta V_{10\text{-}90}$ = 2.6 V

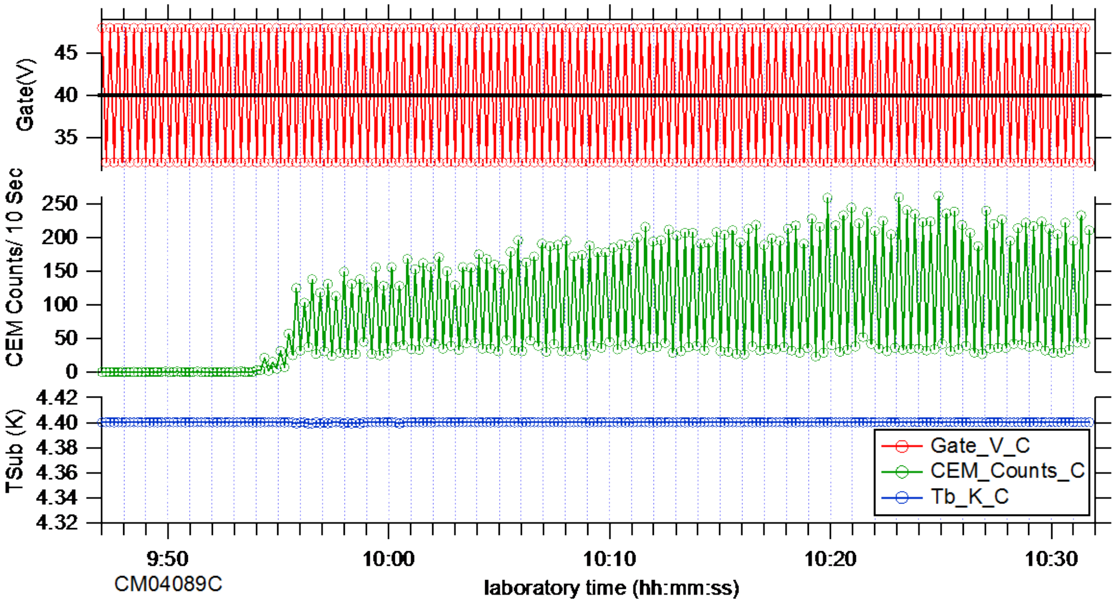

Figure 59. 24.8-μm-thick Ne moderator grown "in the dark" through cold o/p converter T_{sub} = 4.4 K, $T_{o/p}$ = 27.0 K, 2.78 mmol Ne (08:52 to 09:25) [CM04089C]

Figure 59 shows our attempt to observe this moderator charging process directly, during which we grow a clean medium thickness Ne moderator "in the dark," *i.e.* with the ^{22}Na source in the Storage mode depicted above in Figure 9. Note that all our other positron moderation experiments involve moderators grown under continuous irradiation by the ^{22}Na source in Active mode. Indeed, in Figure 59 the CEM signal in the RPA On state grows gradually, but significantly over the first 20 minutes of exposure of the as-deposited moderator to the ^{22}Na source. The CEM signal in the RPA Off state remains constant during the same time period.

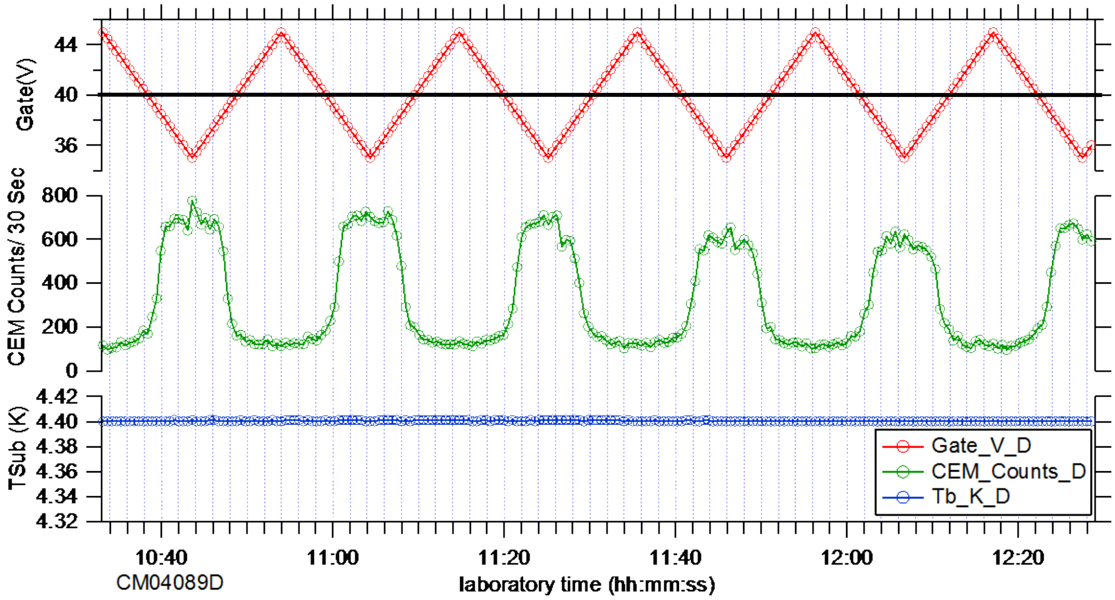

Figure 60. High-res RPA scans of sample depicted in Figure 59 [CM04089D]

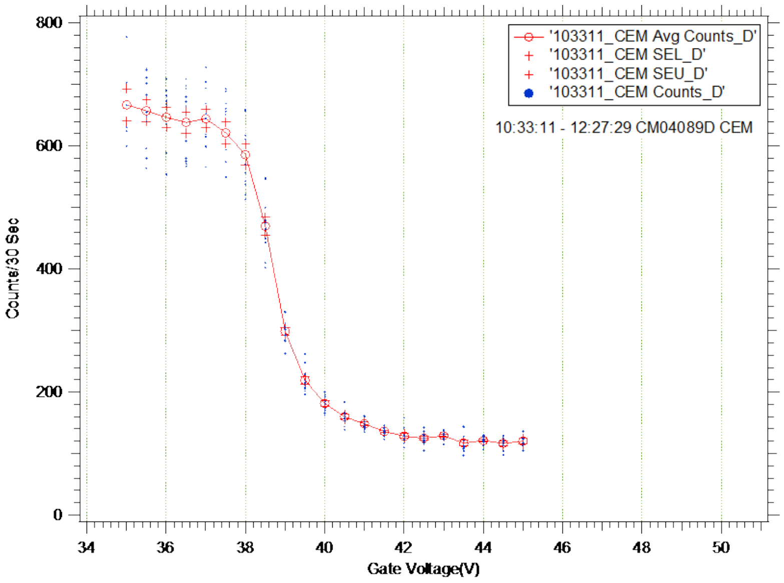

Figure 61. Compiled RPA scans from data shown in Figure 60 [CM04089D]
<On> = 21.5 cps, <Off> = 4.0 cps, 50% @ 38.8 V, $\Delta V_{10\text{-}90}$ = 2.4 V

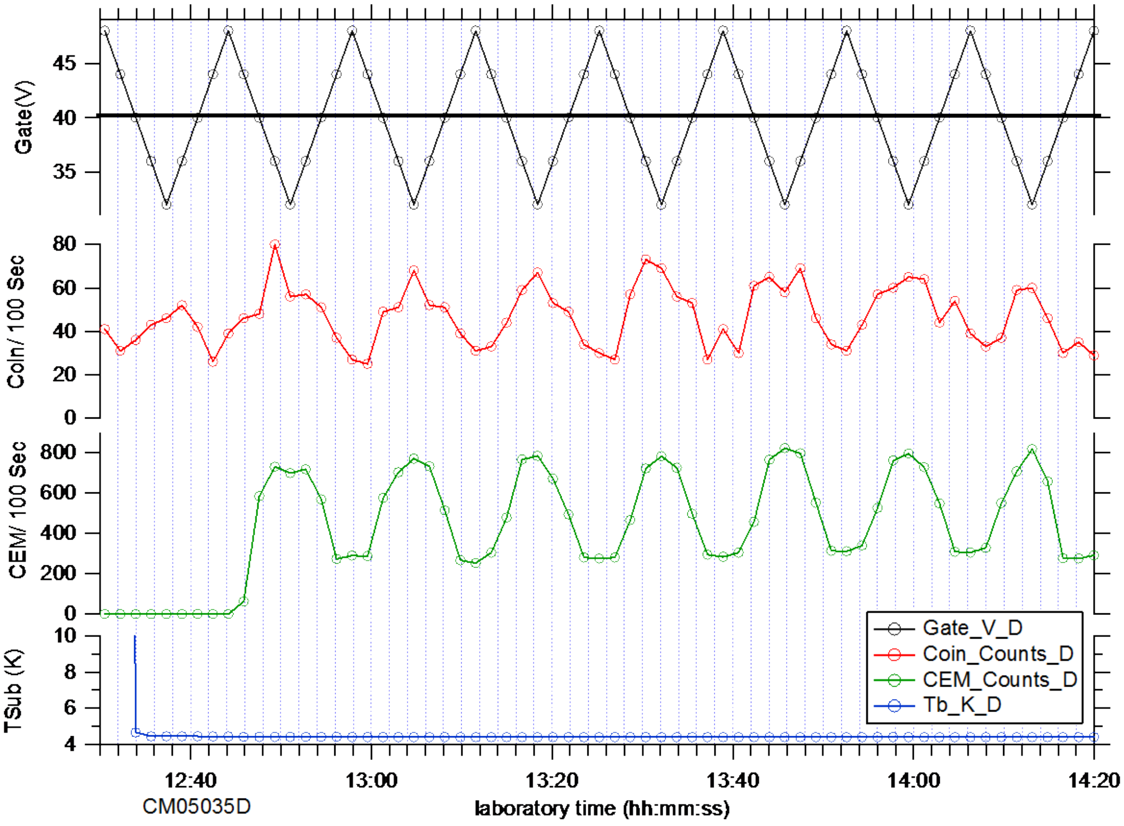

Figure 62. Correlation between CEM and γ–γ coincidence signals [CM05035D]
Ne moderator, d_{mod} =24.6 μm, T_{sub} = 4.4 K, $T_{o/p}$ = 27.0 K, 2.78 mmol Ne (12:35 to 12:45).

Figure 60 shows the acquisition of the high resolution ($\Delta V_4 = 0.5$ V) RPA scan data compiled in Figure 61. This experiment begins roughly 40 minutes after first exposure of the moderator to the ^{22}Na source. The first five RPA cycles in Figure 60 suggest a gradual decrease in peak signal, but the last half cycle falls in well with the early data. The compiled data in Figure 61 show the sharpest transition between On and Off states observed in this study ($\Delta V_{10\text{-}90} = 2.4$ V), as well as the lowest mid-point blocking potential (38.8 V).

So far, we have presented the CEM signals from experiments performed in Fall 2010 using the large Annihilation chamber, as depicted in Figure 33. We have assigned the difference between the CEM signals with the RPA On and Off to slow positrons, without any independent verification. We did record γ–γ coincidence data with the two NaI(Tl) detectors that show a statistically significant (but hardly convincing) correlation with the CEM signals. In Fall 2011, we replaced the large Annihilation chamber with a 2-3/4-inch Conflat cross, as depicted in Figure 34. This reduced the center-to-center separation between the NaI(Tl) detectors from 32.3 cm to 10.2 cm. We expected, and obtained, a corresponding increase in the γ–γ coincidence signal of $(32.3/10.2)^2 = 10$x. Figure 62 shows the new, improved γ–γ coincidence signal obtained from a 24.6-μm-thick Ne moderator. The ≈ 0.3 cps RPA Off baseline in the γ–γ coincidence signal is due to gamma radiation from the ^{22}Na source in Active mode. The strong correlation between the RPA modulation of the CEM and γ–γ coincidence signals demonstrates that the CEM On-Off signal is due to slow positrons arriving in the Annihilation chamber.

3.C.2. Solid Ar

We also investigated positron moderation in other Rg solids besides Ne. Figure 63 shows CEM data obtained before, during, and after annealing of an as-deposited 13.9-μm-thick Ar

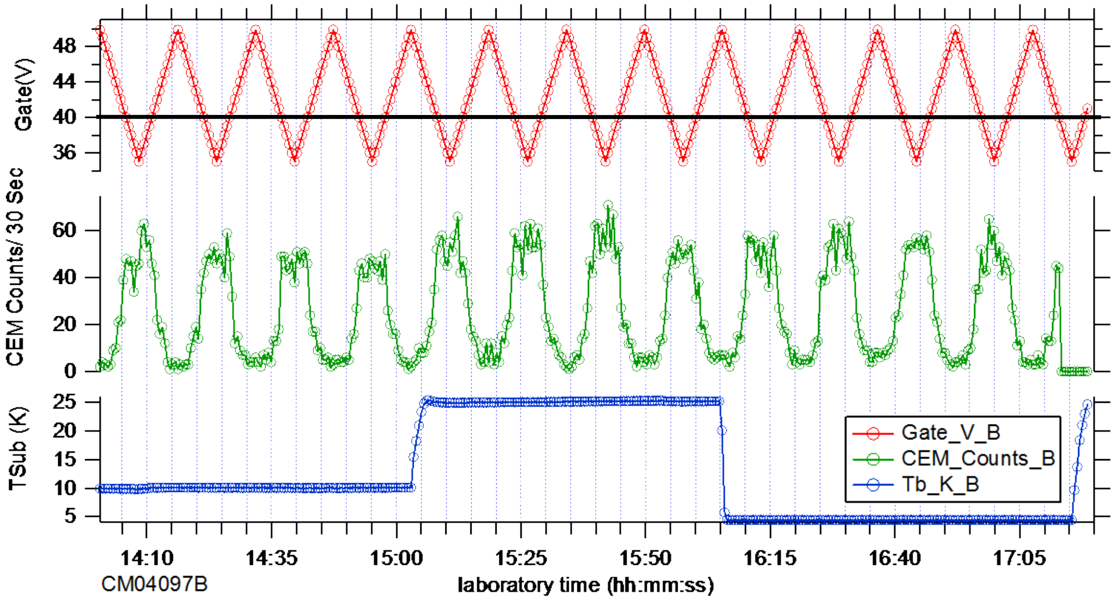

Figure 63. 13.9-μm-thick Ar moderator deposited through cold o/p-converter T_{sub} = 10 K, $T_{o/p}$ = 184 K, 0.81 mmol Ar (13:40 to 13:55) [CM04097B]

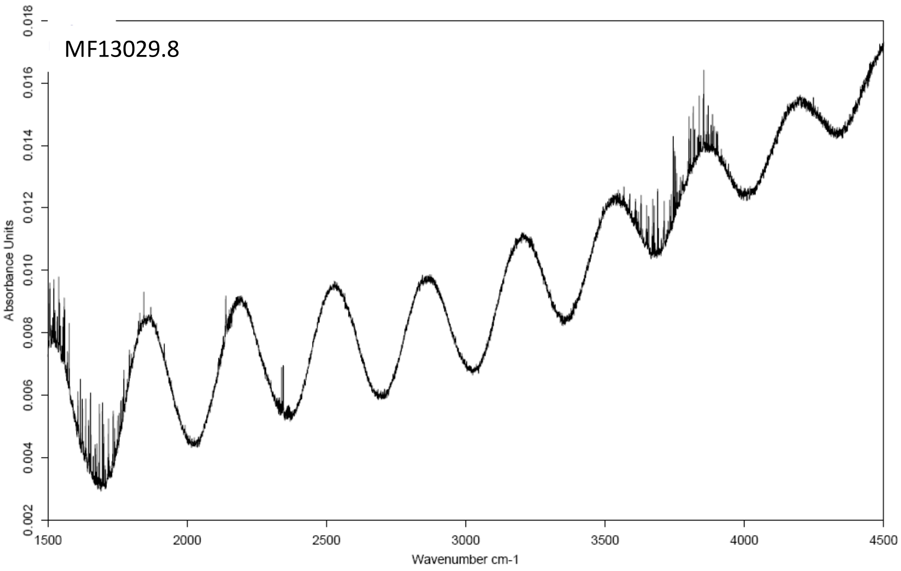

Figure 64. IR absorbance spectrum of sample depicted in Figure 63 [MF13029.8]

moderator. The CEM signal appears to grow upon warming to T ≈ 25 K, and remains slightly higher than the as-deposited T = 10 K signal upon cooling to T = 4.4 K.

Figure 64 shows clear interference fringes, which are more pronounced than for solid Ne since the larger index of refraction of Ar results in a stronger Fresnel reflection at the Ar-vacuum surface. The spectrum also shows features from trapped CO, CO_2, and H_2O molecules which made it through the much warmer o/p converter ($T_{o/p}$ = 184 K) than used for Ne depositions.

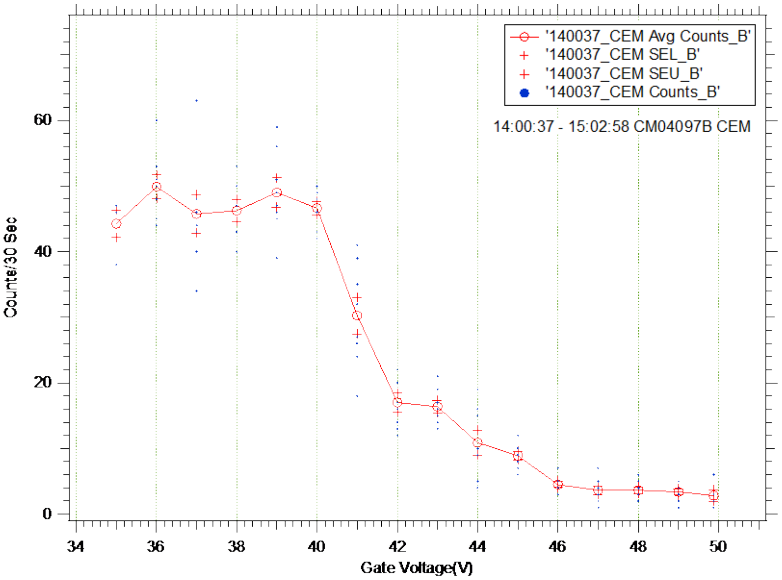

Figure 65. Compiled RPA scans for as-deposited sample depicted in Figure 63 CM04097B]
<On> = 1.6 cps, <Off> = 0.1 cps, 50% @ 41.3 V, $\Delta V_{10\text{-}90}$ = 5.0 V

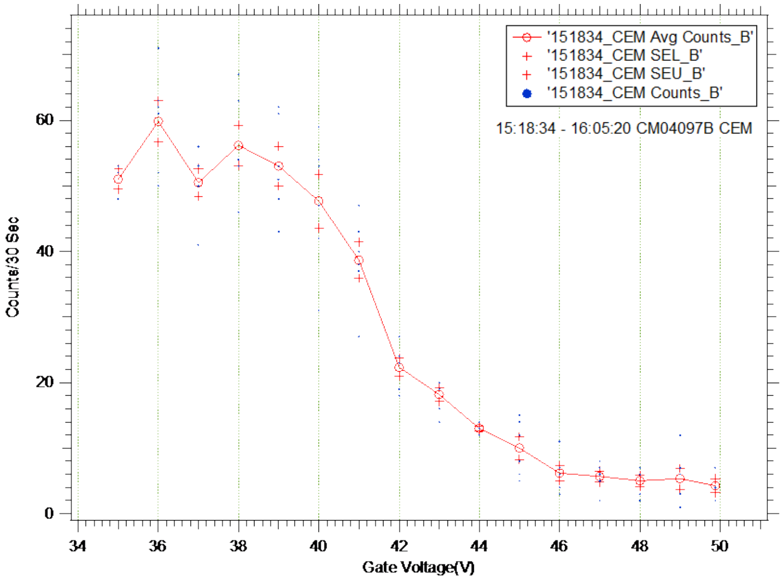

Figure 66. Compiled RPA scans during annealing of sample in Figure 63 [CM04097B] <On> = 1.8 cps, <Off> = 0.1 cps, 50% @ 41.5 V, $\Delta V_{10\text{-}90}$ = 5.4 V

Figures 65, 66, and 67 show the compiled RPA scans for the three phases of the experiment in Figure 63. The annealing process seems to shift the midpoint of the On-Off transition to higher retarding potentials, while leaving the width of the transition at ≈ 5 V.

We performed a series of experiments depositing Ar moderators at progressively higher deposition substrate temperatures. Figure 68 shows the T ≈ 15 K deposition and subsequent T ≈ 25 K annealing of a 13.4-µm-thick Ar moderator. Figure 69 shows the T ≈ 20 K deposition of a

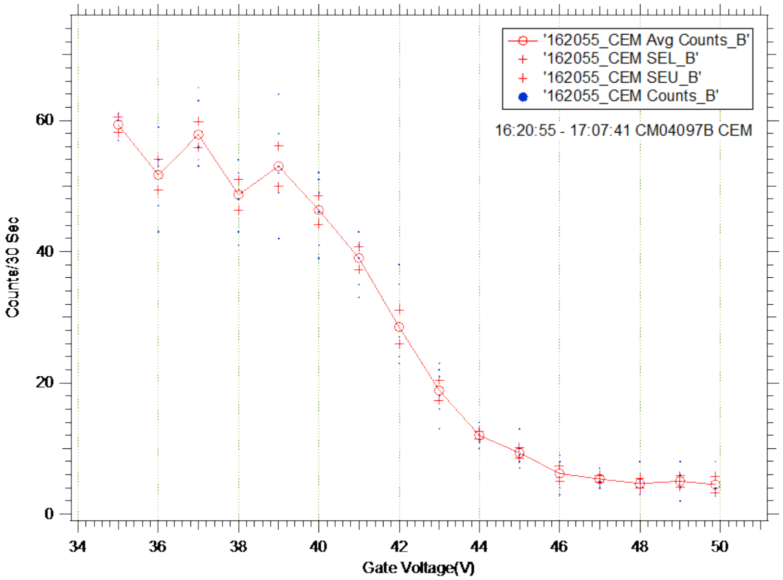

Figure 67. Compiled RPA scans for annealed sample depicted in Figure 63 [CM04097B] <On> = 1.8 cps, <Off> = 0.1 cps, 50% @ 41.9 V, $\Delta V_{10\text{-}90}$ = 5.3 V

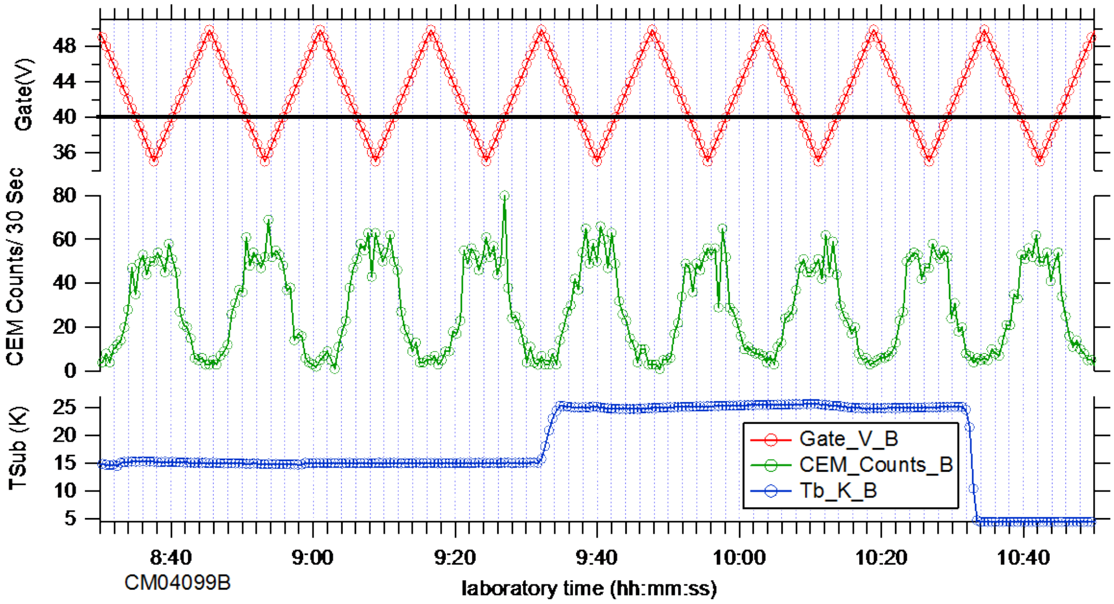

Figure 68. 13.4-µm-thick Ar moderator deposited through cold o/p-converter T_{sub} = 15 K, $T_{o/p}$ = 161 K, 0.84 mmol Ar (08:08 to 08:30). [CM04099B]

13.9-µm-thick Ar moderator. Figure 70 shows the T ≈ 24 K deposition of a 15.5-µm-thick Ar moderator. For Ar, it seems like higher deposition substrate temperatures in the 10-24 K range yield higher positron moderation efficiencies.

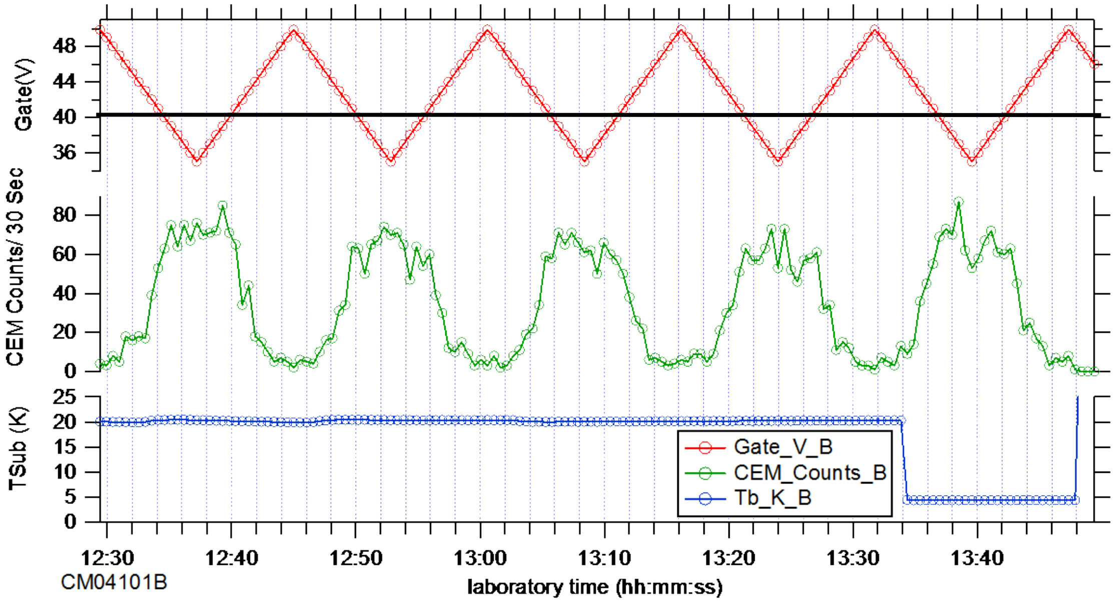

Figure 69. 13.9-µm-thick Ar moderator deposited through cold o/p-converter T_{sub} = 20 K, $T_{o/p}$ = 175 K, 0.85 mmol Ar (12:10 to 12:30). [CM04101B]

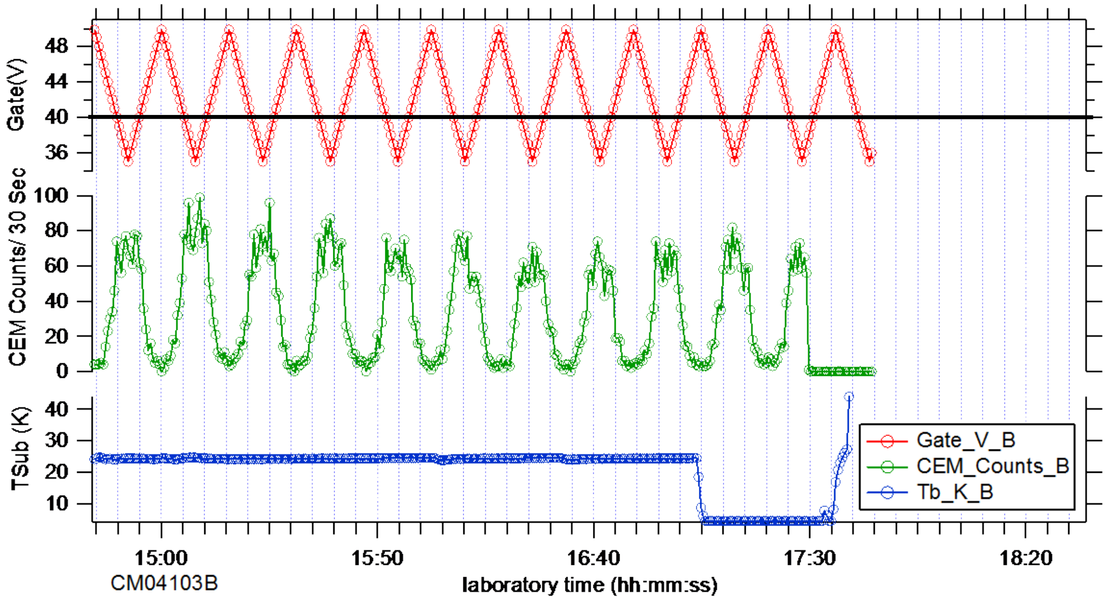

Figure 70. 15.5-µm-thick Ar moderator deposited through cold o/p-converter T_{sub} = 24 K, $T_{o/p}$ = 205 K, 0.96 mmol Ar (14:24 to 14:44) [CM04103B]

Figure 71 shows the compiled RPA scans for the Ar moderator as-deposited at T = 24 K. It most closely resembles the data for the annealed moderator shown in Figure 67.

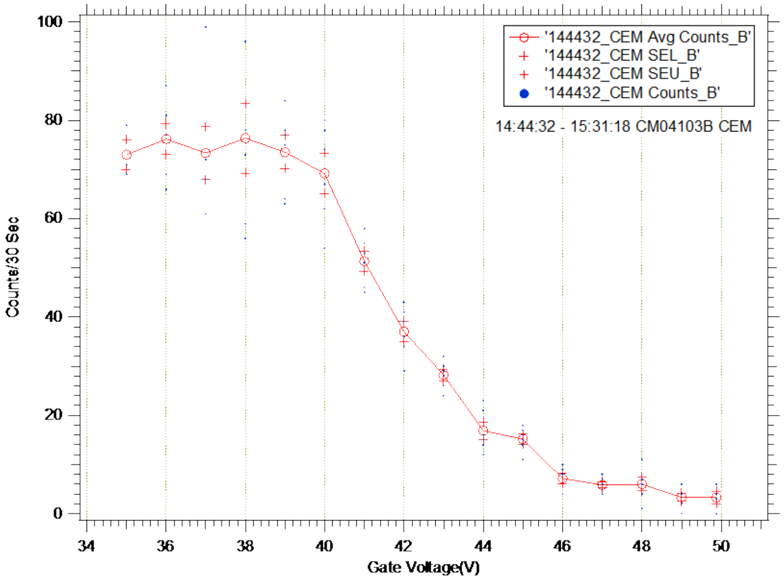

Figure 71. Compiled RPA scans for as-deposited sample depicted in Figure 70 [CM04103B] <On> = 2.5 cps, <Off> = 0.2 cps, 50% @ 41.8 V, $\Delta V_{10\text{-}90}$ = 4.9 V

3.C.3. Solid Kr

Besides Ne, we performed the majority of our experiments with Kr moderators. Figure 72 shows results from a relatively thin Kr moderator deposited at T = 25 K from Kr gas evaporated by warming the previously filled, cold o/p converter from $T_{o/p}$ = 98 → 115 K. Figure 73 shows strong interference fringes and only weak trapped CO_2 and H_2O absorptions.

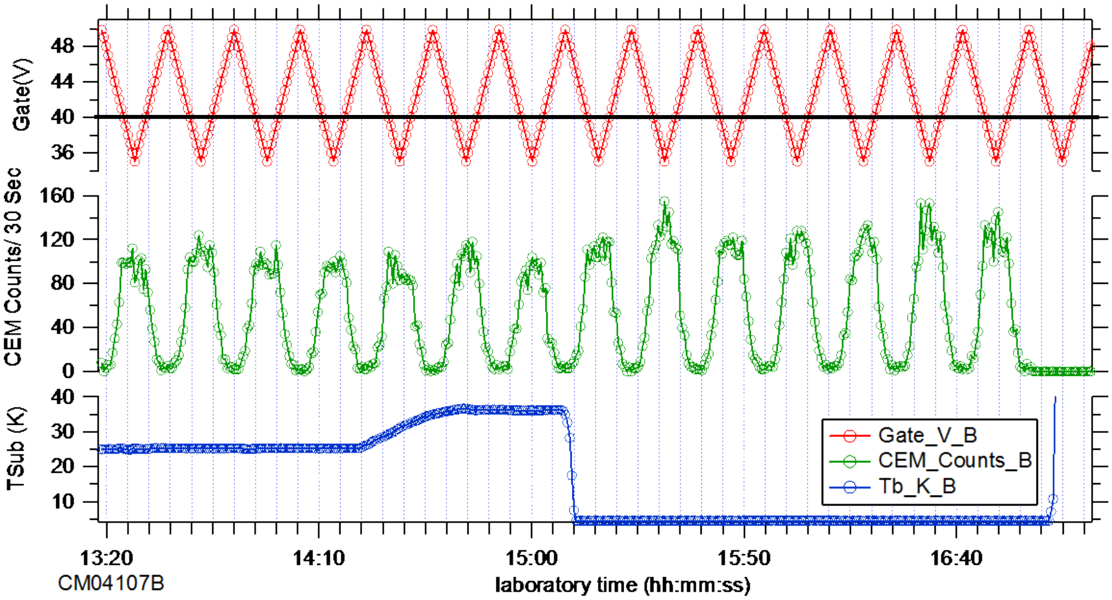

Figure 72. 7.0-µm-thick Kr moderator deposited by evaporation from cold o/p converter T_{sub} = 25 K, $T_{o/p}$ = 98 → 115 K (12:45 to 13:20). [CM04107B]

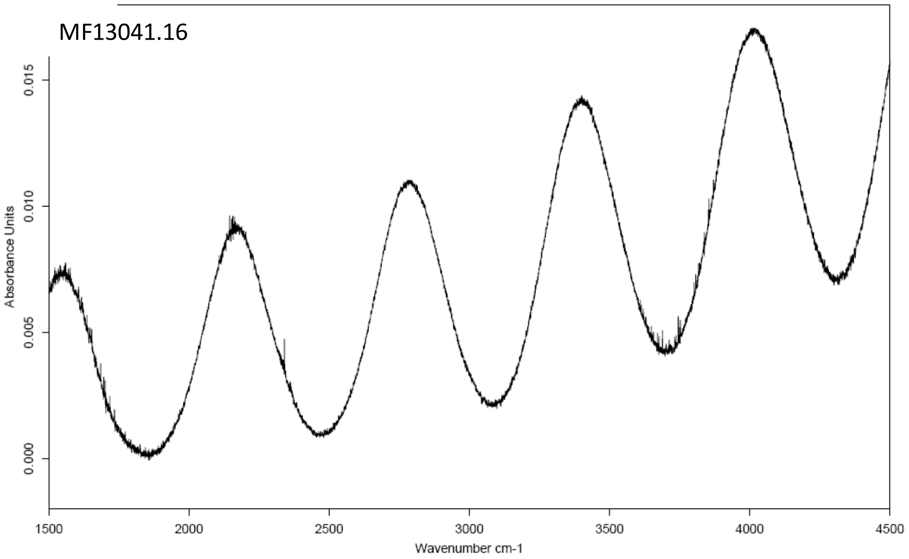

Figure 73. IR absorbance spectrum of sample depicted in Figure 72 [MF13041.16]

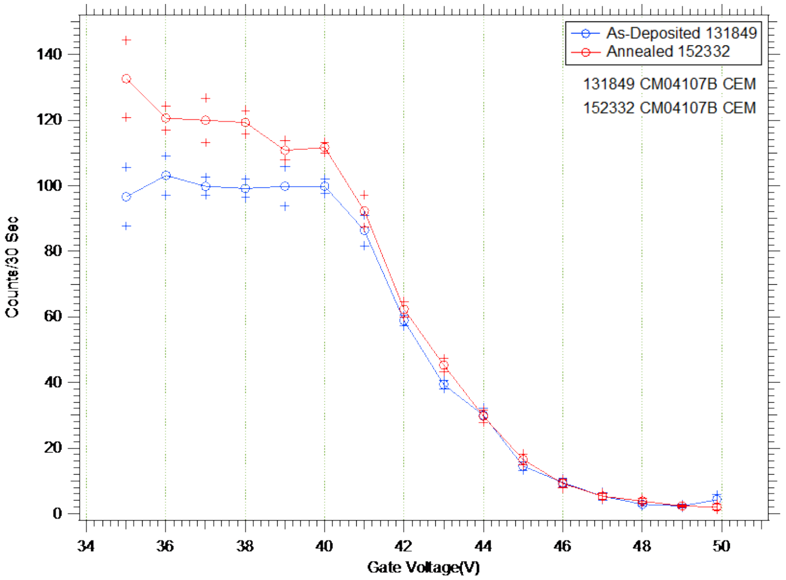

Figure 74. Compiled RPA scans for data shown in Figure 72 [CM04107B]
as-deposited: <On> = 3.3 cps, <Off> = 0.3 cps, 50% @ 42.0 V, $\Delta V_{10\text{-}90}$ = 5.3 V
annealed: <On> = 4.0 cps, <Off> = 0.3 cps, 50% @ 41.8 V, $\Delta V_{10\text{-}90}$ = 4.5 V

Figure 74 shows the compiled RPA scans for both the as-deposited and post-annealing sample; annealing to T ≈ 36 K results in a noticeable increase in the moderation efficiency.

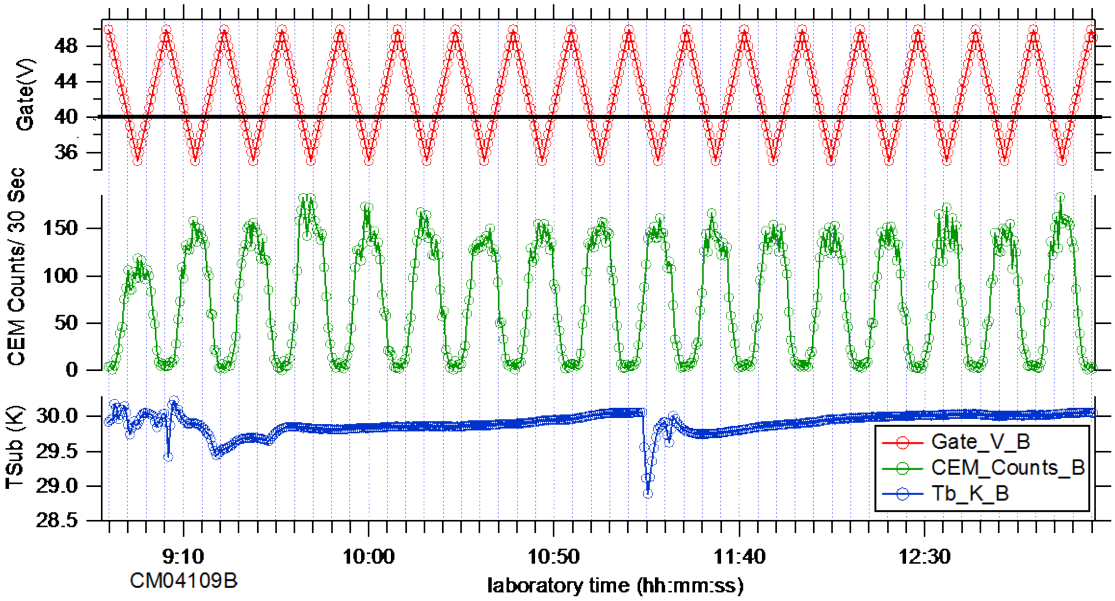

Figure 75. 31.6-µm-thick Kr moderator as-deposited through cold o/p-converter
T_{sub} = 30 K, $T_{o/p}$ = 119 → 124 K, 1.54 mmol Kr (08:30 to 09:15) [CM04109B]

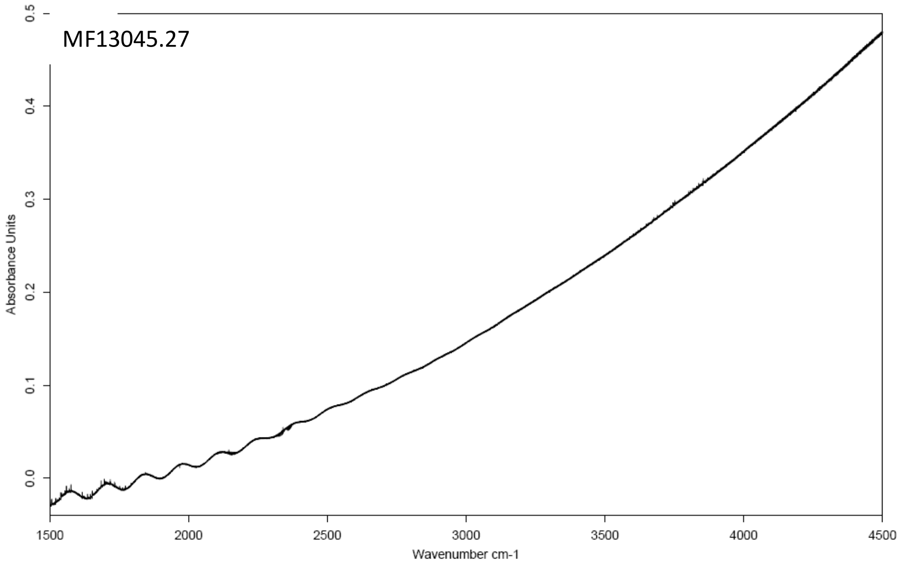

Figure 76. IR absorbance spectrum of sample depicted in Figure 75 [MF13045.27]

Figure 75 shows results from a much thicker Kr moderator deposited at T = 30 K through the cold o/p converter. The CEM signal from this as-deposited moderator exceeds that of the annealed thin sample depicted in Figure 72. Figure 76 shows remnant transmission interference fringes, and the strong wavelength-dependent scattering familiar to practitioners of Matrix Isolation Spectroscopy in the heavier Rg hosts. The compiled RPA scans in Figure 77 seem to indicate a shift of the midpoint to higher blocking potential relative to the thinner Kr moderator, however this shift is well within the error of our graphical estimation procedure. It would also be opposite the thickness-dependent trend observed for Ne moderators.

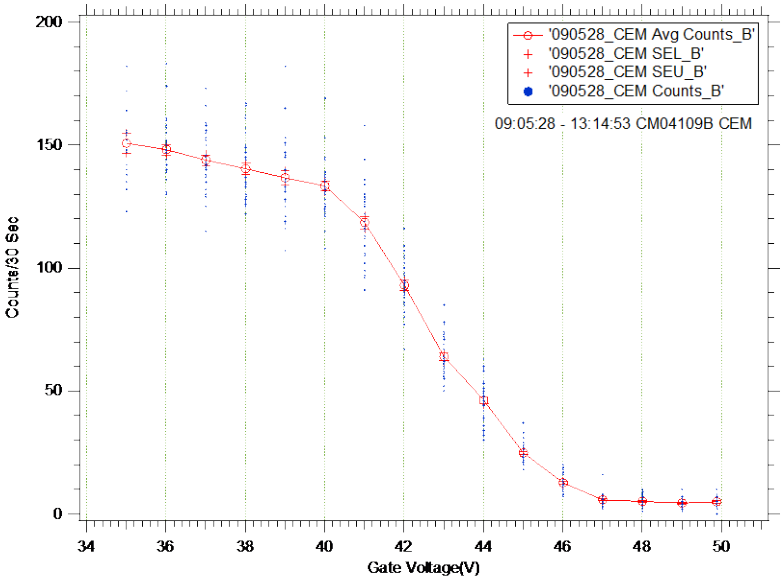

Figure 77. Compiled RPA scans from data shown in Figure 75 [CM04109B]
<On> = 4.7 cps, <Off> = 0.2 cps, 50% @ 42.6 V, $\Delta V_{10\text{-}90}$ = 5.0 V

3.C.4. Solid Xe

Figure 78 shows results from a Xe moderator deposited at T ≈ 50 K from the dopant manifold, however in ≈ 40 μmol aliquots delivered over roughly an hour long period. By the end of the experiment, the CEM signal in the RPA On state is only ≈ 0.7 cps, and any modulation of the γ–γ coincidence signal is not visible against its ≈ 0.3-0.4 cps background.

Figure 79 shows the strongly contrasting, but slowly modulated, interference fringes for the very thin (0.77 μm) Xe sample recorded after deposition of the first 42 μmol of Xe.

Figure 80 shows the compiled RPA scans from data recorded for the as-deposited sample immediately following those shown in Figure 78. The CEM signal appears to have dropped off to about 0.6 cps by the time those scans were acquired. The low count rate required a long counting interval (100 s), and a correspondingly low retarding potential resolution (2 V) to complete the data acquisition in the allotted time.

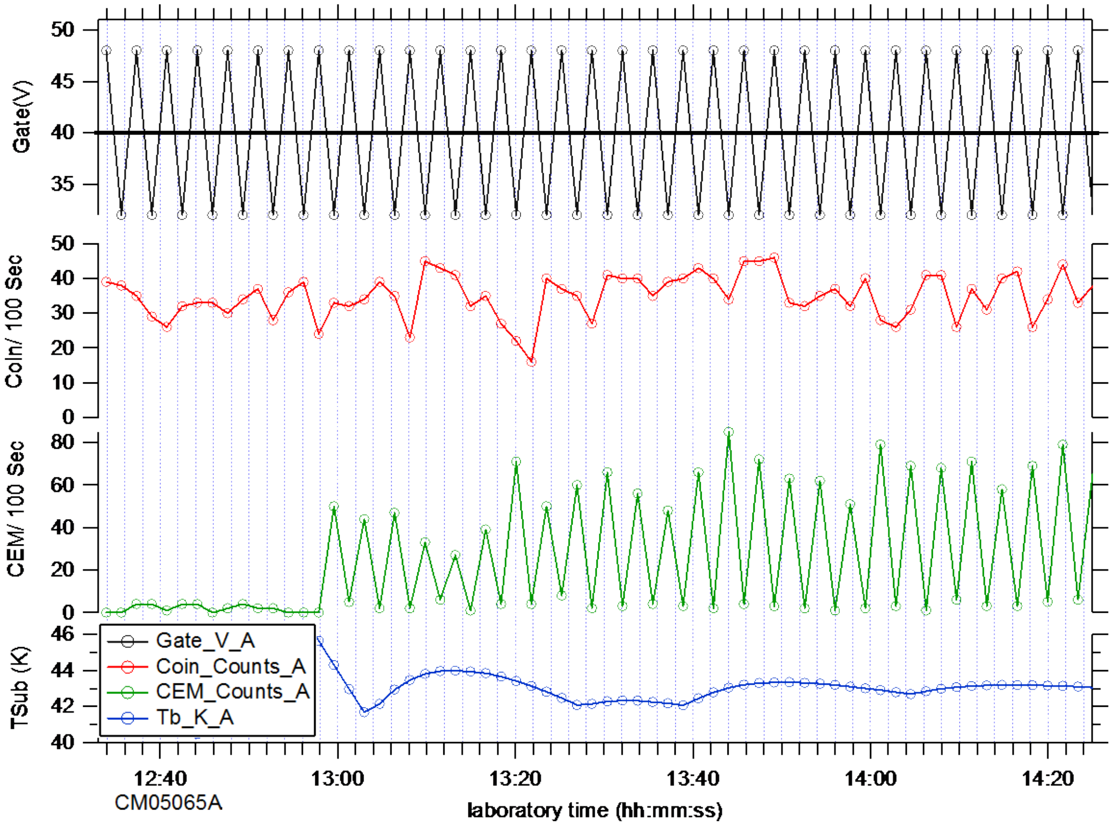

Figure 78. 6.9-μm-thick Xe moderator deposited from dopant manifold T_{sub} = 50 → 46 K, $T_{o/p}$ = 6.4 K, 416 μmol Xe (12:53 to 13:59) [CM05065A]

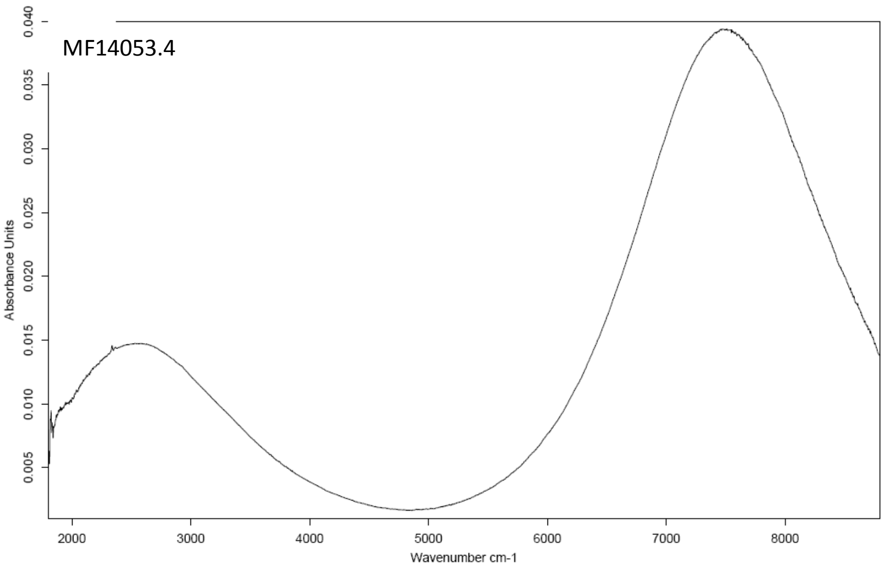

Figure 79. IR absorbance spectrum of sample depicted at 12:57 in Figure 78 [MF14053.4]

Figure 81 shows data from a thicker Xe moderator deposited at T = 48 K from the dopant manifold. The CEM signal level is only slightly higher than for the thinner moderator depicted in Figure 78. Figure 82 shows interference fringes and weak impurity absorptions. Due to the low signal levels and low voltage resolution, it is difficult to make a conclusive comparison of the compiled RPA scan data in Figures 80 and 83, however the thicker moderator seems to show a slightly broader On -Off transition.

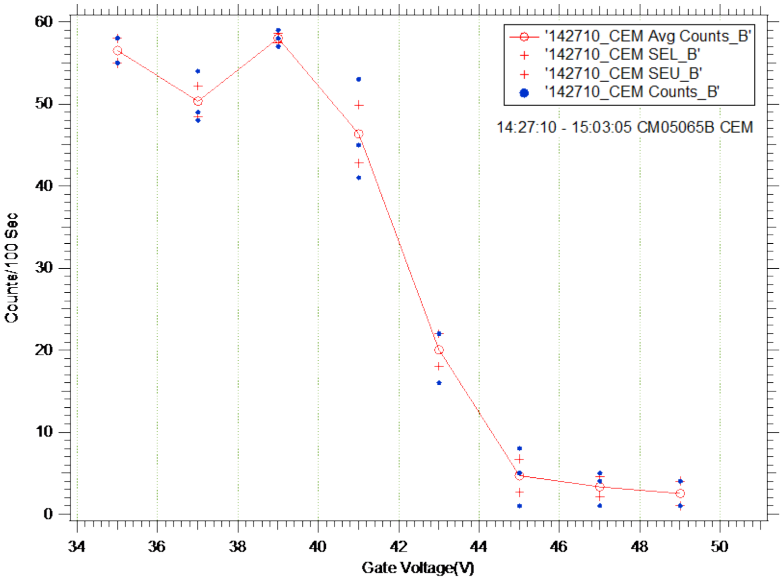

Figure 80. Compiled RPA scans for as-deposited sample depicted in Figure 78 [CM05065A] <On> = 0.54 cps, <Off> = 0.05 cps, 50% @ 42.3 V, ΔV_{10-90} = 4.1 V

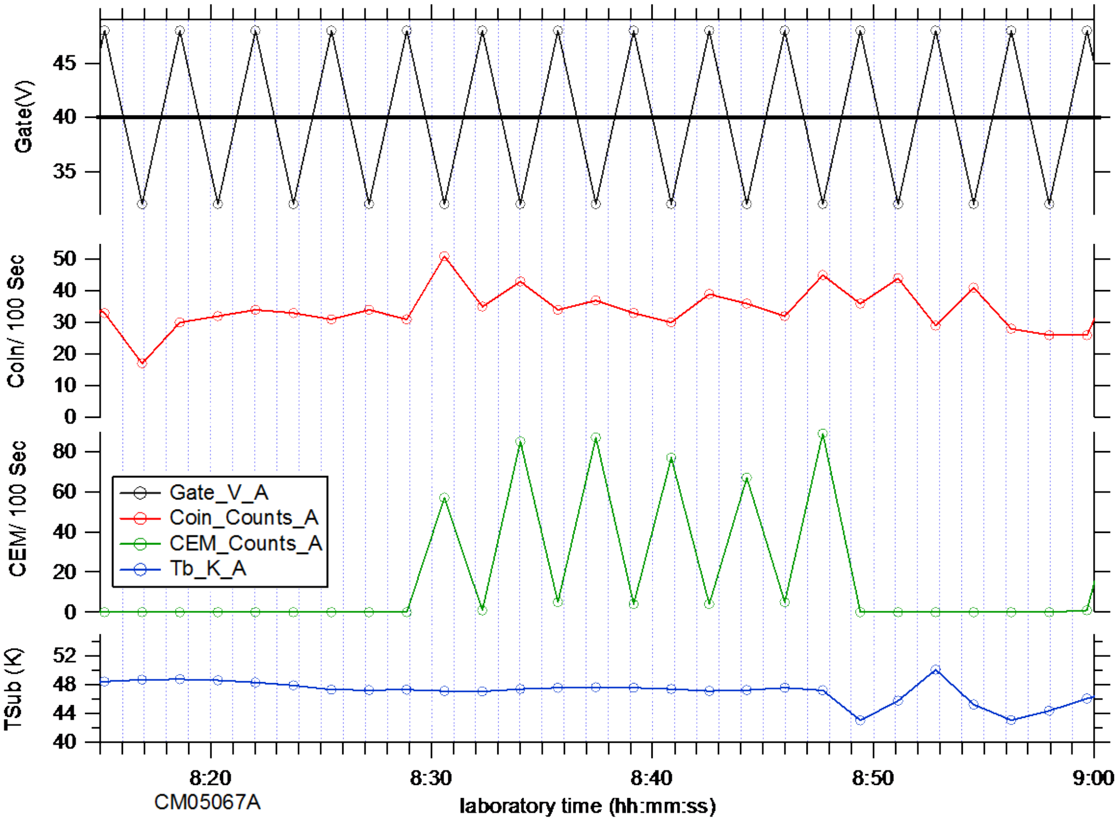

Figure 81. 13.4-µm-thick Xe moderator deposited from dopant manifold T_{sub} = 48 K, $T_{o/p}$ = 302 K, 94 µmol Xe (08:15 to 08:29) [CM05067A]

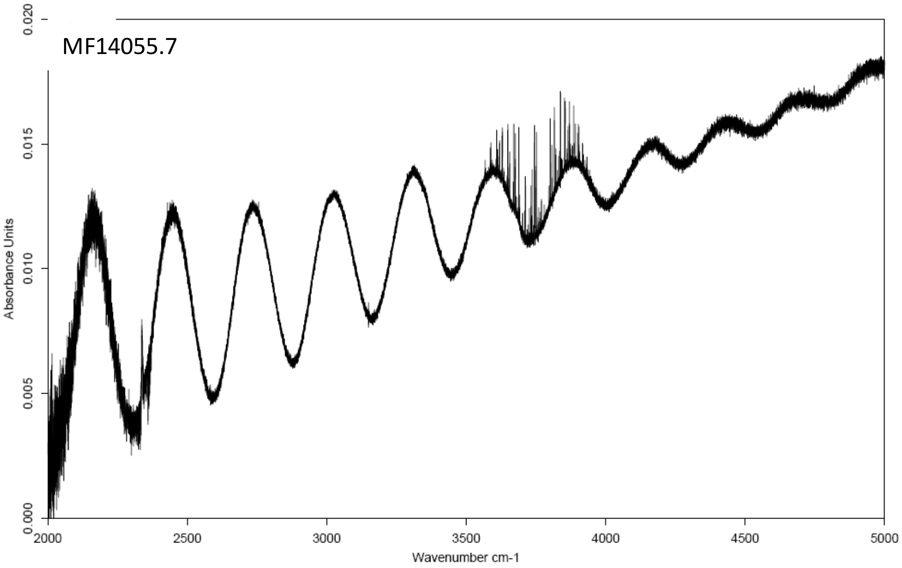

Figure 82. IR absorbance spectrum of sample depicted in Figure 81 [MF14055.7]

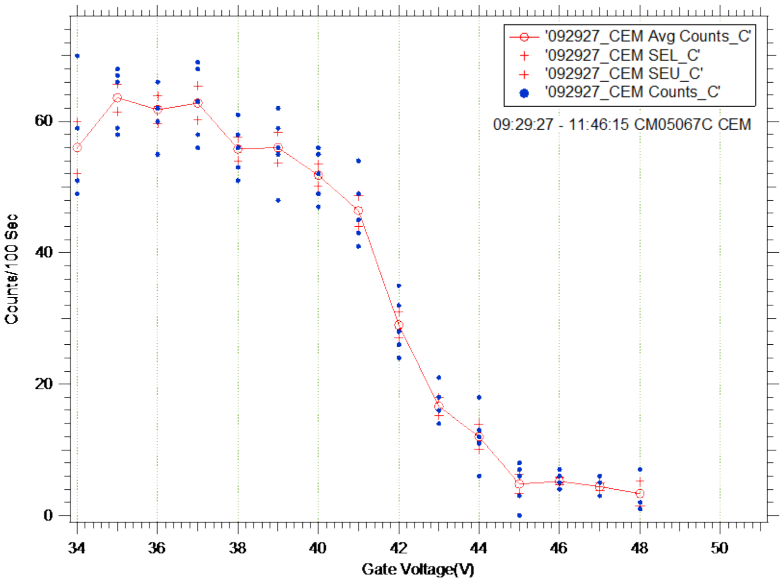

Figure 83. Compiled RPA scans for as-deposited sample depicted in Figure 81 [CM05067A] <On> = 0.60 cps, <Off> = 0.06 cps, 50% @ 41.8 V, $\Delta V_{10\text{-}90}$ = 4.9 V

3.C.5. Solid N_2

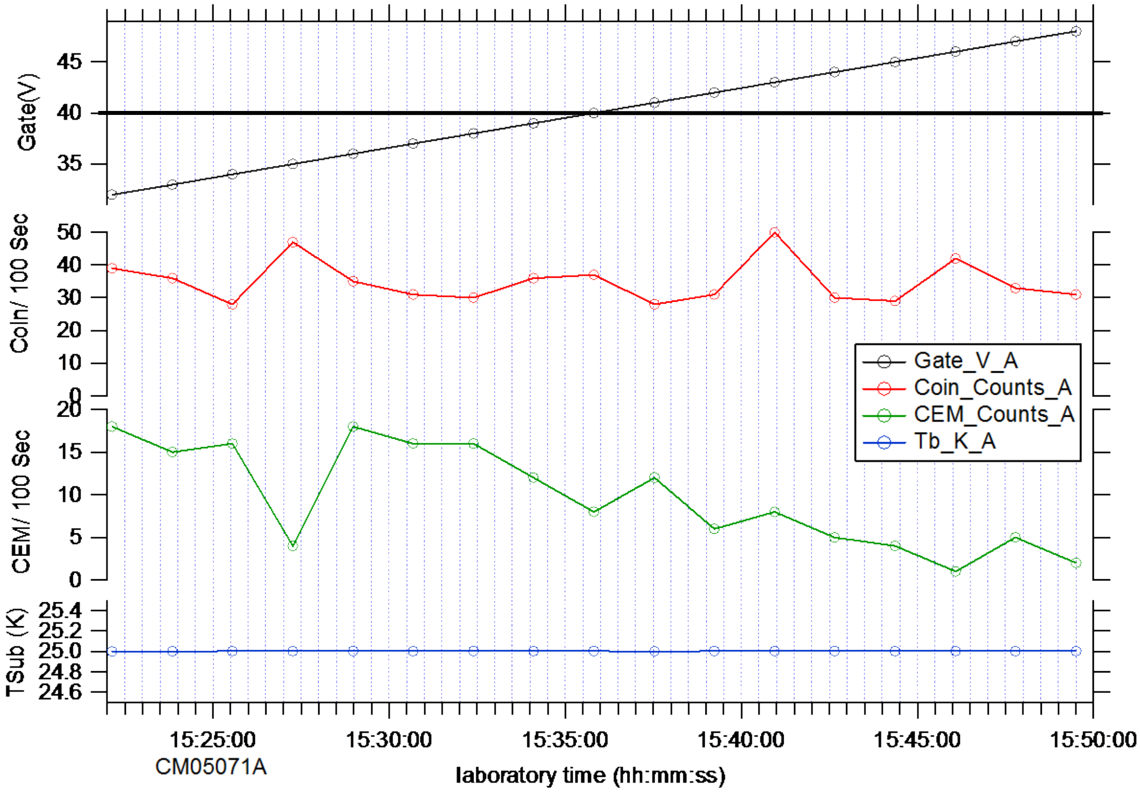

Figure 84. 5.7-μm-thick N_2 moderator deposited from dopant manifold T_{sub} = 25 K, $T_{o/p}$ = 302 K, 46 μmol N_2 (15:16 to 15:20) [CM05071A]

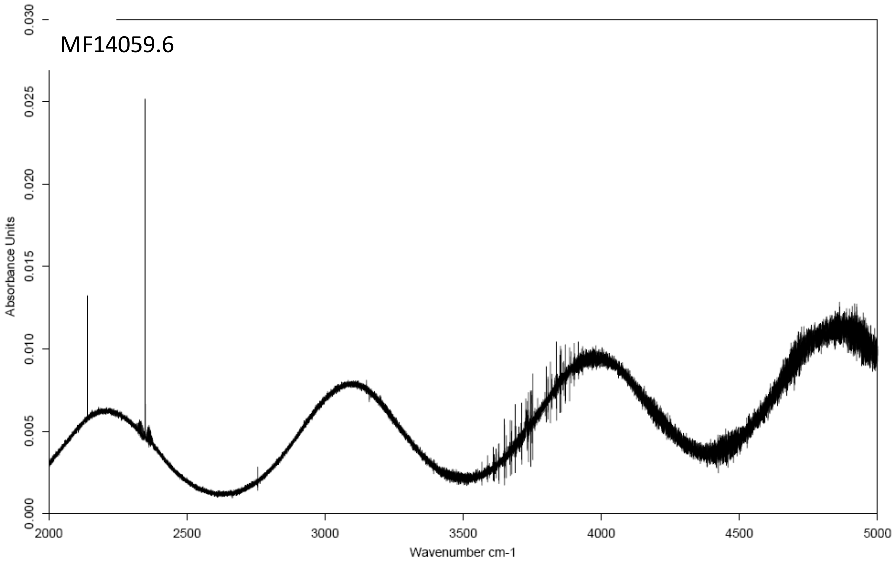

Figure 85. IR absorbance spectrum of sample depicted in Figure 84 [MF14059.6]

Figure 84 depicts the last positron moderation experiment performed during this project: a half-cycle RPA scan of an N_2 moderator. The $\approx$ 0.15 cps CEM signal is clearly visible above the $\approx$ 0.03 cps background. The very sharp absorption lines for trapped CO and CO_2 molecules shown in Figure 85 at 2139.7 and 2348.8 cm^{-1} (respectively) have integrated intensities of 0.0010 and 0.0032 cm^{-1}, corresponding to concentrations of roughly 3 and 1 ppm [65]. The weak, broad solid α-N_2 absorption peaking near 2370 cm^{-1} [80] is obscured by the transmission fringes.

3.C.6. Solid Molecular Hydrogens

Over the course of this project, we performed seven solid pH_2 and two solid oD_2 positron moderation experiments, without any hint of a statistically significant slow positron signal. The numerous accompanying H_2 and D_2 slow positron attenuation experiments are described separately, below.

Figure 86 shows the null result for a 310-μm-thick pH_2 “moderator” deposited through the cold o/p converter. Approximately half of the pH_2 was deposited before the start of the scan showed in Figure 86, the other half was deposited between 09:44 and 10:10, producing the observed increase in the substrate temperature.

Figure 87 shows the IR absorption spectrum of this sample; the inset shows the oH_2 induced absorption at 4153 cm^{-1}. The integrated absorption of this feature is 0.0021 cm^{-1}, which combined with the 790 μm optical path length indicates a residual oH_2 concentration of 760 ppm [64]. This concentration is two orders of magnitude higher than the 6 ppm expected from the $T_{o/p}$ = 12.0 K temperature of the o/p converter. We eventually discovered that the hot filament ionization gauge used to measure the pressure during moderator depositions was causing back-conversion of the pH_2 gas. Once we turned off this gauge, the residual oH_2 concentrations in our pH_2 solids returned to their customary sub-100 ppm levels.

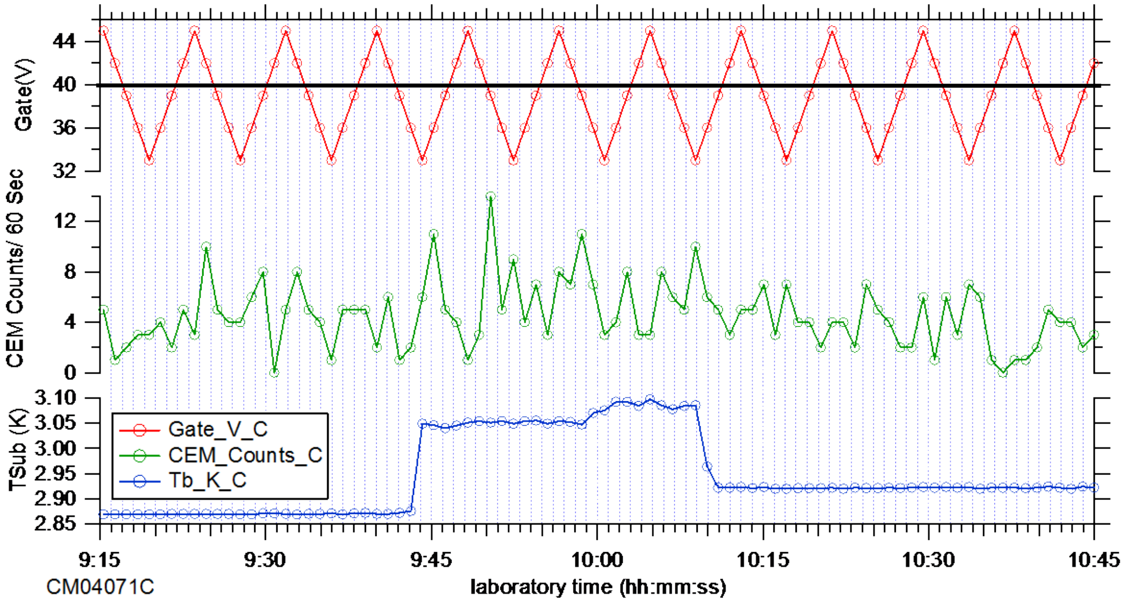

Figure 86. 310-µm-thick pH_2 "moderator" deposited through cold o/p converter T_{sub} = 2.9 K, $T_{o/p}$ = 12.0 K, 30.3 mmol pH_2 (08:50 to 09:05 and 09:44 to 10:10) [CM04071C]

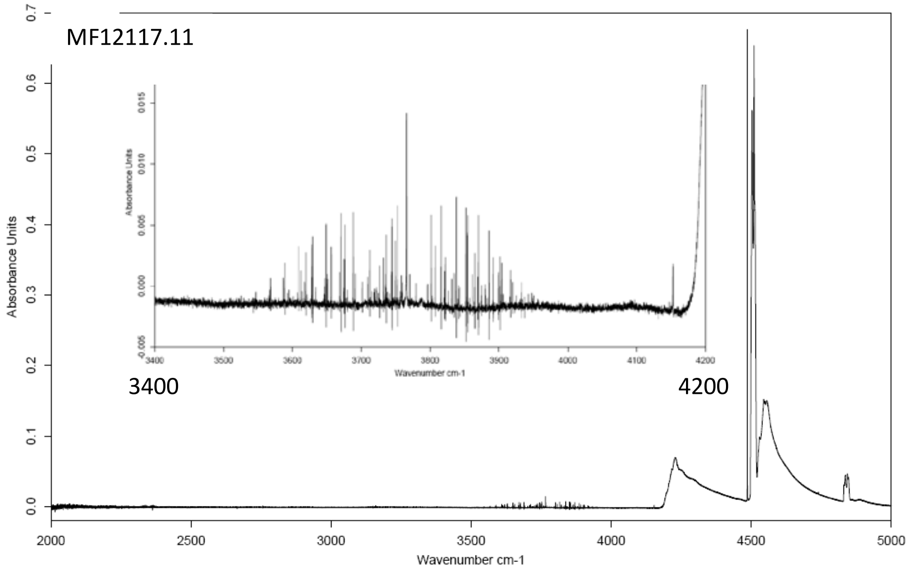

Figure 87. IR absorbance spectrum of sample depicted in Figure 86 [MF12117.11]

3.D. Positron Attenuation Experiments on Overcoated Rg Moderators

3.D.1. Solid molecular hydrogens on solid Ne

Our great disappointment in our failure to detect any slow positrons from our highly touted RVD pH_2 solids motivated a series of experiments to help us understand this unexpected result. We quickly discovered that not only does pH_2 not moderate positrons, it also kills the flux of slow positrons from Rg moderators. Figure 88 shows results from such an experiment, where a mere 1.3-µm-thick overcoated layer of solid pH_2 completely obliterates the slow positron signal from a working 13.5-µm-thick Ne moderator! This pH_2 was deposited between 16:10 and 16:13 by raising the temperature of the "full" cold o/p converter from $T_{o/p} = 6.4 \rightarrow 11.7$ K. A few minutes later, the deposition of an additional 0.35 mmol (≈ 2 µm) of Ne restores the slow positron signal.

Figure 89 shows the pH_2 "Q+S" region of the IR absorption spectrum. Using the values in Tables 3 and 4 we calculate a 3.3 µm optical path length, and a 1.3 µm thickness, for this pH_2 solid. This sample was deposited with the Ne flowing from the dopant manifold, and the H_2 through the cold o/p converter. This results in a fairly dirty Ne moderator, and in poor control of the H_2 deposition rate.

Figure 90 shows results for an experiment with the Ne gas is deposited through the o/p converter (albeit at $T_{o/p} = 297$ K) and nH_2 gas deposited from the dopant manifold. These CEM signal levels are not directly comparable to those in Figure 88 due to long term changes in instrumental sensitivity, caused mainly by inadvertent exposure of the high voltage biased CEM detector to "puffs" of gases during moderator evaporation. Figure 91 shows a Ne moderator grown through the cold o/p converter on the same day as the sample depicted in Figure 90.

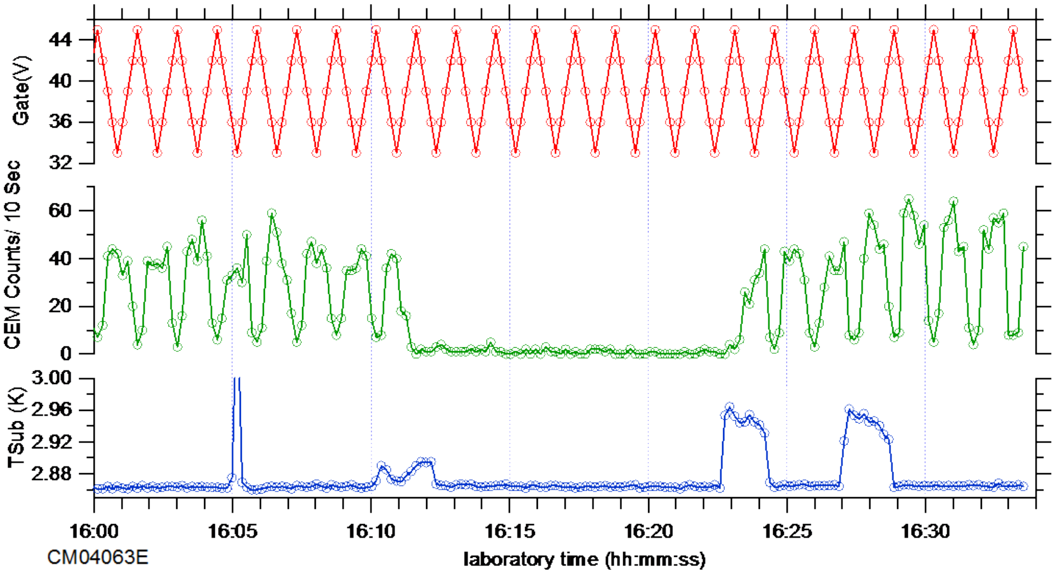

**Figure 88. Ne/pH_2/Ne moderator/attenuator/moderator [CM04063E]
13.5-µm-thick Ne moderator (2.08 mmol, 14:49 to 15:39)
+ 1.3-µm-thick pH_2 (16:10 to 16:13) + 0.35 mmol Ne (16:22 to 16:29)**

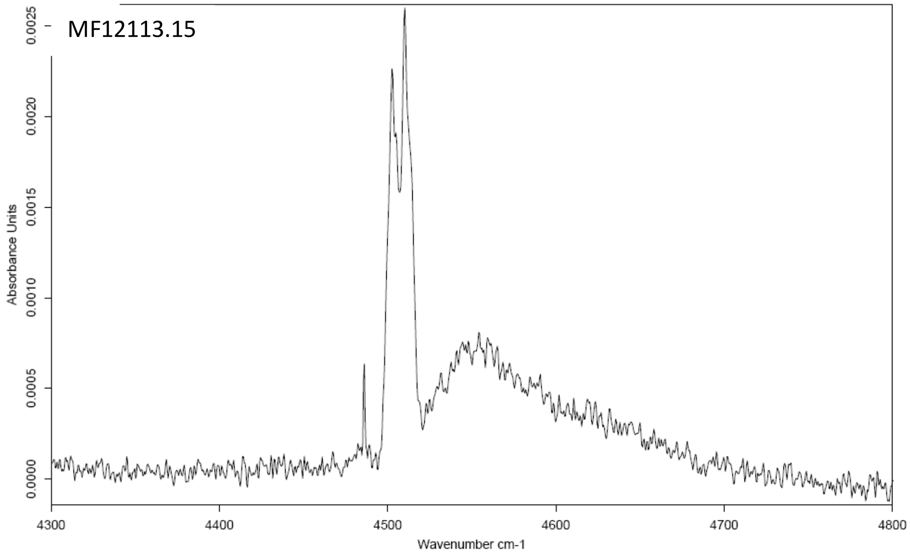

Figure 89. IR absorbance spectrum of sample depicted in Figure 88 [MF12113.15]

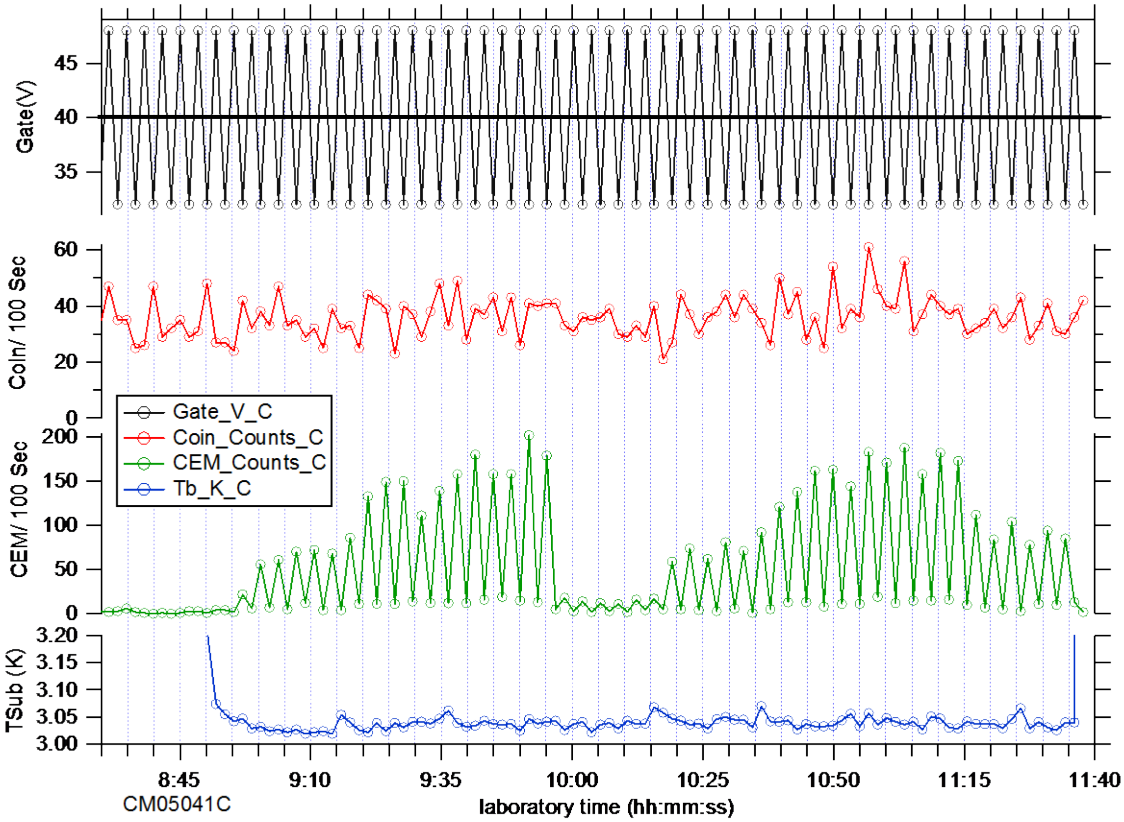

Figure 90. Ne/nH$_2$/Ne/nH$_2$ moderator/attenuator/moderator/attenuator [CM05041C] 4.1-μm-thick Ne moderator (0.53 mmol, 08:55 to 09:45) + 11.2 μmol nH$_2$ (09:55 to 09:56) + 0.39 mmol Ne (10:15 to 10:40) + 1.8 μmol nH$_2$ (11:15 to 11:16)

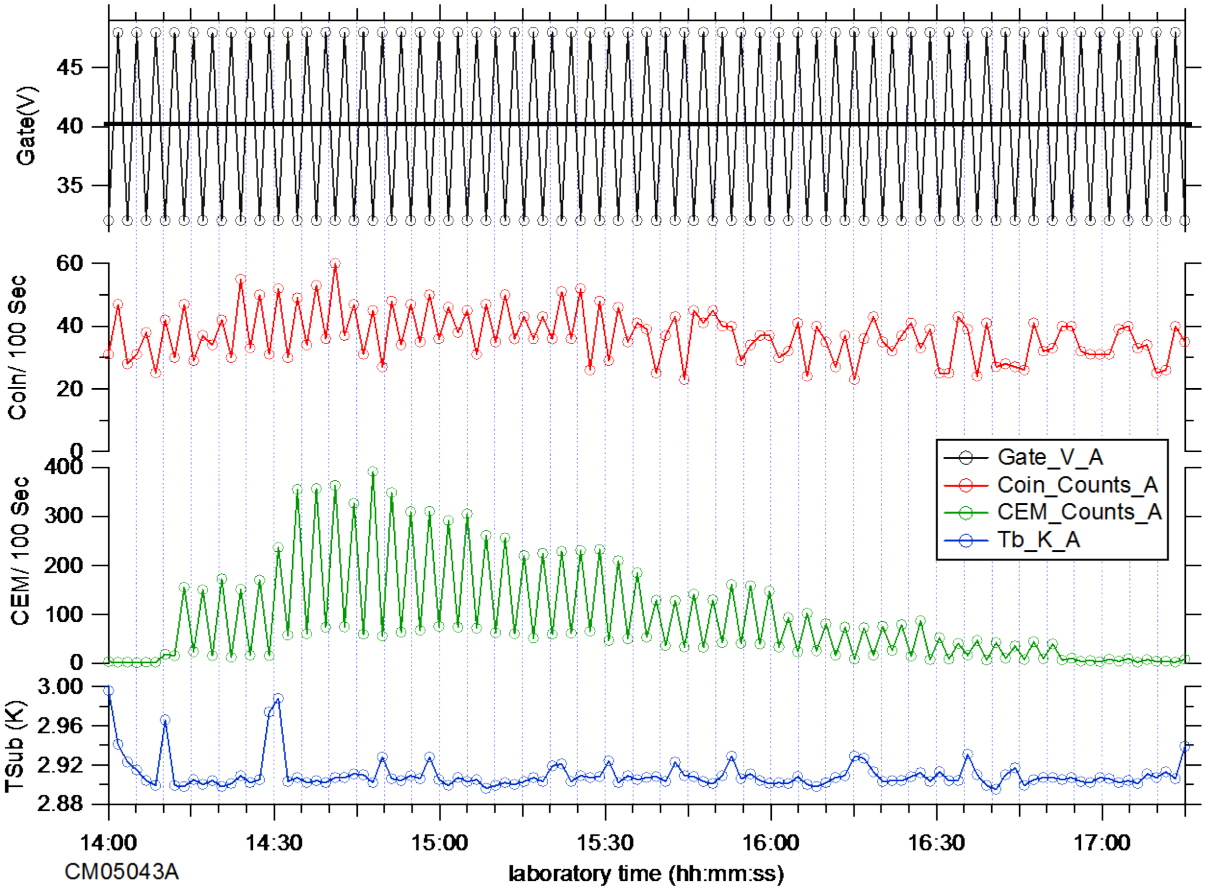

Figure 91. nH_2 attenuator grown on 7.8-µm-thick Ne moderator [CM05043A]
1.36 mmol Ne through $T_{o/p}$ = 27.0 K o/p converter + 35.3 µmol nH_2 deposited in six steps

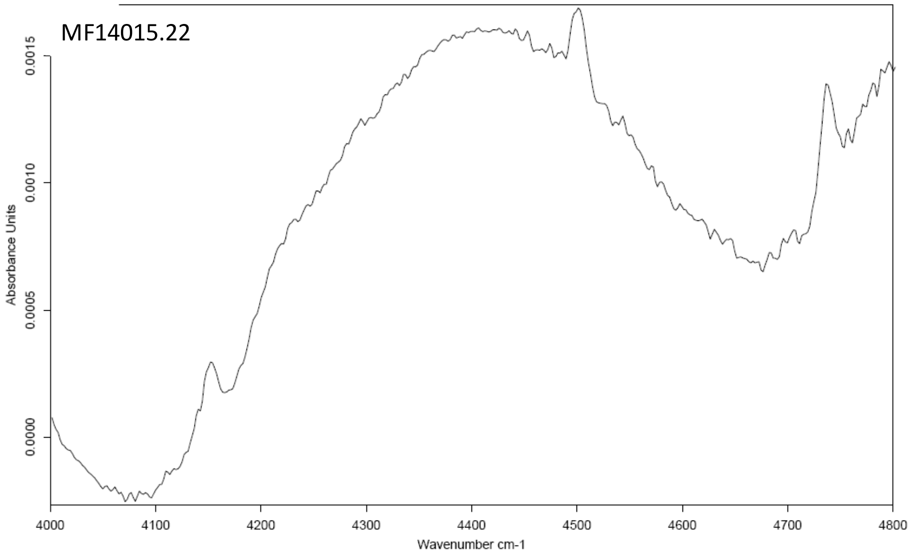

Figure 92. IR absorbance spectrum of sample depicted in Figure 91 [MF14015.22]

In this case the CEM signal levels are directly comparable, and the cleaner, thicker moderator in Figure 91 yields nearly double the flux of slow positrons.

The nH_2 overcoat layer in Figure 91 was deposited in six discrete steps, with time taken in between to record the surviving slow positron yield. Those results are presented in greater detail below in the Discussion section.

The intensity pattern of the weak absorption features seen in Figure 92 near 4152, 4502, and 4738 cm^{-1} match the known IR spectrum of solid nH_2 [81]. Comparing these features with those for a known path length nH_2 solid in Ref. [81], and applying the correction factor in Table 4, we can estimate a final solid nH_2 layer thickness of 0.62(±0.03) μm, where the uncertainty is the standard error of the mean. Assuming a constant rate of solid nH_2 thickness growth *vs.* amount of nH_2 deposited, we can go back to Figure 90 and estimate solid nH_2 overcoat layer thicknesses of ≈ 200 nm for the deposition ending at 09:56, and ≈ 30 nm at 11:16.

Figure 93 shows results from a similar experiment with a solid nD_2 overcoat layer built up by depositing the same amount of nD_2 onto a Ne moderator in six discrete steps. We acquired IR absorption data from thin nH_2 and nD_2 films showing interference fringes for the purpose of calibrating the intensities of the absorption features. However, we have not completed their analysis, yet, and so postpone a detailed discussion of the thickness of the attenuating layers.

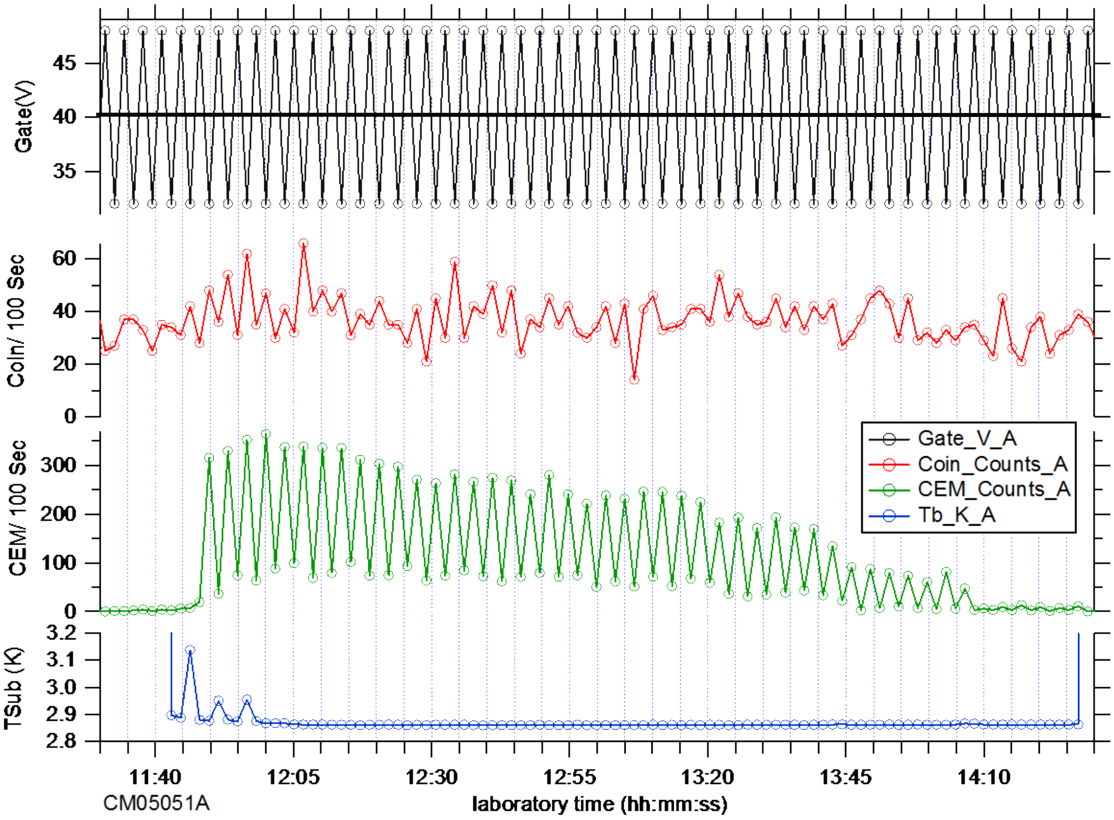

Figure 93. nD_2 attenuator grown on 10.5-μm-thick Ne moderator [CM05051A]
Ne evaporated from $T_{o/p}$ ≈ 25 K o/p converter + 35.4 μmol nD_2 deposited in six steps

3.D.2. Solid CO and solid H_2O on solid Ne

We also performed overcoated layer positron attenuation experiments with solid CO and H_2O ice films deposited on working Ne moderators. Figure 94 shows the results obtained by depositing 11.3 μmol of CO in five discrete steps. Clearly, the solid CO is more effective (on a molar basis) at reducing the flux of slow positrons than is either solid nH_2 or nD_2. The IR absorption spectrum of the final CO film (not shown) includes a strong absorption feature due to trapped CO_2, which is apparently present in our CO sample as an impurity at the ≈ 6 % level.

Figure 95 shows the results of overcoating a Ne moderator with an amorphous water ice film made by depositing 3.64 μmol of H_2O vapor in four discrete steps. Handling and metering H_2O in this manner poses special problems because water is "sticky," *i.e.*: a significant fraction of the water in our manifold is adsorbed on the interior surfaces [82]. Furthermore, the vapor pressure of water at room temperature is only ≈ 20 torr, so working pressures in this ballpark increase the fraction of adsorbed water and even risk the formation of condensed bulk water deposits in the manifold. We attempt to mitigate these effects by working at much lower H_2O pressures in our manifold, and by inducing only very small changes to this pressure during a deposition. For example, producing the sample depicted in Figure 95 involved a change in manifold pressure from 3.421 to 3.002 torr.

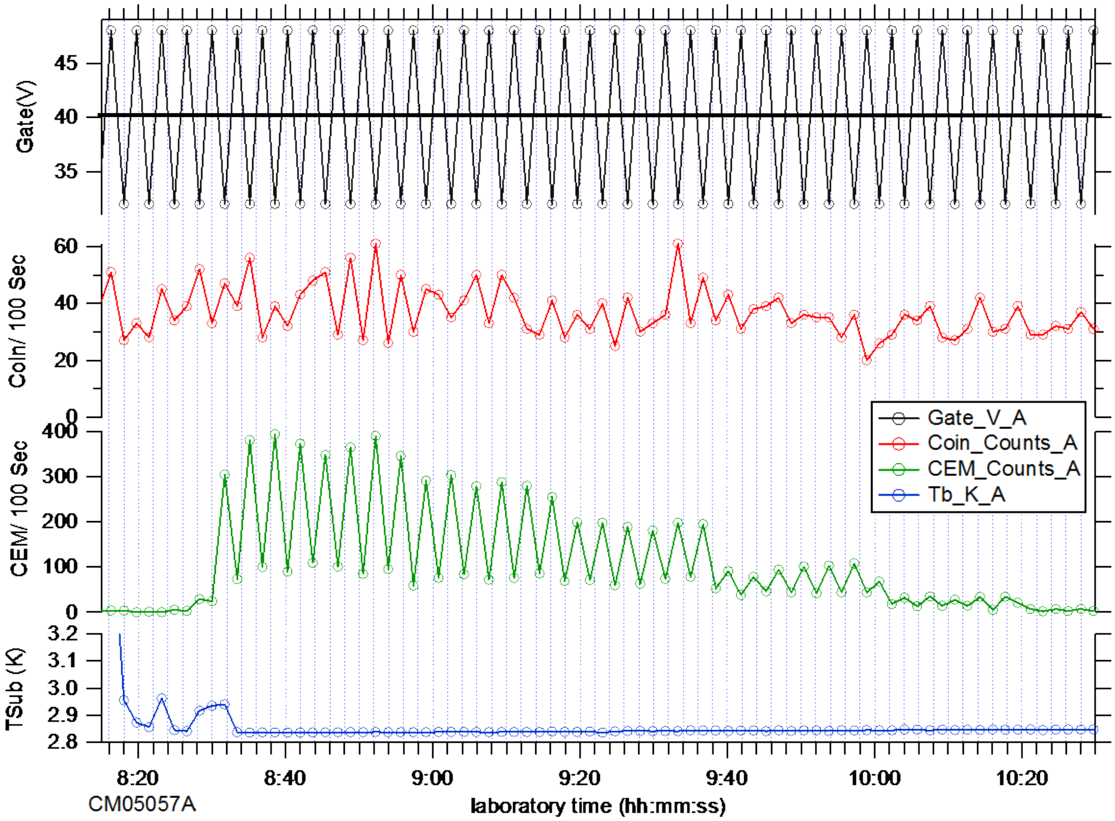

Figure 94. CO attenuator grown on 10.6-μm-thick Ne moderator [CM05057A]
1.63 mmol Ne through $T_{o/p}$ = 27.0 K o/p converter + 11.3 μmol CO deposited in five steps

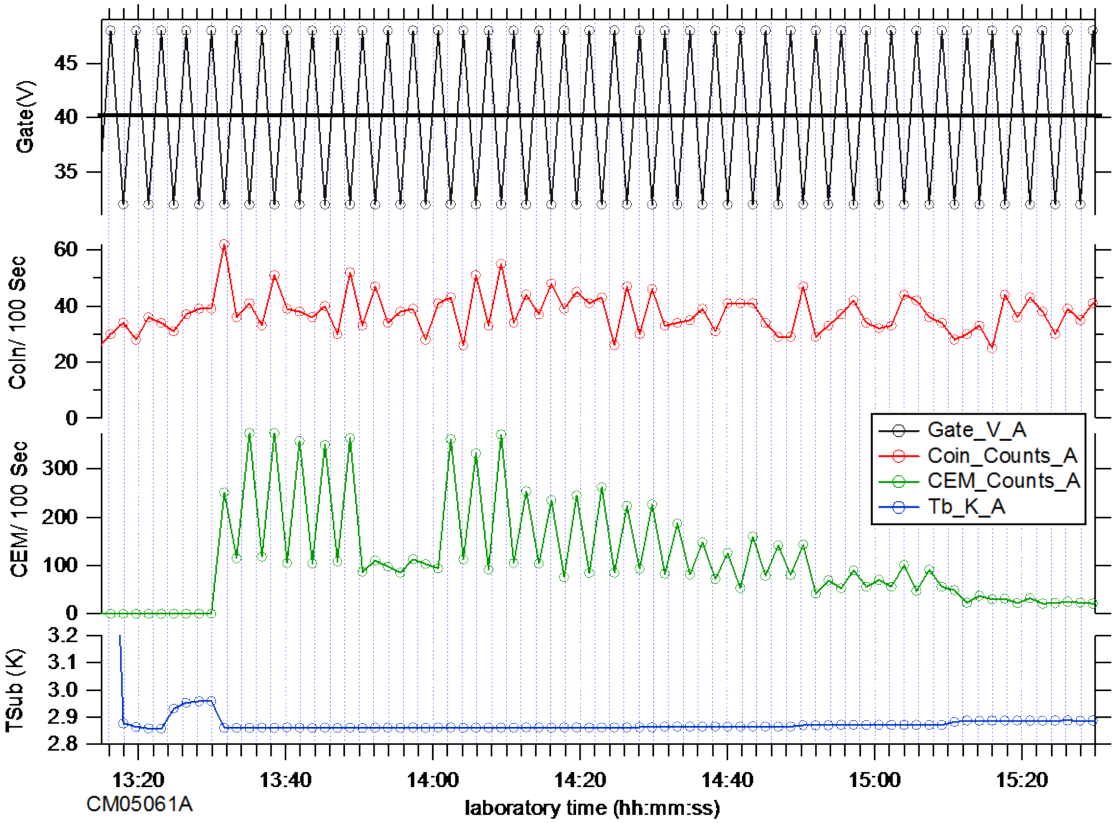

Figure 95. H_2O attenuator grown on 10.9-µm-thick Ne moderator [CM05061A]
1.61 mmol Ne through $T_{o/p}$ = 27.0 K o/p converter + 3.64 µmol H_2O deposited in four steps
Permanent magnet applied to positron transport tube from 13:50:30 to 13:59:00

Figure 95 also shows the effect of placing a strong permanent magnet in contact with the outer wall of the magnetically guided slow positron transport tube. We estimate that this produces a transverse magnetic field of ≈ 60 G at center of transport tube, completely blocking the passage of slow positrons. However, the CEM signal for the RPA Off state does not go to zero, confirming that this contribution to the signal is not due to transport of a charged species.

3.D.3. Solid H_2O on solid Kr

Figure 96 shows the CEM signal during RPA scans for an amorphous water ice layer deposited very slowly onto a working Kr moderator. Prior to the H_2O deposition, the CEM signal for the RPA On condition was ≈ 5 cps, so the ice layer has decreased the slow positron yield to less than half the original value.

Figure 97 shows a broad IR absorption peaking near 3290 cm^{-1} due to the amorphous ice layer [71,83,84]. In principle, we should be able to quickly calculate a thickness for this ice layer from the strength of this absorption feature. However, our thickness values calculated by comparison with spectra presented in Refs. [71], [83], and [84] differ by more than a factor of two, and we require additional study to understand this discrepancy. Hence we limit our thickness estimate to ~ 100 nm, with no specified error estimate. Nonetheless, it is clear that

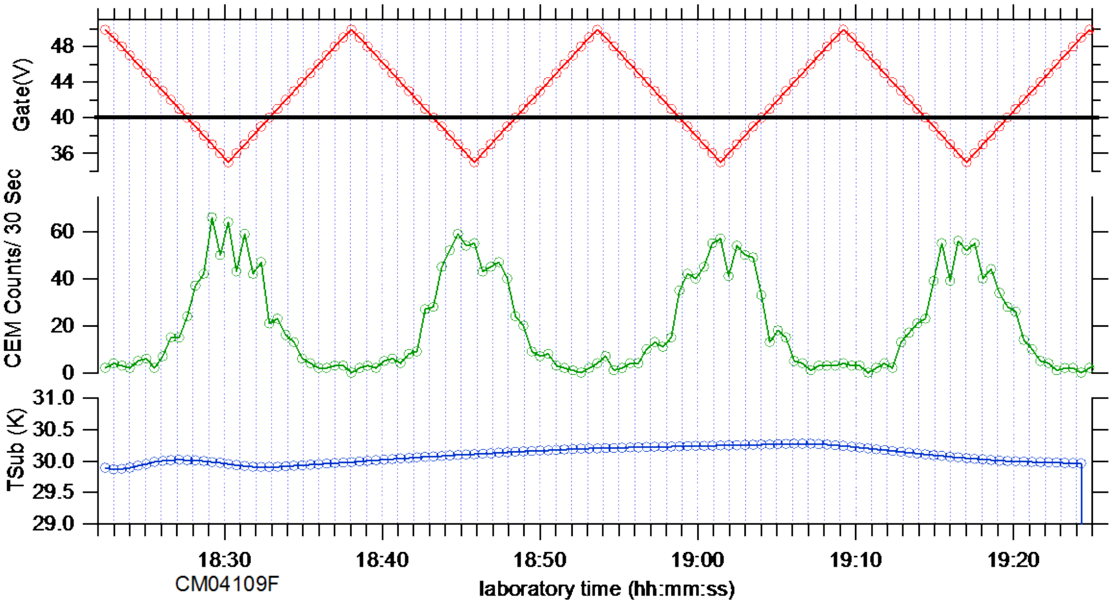

Figure 96. H_2O attenuator on 31.6-μm-thick Kr moderator [CM04109F]
1.54 mmol Kr through $T_{o/p}$ = 120 K o/p converter + 9.4 μmol H_2O deposited over 4.4 hours

the 9.4 μmol H_2O deposited onto the Kr moderator has less effect than the 3.64 μmol H_2O deposited onto the Ne moderator in Figure 95.

Figure 98 shows the RPA scan compiled from the data in Figure 96, which appears considerably broadened and shifted to lower retarding potential than the data shown for Kr moderators above in Section 3.C.3. It is unclear if this shift is due to surface charging effects, or to a modification to the positron KED by the amorphous water ice overlayer.

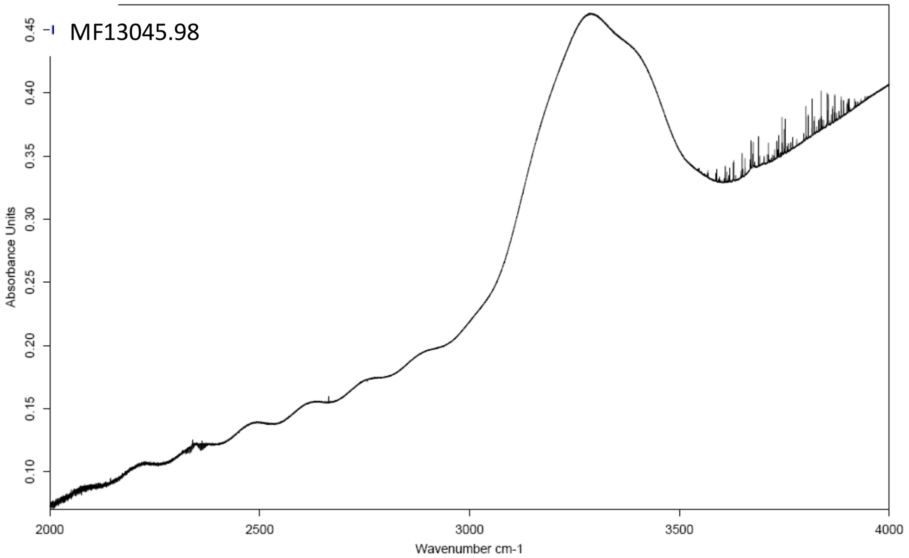

Figure 97. IR absorbance spectrum of sample depicted in Figure 96 [MF13045.98]

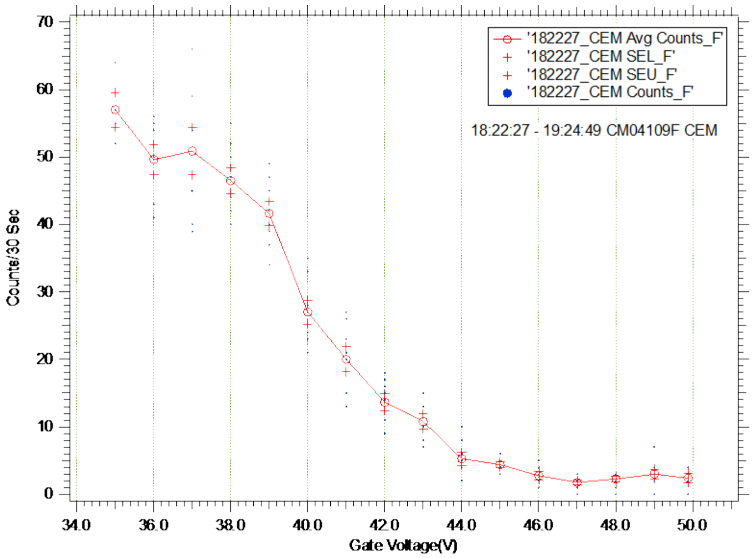

Figure 98. Compiled RPA scans for data shown in Figure 96 [CM04109F] <On> = 1.8 cps, <Off> = 0.1 cps, 50% @ 39.8 V, $\Delta V_{10\text{-}90}$ = 6.1 V

3.E. Positron Moderation Experiments in Doped Rg Moderators

3.E.1. Doped solid Ne

We also wanted to determine if the strong positron attenuation observed for the H_2, D_2, CO, and H_2O cryosolid overlayers was due to collective effects in these solids, or if the positrons would also interact strongly with the individual molecules isolated in the Rg moderators.

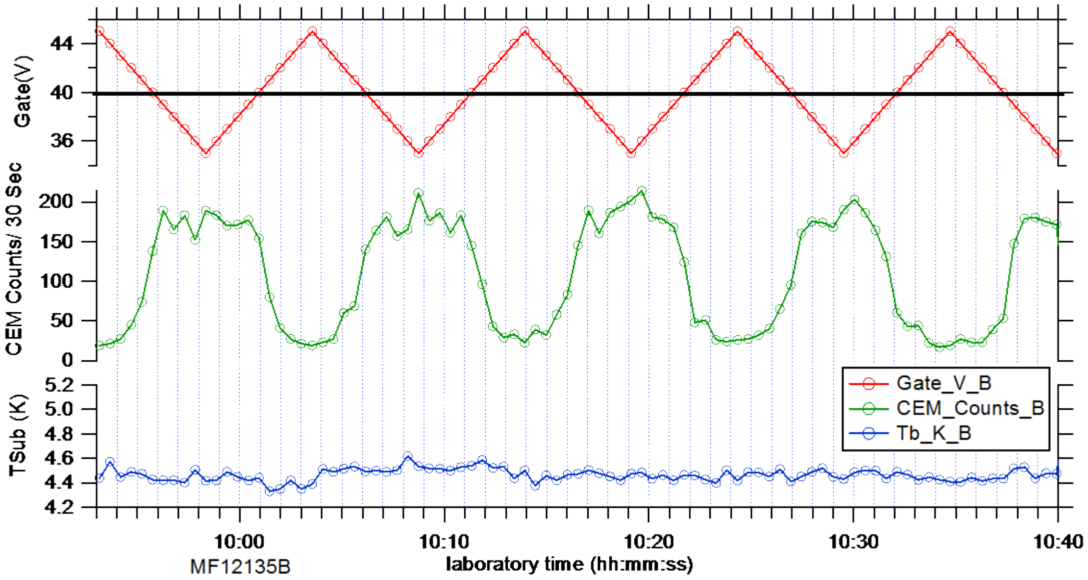

Figure 99. ≈ 47-mm-thick 1% Ar/Ne moderator [MF12135B] 6.48 mmol Ne through $T_{o/p}$ = 27.0 K o/p converter co-deposited with 68 μmol Ar over 45 min.

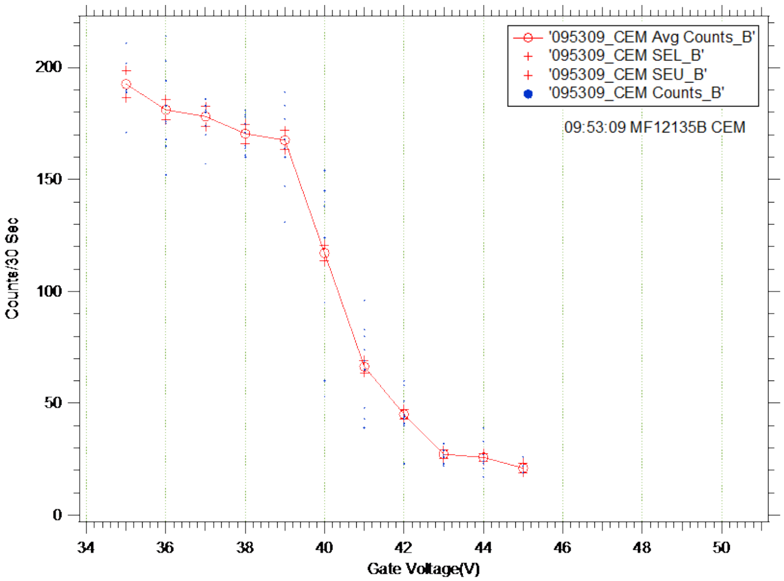

Figure 100. Compiled RPA scans for data shown in Figure 99 [MF12135B] <On> = 6.0 cps, <Off> = 0.9 cps, 50% @ 40.2 V, $\Delta V_{10\text{-}90}$ = 4.0 V

To test the effects of simple structural disorder caused by impurities in solid Ne, we codeposited a 1 % Ar-doped-in-Ne (Ar/Ne) moderator, as shown in Figure 99. The ≈ 6 cps CEM signal in the RPA On mode is only about 1/3 of that expected for a pure Ne moderator of this thickness, but it is more than double the best signals we obtained from pure Ar moderators. The compiled RPA scans in Figure 100 show a considerable broadening of the RPA On - Off transition relative to pure Ne moderators.

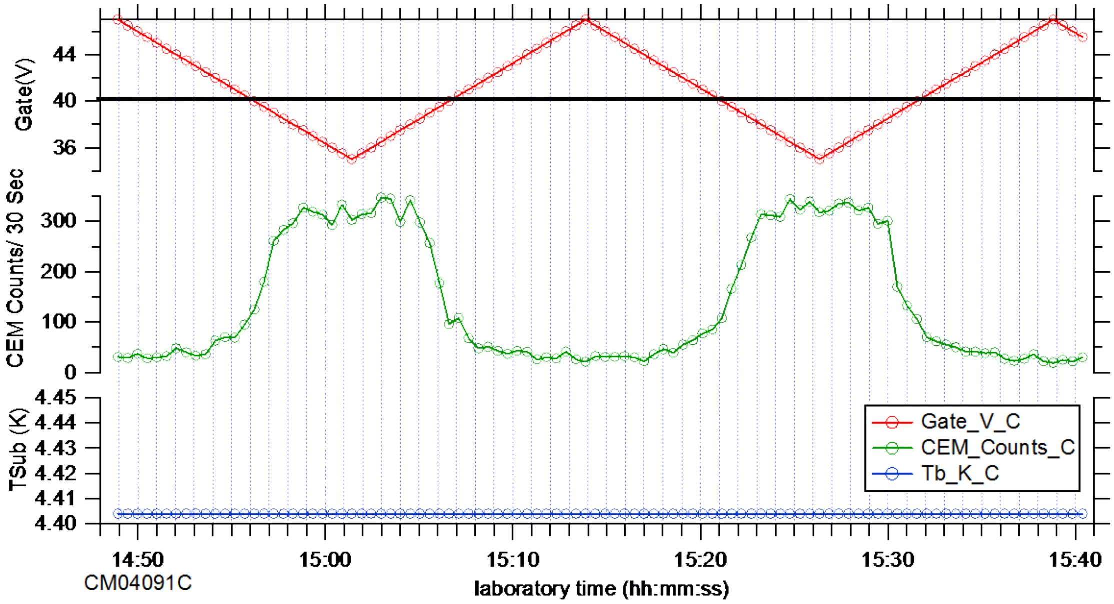

Figure 101. ≈ 62-µm-thick 220 ppm CO/Ne moderator [CM04091C] 8.65 mmol Ne through $T_{o/p}$ = 27.0 K o/p converter co-deposited with 1.87 µmol CO over 29 min

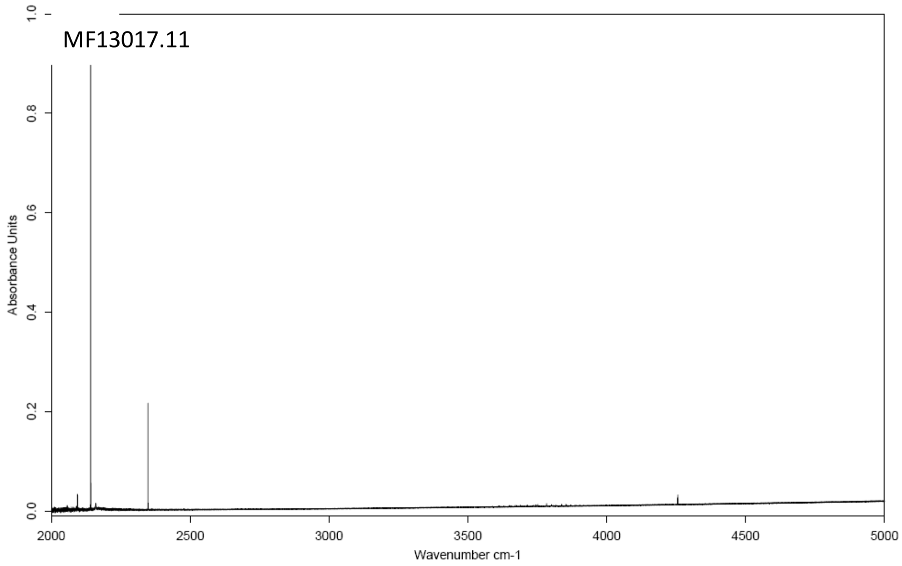

Figure 102. IR absorbance spectrum of sample depicted in Figure 101 [MF13017.11]

Figure 101 shows results from a thick, nominally 220 ppm CO/Ne moderator; the much lower concentration CO dopant is almost as effective at reducing the slow positron yield as is the 1 % Ar dopant. The spectrum in Figure 102 shows clear peaks for $^{13}C^{16}O$ near 2094 cm^{-1}, for $^{12}C^{16}O$ near 2141 cm^{-1}, for $^{12}C^{16}O_2$ near 2348 cm^{-1}, and for the $^{12}C^{16}O$ overtone near 4255 cm^{-1}.

Figure 103 shows compiled RPA scan data for this sample. The RPA On to Off transition appears to be slightly broader than for the pure Ne moderator of comparable thickness shown above in Figure 58.

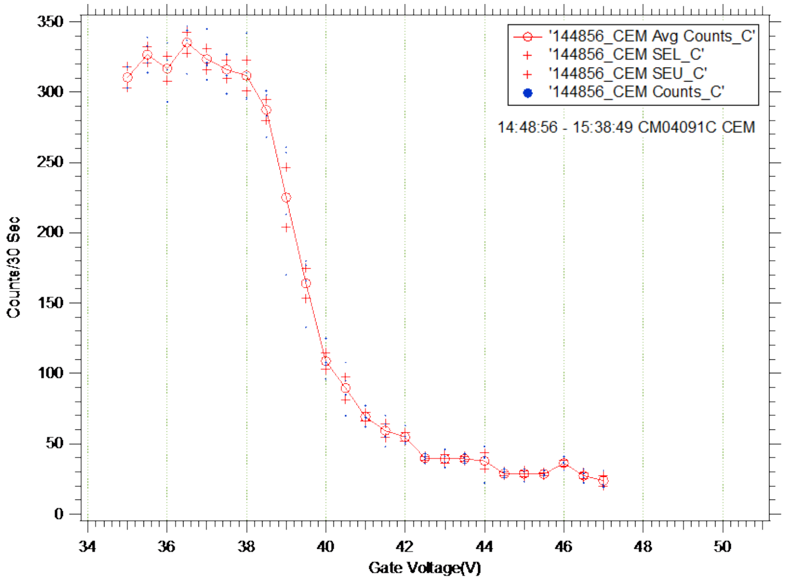

Figure 103. Compiled RPA scans for data shown in Figure 101 [CM04091C]
<On> = 10.7 cps, <Off> = 1.0 cps, 50% @ 39.6 V, $\Delta V_{10\text{-}90}$ = 3.2 V

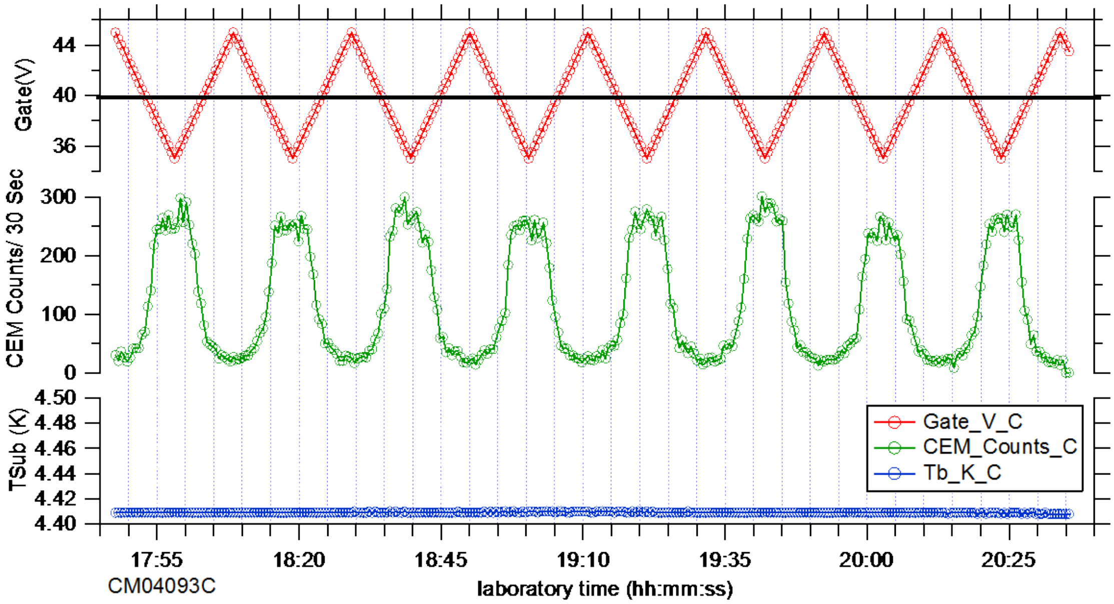

Figure 104. ≈ 61-µm-thick 600 ppm CO/Ne moderator [CM04093C] 8.50 mmol Ne through $T_{o/p}$ = 27.0 K o/p converter co-deposited with 5.13 µmol CO over 30 min

Figure 104 shows results from a nominally 600 ppm CO/Ne moderator codeposited later in the same day as the 220 ppm CO/Ne sample depicted in Figure 101; the slow positron yield is decreased even further by the additional CO dopant. As expected, Figure 105 shows roughly 3x stronger versions of the same trapped CO and CO_2 IR absorptions seen above in Figure 102. The RPA scan data in Figure 106 clearly show additional broadening of the RPA On to Off transition, and a shift of the midpoint to lower retarding potential.

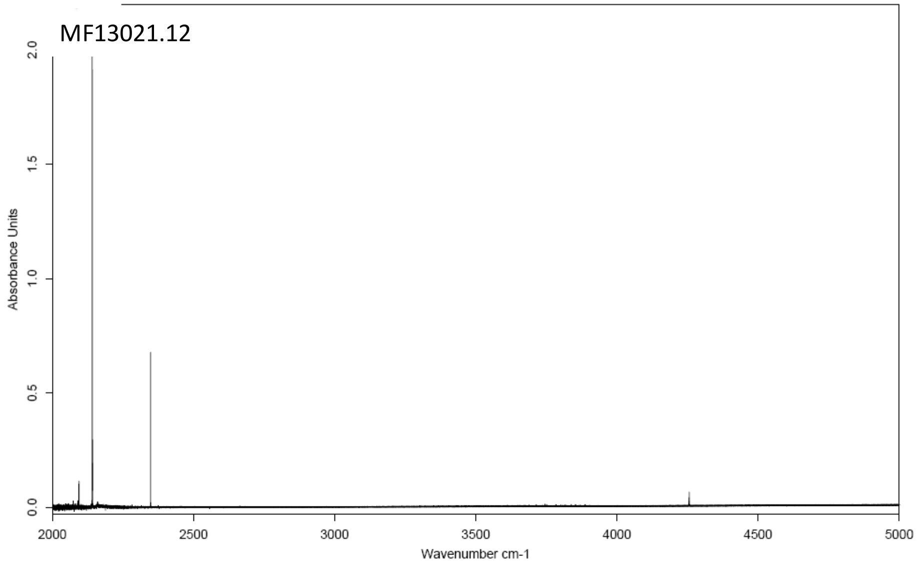

Figure 105. IR absorbance spectrum of sample depicted in Figure 104 [MF13021.12]

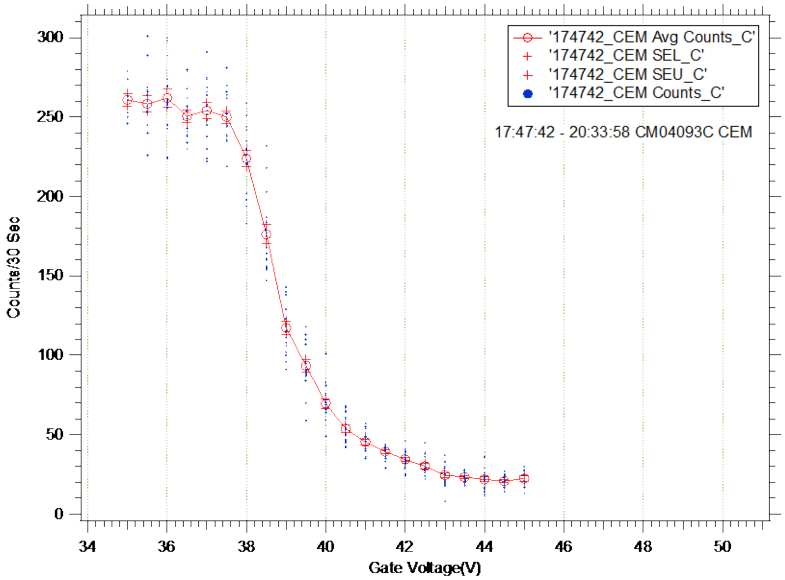

Figure 106. Compiled RPA scans for data shown in Figure 104 [CM04093C] <On> = 8.7 cps, <Off> = 0.7 cps, 50% @ 38.8 V, $\Delta V_{10\text{-}90}$ = 4.2 V

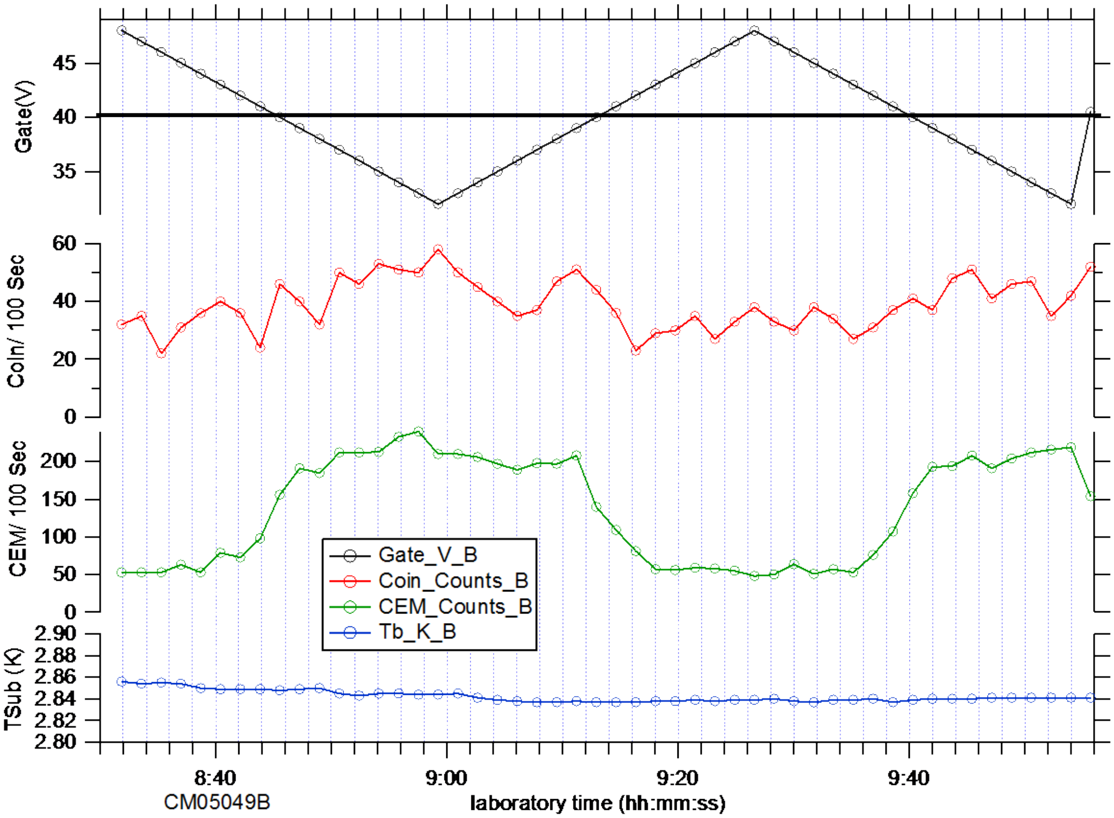

Figure 107. 10.1-µm-thick 660 ppm nH_2/Ne moderator [CM05049B] 1.63 mmol Ne through $T_{o/p}$ = 27.0 K o/p converter co-deposited with 1.10 µmol nH_2 over 6 min

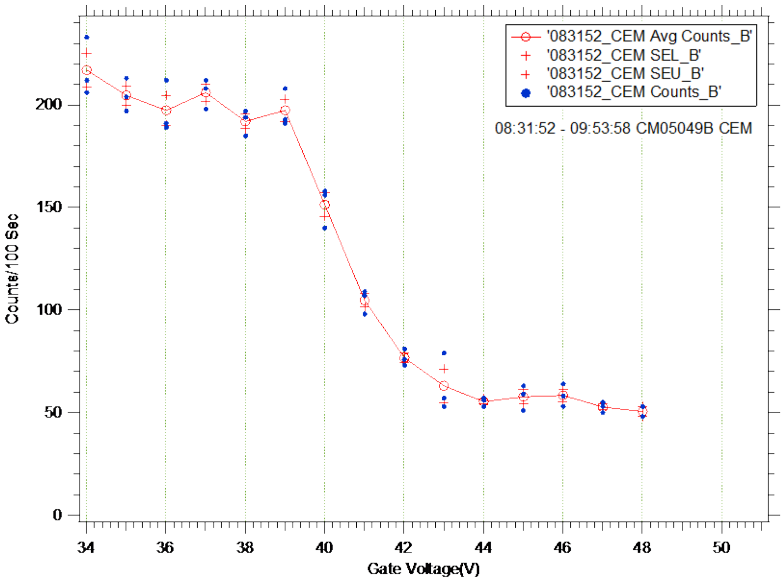

Figure 108. Compiled RPA scans for data shown in Figure 107 [CM05049B] <On> = 2.1 cps, <Off> = 0.6 cps, 50% @ 40.4 V, $\Delta V_{10\text{-}90}$ = 3.4 V

Figure 107 shows results from a nominally 660 ppm nH_2/Ne moderator; the compiled RPA scans for these data are shown in Figure 108. The nH_2 dopant reduces the positron yield about 1/2 of that for the contemporary and comparable thickness pure Ne moderators depicted at the starts of Figures 93-95, and broadens the RPA On - Off transition.

3.E.2. Doped solid Kr

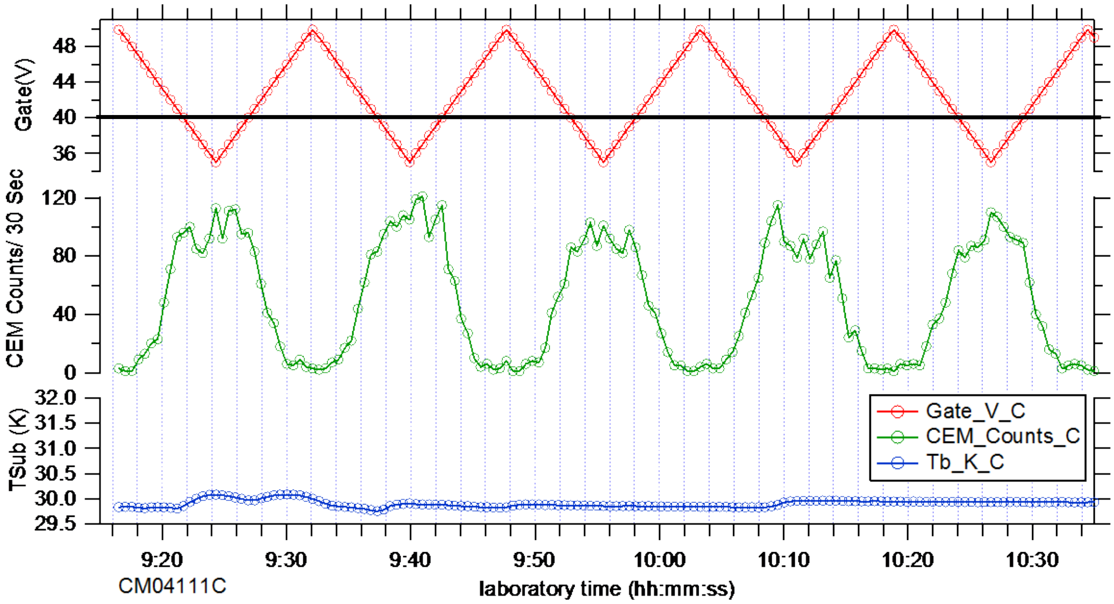

Figure 109. 25.3-µm-thick 280 ppm H_2O/Kr moderator [CM04111C] 1.55 mmol Kr through $T_{o/p}$ = 307 K o/p converter co-deposited with 0.43 µmol H_2O over 31 min

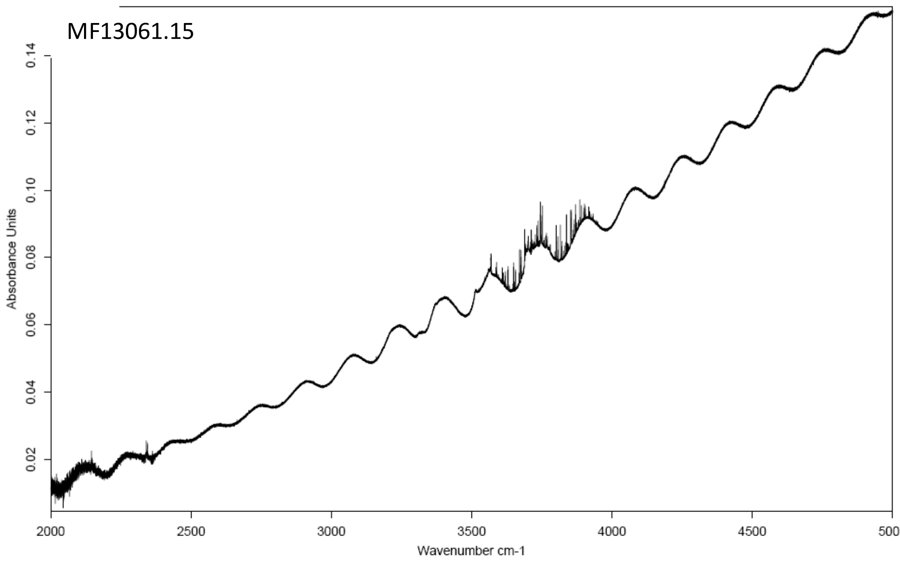

Figure 110. IR absorbance spectrum of sample depicted in Figure 109 [MF13061.15]

Figure 109 shows results from a nominally 280 ppm H_2O/Kr moderator. The H_2O dopant reduces the slow positron yield to about 2/3 of that for the comparable thickness pure Kr moderator depicted above in Figure 75. Figure 110 shows clear transmission interference fringes, and water monomer and cluster absorptions, notably: cyclic-$(H_2O)_3$ at 3514 cm^{-1}, and $(H_2O)_2$ at 3569 cm^{-1} [77]. The compiled RPA scan data in Figure 111 fall in line with our previously presented data from nominally pure Kr moderators.

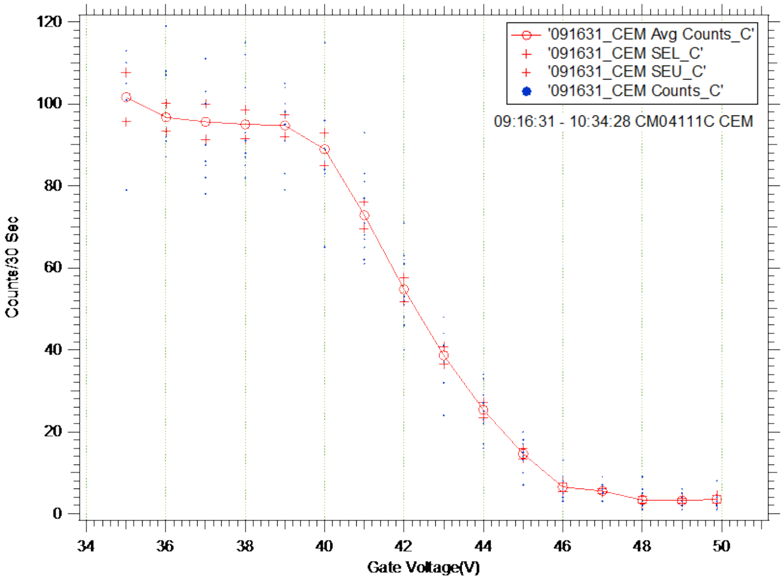

Figure 111. Compiled RPA scans for data shown in Figure 110 [CM04111C]
<On> = 3.2 cps, <Off> = 0.1 cps, 50% @ 42.2 V, ΔV_{10-90} = 5.2 V

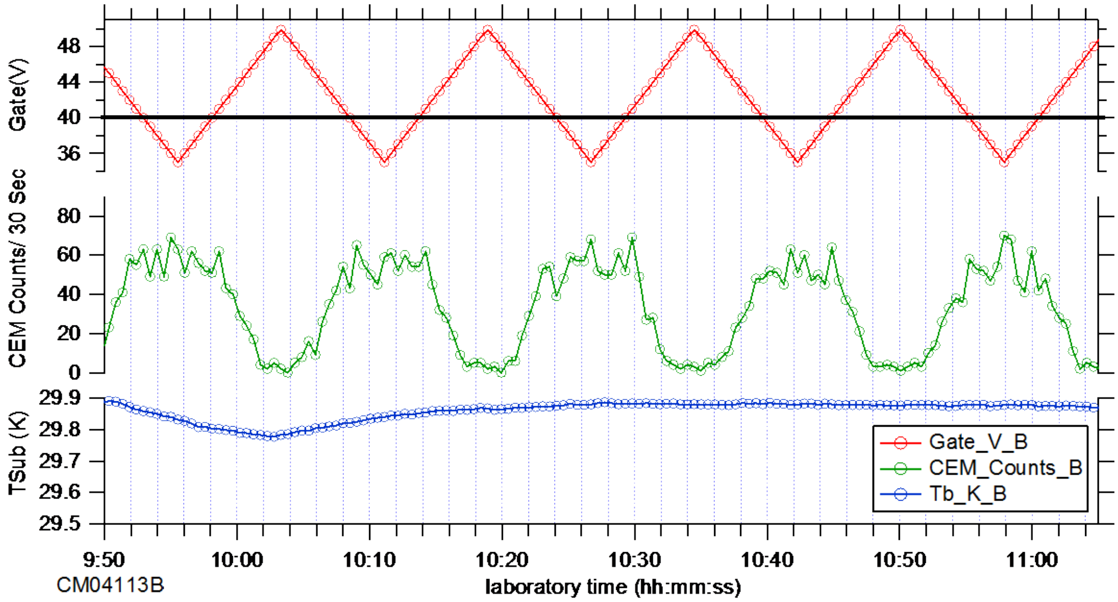

Figure 112. 32.8-µm-thick 1700 ppm H_2O/Kr moderator [CM04113B] 1.81 mmol Kr through $T_{o/p}$ = 307 K o/p converter co-deposited with 3.13 µmol H_2O over 38 min

Figure 112 shows results from a nominally 1700 ppm H_2O/Kr moderator. The additional H_2O dopant further reduces the slow positron yield to less than ½ of that shown in Figure 75. Figure 113 shows clear transmission interference fringes, stronger versions of the water cluster absorption seen in Figure 110, and new peaks for cyclic-$(H_2O)_4$ at 3370 cm^{-1} [77], and at 3312 cm^{-1} {$(H_2O)_5$?} and 3208 cm-1 {$(H_2O)_6$?}. The compiled RPA scan data in Figure 114 show a shift to higher retarding potentials and considerable broadening compared to pure Kr moderators.

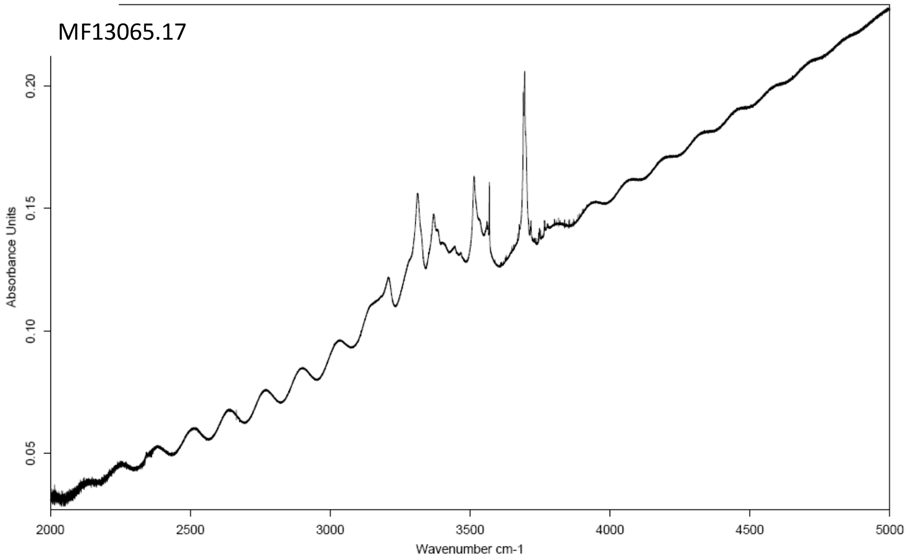

Figure 113. IR absorbance spectrum of sample depicted in Figure 112 [MF13065.17]

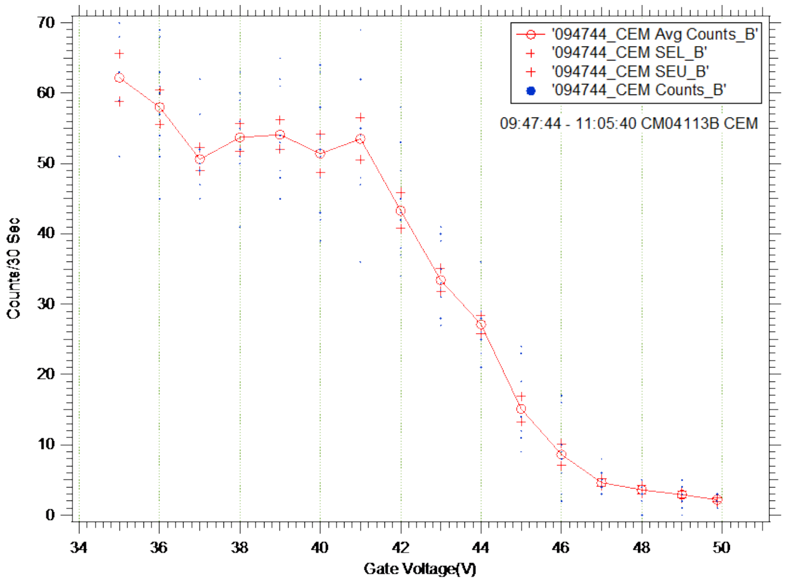

Figure 114. Compiled RPA scans for data shown in Figure 112 [CM04113B]
<On> = 1.8 cps, <Off> = 0.1 cps, 50% @ 43.6 V, $\Delta V_{10\text{-}90}$ = 6.2 V

4. DISCUSSION

4.A. Spectroscopic Characterization of Cryogenic Moderators

The application of Matrix Isolation Spectroscopy (MIS) to characterizing cryogenic solid positron moderators provides new information that illuminates a number of issues. The simple analysis of the observed transmission/reflection interference fringes presented above in Section 2.C.4 yields a quantitative measure of the physical thickness of the moderator. The side view of the pH_2 solid depicted above in Figure 39 reveals a wedged shape deposit, thicker at the bottom of the substrate which is closer to the cold pH_2 gas delivery tube [57]. We expect similar shapes for moderators up to a few mm thick; for thicker solids shadowing of the top of the deposition substrate leads to more pronounced wedging and eventually to a highly curved deposit [65]. We estimate a ± 10 % variation in thickness from the centerline value across the ≈ 8-mm-tall field of view of the photo. According to the SIMION calculations presented in Figure 27, this field of view corresponds roughly with the region of the moderator from which slow positrons are efficiently collected and launched into the solenoid transport tube. So we take ± 10 % as a reasonable estimate of the range of moderator thicknesses contributing to each of our slow positron measurements.

The IR diagnostic is also useful in assessing the purity of a moderator, and in identifying the presence of an overcoated layer of a strong IR absorber, like the water ice shown above in Figure 97. The IR spectra can also provide quantitative concentrations for well-isolated dopants or impurities [65]. At higher concentrations, this analysis is complicated by dopant clustering, especially for species like H_2O which engage in strong hydrogen-bonding that alters the inherent strengths of the IR absorptions. In such cases, a concentration estimate can still be made by comparison of the "fingerprint" pattern of cluster absorption features (*e.g*. Figures 110 and 113) with those of samples with known dopant concentrations.

For pH_2 solids, we can calculate sample thicknesses directly from the pH_2 absorptions, using the approach described in Figure 17 and Tables 3 and 4, and as demonstrated above for the sample depicted in Figure 89. High resolution IR spectra of pH_2 solids reveal a wealth of information, including: the mixed hcp/fcc microstructure of as-deposited solids seen in Figure 35, the laboratory frame alignment of annealed hcp crystallites revealed by analysis of the PIRAS spectra shown in Figures 36 and 37, the quantitative determination of residual oH_2 content from the impurity-induced IR absorptions as shown for Figure 87. We are still analyzing data to calibrate the strengths of the IR absorptions of nH_2 and nD_2 solids to enable thickness measurements, and will report these results later. We had hoped to detect the presence of charged radiation damage products in our pH_2 solids, as suggested by Figure 18, but the relatively low dosages absorbed in our experiments did not yield observable signals.

The main downside of employing MIS techniques in our experiments is the requirement for optical access to the cryogenic moderator. Our brute-force implementation, with irregularly shaped holes cut into the radiation shield, results in direct radiative heating of the moderators by the room-temperature surroundings. Additionally, our choice of a vertical orientation for the deposition cryostat axis and a perpendicular horizontal orientation for the slow positron transport tube results in breaking the cylindrical symmetry about the axis of the positron collection ion optics. This (along with the grounded radiation shield with the irregular optical access hole) introduces large variations in the electric fields experienced by the slow positrons on their way from the moderator to the ion optics, and may account for much of the ≈ 1.2 V width of the RPA On to Off transition seen above in Figure 41.

4.B. Positron Moderation

We begin this section by confirming that our CEM signals are due to slow positrons.

4.B.1. Origin of CEM signal

Figure 115 shows a correlation plot for the γ–γ coincidence and CEM data obtained from a 24.6-μm-thick Ne moderator, as presented above in Figure 62. The strong linear correlation demonstrates that some part of the CEM signal is due to slow positrons arriving in the Annihilation chamber, but the non-zero intercept of the straight line fit deserves additional comment.

The backgrounds (with ^{22}Na source in Active position, warm moderator substrate) for the two measurement techniques are indicated by the two blue dashed lines in Figure 115. Even though we placed lead brick shielding between the ^{22}Na source and the NaI(Tl) detectors (see Figures 33 and 34), Compton scattering by the surroundings of the gamma radiation escaping the Moderation chamber leads to a ≈ 0.3 cps background for the γ–γ coincidence channel. This is comparable to the difference between RPA On and Off coincidence signals shown in Figure 115, and illustrates why this measurement channel did not see more use during our project. In contrast, the background for the much more sensitive CEM channel is an order of magnitude lower (≈ 0.03 cps). However, the CEM signal in the RPA Off state does not return to the background in this experiment, demonstrating that there is another contribution to the CEM signal besides slow positrons.

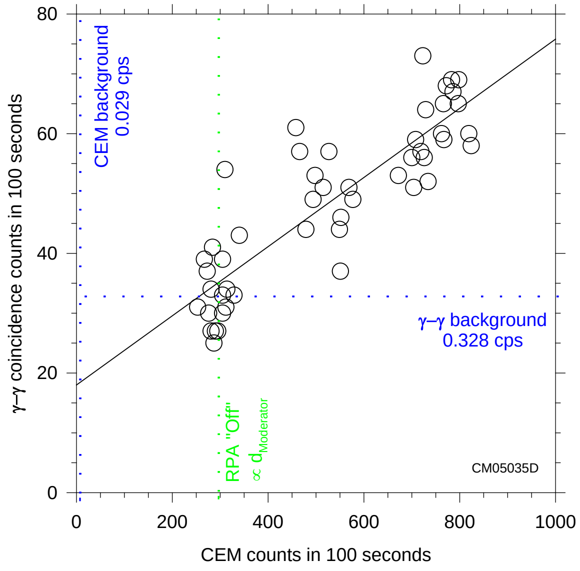

Figure 115. γ–γ coincidence and CEM data from Figure 62 [CM05035D]

We considered and discarded a number of candidates for the source of the RPA Off CEM signal. It requires the presence of a ~ 10 μm thickness cryogenic moderator, so we exclude Compton-scattered or X-ray fluorescence photons from the Au/Cu deposition substrate. Application of a strong transverse magnetic field to the slow positron transport tube midpoint has no effect on the signal, as shown above in Figure 95, demonstrating that it is not due to transport of a charged species between the Moderator and Annihilation chambers. We imagine two plausible possibilities: (1) vacuum ultraviolet (VUV) photoemission from the irradiated Rg moderators [85], and gas-phase transport of neutral metastable electronically excited Rg* atoms.

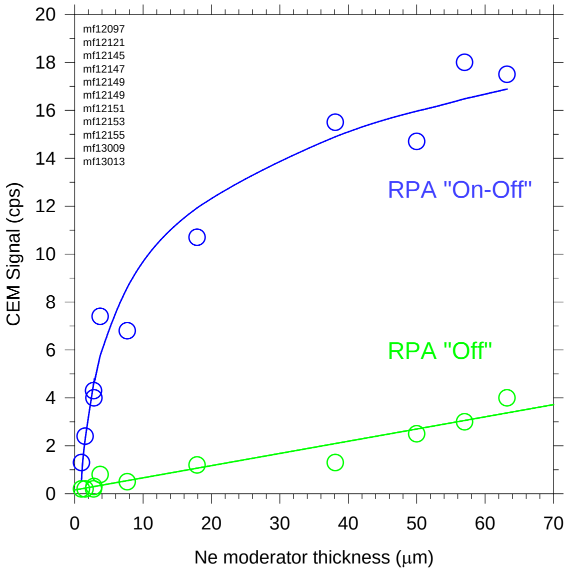

Figure 116. CEM signals *vs.* Ne moderator thickness; RPA <On> - <Off> and <Off>

Figure 116 shows a plot of the CEM signals from only those Ne moderators for which we were able to measure the thicknesses from the interference fringes in the IR spectra. The upper curve shows the amplitude of the RPA modulated CEM signal, *i.e*. the difference observed between the On and Off states, and the bottom shows the RPA Off CEM signal. The linear growth of the RPA Off CEM signal with sample thickness suggests that the entire bulk of the Ne moderator contributes to the signal. Likewise, the ability of the unknown carrier to pass through the initial overcoat layers in the attenuation experiments depicted in Figures 91, 93, 94 and 95 also argues against a surface-emission process. Hence, we believe that volumetric VUV photoemission from the moderator, with these photons reflected at the bend of the positron transport tube onto the CEM detector, is the most likely explanation.

We confirmed that the CEM detector is very sensitive to UV illumination by a Hg/Ar pen lamp. We also attempted (unsuccessfully) to detect the VUV emission from working Rg moderators directly using a solar-blind photomultiplier tube, which is only sensitive to 160-320 nm photons, placed just outside a MgF_2 window on the side of the Moderation chamber. Unfortunately, the VUV emissions of Ne, Ar, and Kr do not overlap the sensitive wavelength region of the PMT, and the Xe* emission at 175 nm [85] is on the high-energy edge of the PMT response curve, so this null result is inconclusive.

The growth of the RPA On minus RPA Off CEM signal in Figure 116 seems to follow a logarithmic dependence on moderator thickness; the solid line fit is for $y = y_0 + a \log_{10}(x)$, with $y_0 = 0.585$ cps, $a = 3.931$ cps, and x in microns. The simple 1-D model discussed in Appendix A predicts an exponential growth with a definite asymptote. Unfortunately, we were not able to extend our interferometric thickness determinations far enough to establish this limit with confidence.

4.B.2. Apparent shifts in RPA scans

For our Ne moderators, we observe a clear shift of the midpoints of the RPA scans to lower retardation potential with increasing moderator thickness. The trends for Ar, Kr, and Xe moderators are not as clear, and perhaps are masked by their broader On to Off transitions, and/or their weaker signals relative to Ne. One possible contribution to the observed shift for Ne samples is that the vacuum surfaces of the thicker moderators are simply closer to the ion optics package, so that those moderators release positrons at lower electrostatic potentials. However, the spacing between the deposition substrate and the first collection element is 39 mm, so a potential difference of 85 V corresponds to an electric field of only 2.2 V/mm (or 2.2 mV/μm) which is much too small to account for the observed shifts. Thus, surface charging of the moderators [78,79] appears to be the most likely explanation.

We speculate that the lesson of the Ne moderator grown “in the dark” (see Figures 59-61) is that the ultimate distribution of charged species depends on the manner in which the moderator is first exposed to the radiation from the ^{22}Na source. The gradual growth in moderator efficiency over the first 20 minutes of irradiation must somehow be due to the buildup of these charged products, possibly at the moderator surface? This could account for the very narrow RPA On to Off transition, and the low midpoint retarding potential.

4.B.3. Relative positron moderation efficiencies

Figure 117 shows compiled RPA scans for “typical” Ne, Kr, Ar, and pH_2 moderators. The sequence of observed moderation efficiencies $\varepsilon_{Ne} > \varepsilon_{Kr} > \varepsilon_{Ar}$ matches the literature [20-26]. The CEM signal for the pH_2 solid does not appear to be modulated by the RPA scan; its average magnitude of 0.13 cps is less than 2% of the modulated CEM signal for the Ne moderator. For another example, the average CEM signal for the pH_2 solid shown in Figure 86 is 0.08 cps, the RPA On minus Off modulated CEM signal for the contemporary Ne moderator in Figure 56 is 20.3 cps. Even ascribing the entire magnitude of the pH_2 CEM signal in Figure 86 to slow positrons yields a limit on the positron moderation efficiency of solid pH_2 of $\varepsilon_{pH2} < 0.004\ \varepsilon_{Ne}$.

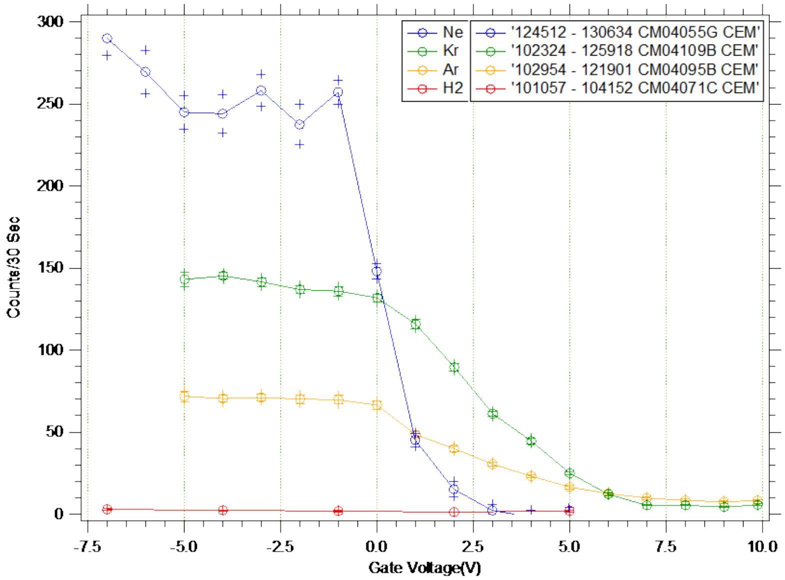

Figure 117. Comparison of RPA scans for typical Ne, Kr, Ar, and pH_2 moderators [CM04055G, CM04109B, CM04095B, CM04071C]

4.C. Positron Attenuation by Cryosolid Layers

4.C.1. Ne moderators

Figure 118 shows a comparison of the attenuation of slow positrons from Ne moderators overcoated by solid nH_2, nD_2, CO, and H_2O layers. The normalized RPA On minus RPA On CEM signals are plotted against the amount of attenuator gas deposited. Using the analysis discussed above in connection with Figure 92, we estimate the thickness of the solid nH_2 layer yielding 50 % attenuation of the slow positrons as ≈ 15 nm. The observed ordering of positron attenuation effectiveness $H_2O > CO > nH_2 > nD_2$ agrees with the trend of total cross sections for positron-molecule scattering at ≈ 1 eV energies [86-88]. The fact that nH_2 is more effective than nD_2 at stopping slow positrons points to the role of molecular rotational and/or vibrational states; the 0.5 eV absorbed by an H_2 molecule upon vibrational excitation may be just the right amount of on energy needed to stop the positrons. Finally, we demonstrated above in Figure 90 that slow positrons do not cross a buried $Ne:pH_2(200nm):Ne$ interface, so the strong slow positron attenuation by nH_2 is not a property of the vacuum surface of the nH_2 solid.

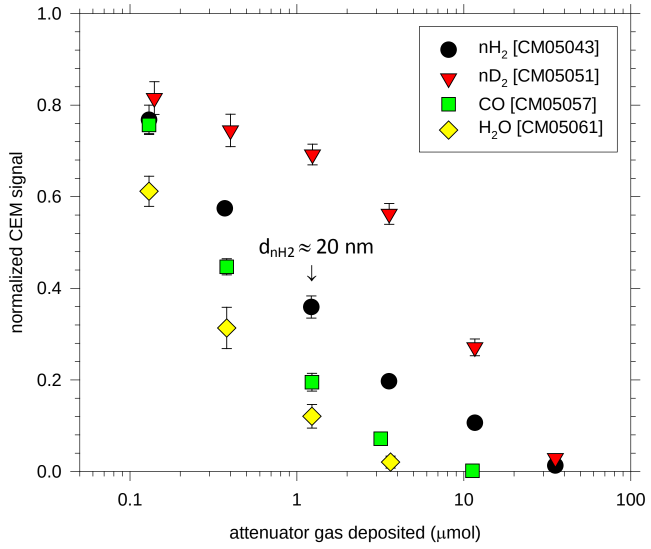

Figure 118. Positron attenuation by nD$_2$, nH$_2$, CO, and H$_2$O overlayers on Ne moderators

4.C.2. Kr moderators

The much broader KED for slow positrons emitted from Kr moderators (as compared to Ne) may be responsible for the differences observed in positron attenuation experiments. Figure 119 shows a comparison of compiled RPA scans for the pure Kr moderator depicted

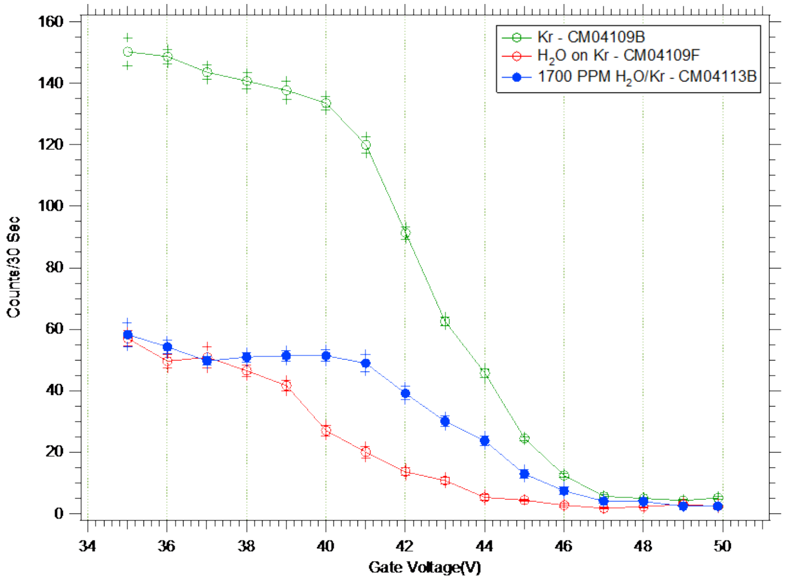

Figure 119. Comparison of effects of H$_2$O in and on Kr moderators [CM04109B, CM04109F, CM04113B]

109B: <On> = 4.7 cps, <Off> = 0.2 cps, 50% @ 42.6 V, $\Delta V_{10\text{-}90}$ = 5.0 V

109F: <On> = 1.8 cps, <Off> = 0.1 cps, 50% @ 39.8 V, $\Delta V_{10\text{-}90}$ = 6.1 V

113B: <On> = 1.8 cps, <Off> = 0.1 cps, 50% @ 43.6 V, $\Delta V_{10\text{-}90}$ = 6.2 V

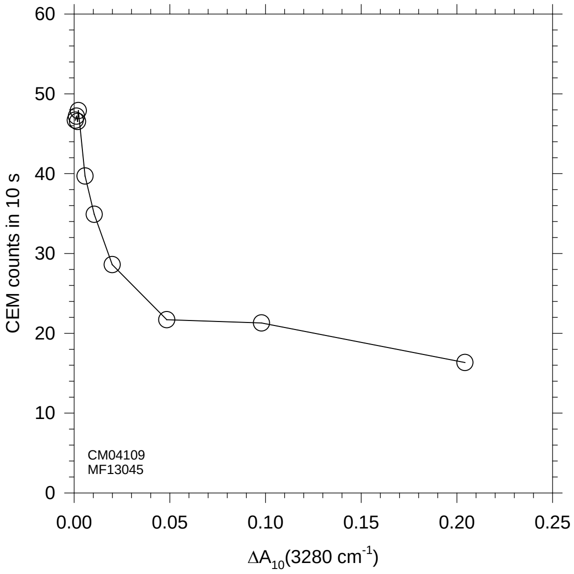

Figure 120. Dependence of CEM signal on H_2O ice thickness on Kr moderator [CM04109]

above in Figure 75, the ~ 100-nm-thick water ice coated Kr moderator (9.4 μmol H_2O) depicted in Figure 96, and the 1700 ppm H_2O/Kr moderator (3.13 μmol H_2O) depicted in Figure 112. As mentioned above in Section 3.D.3, and by comparison with the Ne moderator data summarized in Figure 118, the water ice coating is much less effective at stopping slow positrons from Kr than from Ne. The water ice coating also shifts the midpoint of the RPA scan to lower retarding potential by nearly 3 V.

Rather surprisingly, the smaller amount of H_2O (3.13 μmol) dispersed as monomers and small clusters throughout the 1700 ppm H_2O/Kr moderator is as effective as the larger amount (9.4 μmol H_2O) deposited as a solid water ice overlayer. Part of the answer to this riddle may be seen in Figure 120, which shows the strange dependence of the slow positron signal on the thickness of the H_2O overlayer (represented by the height of the 3280 cm^{-1} IR absorption feature shown in Figure 97). Initially, the positron signal drops rapidly with ice thickness, but then this trend levels off; as if the additional ice was not impeding the progress of positrons that transited the earlier deposits. One possible explanation is that the upper layers of the ice deposit are formed with lower densities than the underlying amorphous ice, and perhaps have even become porous.

4.D. Positron Attenuation by Dispersed Dopants

Figure 121 shows slow positron signals from three ≈ 30-μm-thick Kr moderators containing increasing concentrations of H_2O dopant, estimated as 1, 280, and 1700 ppm. The general trend of decreasing moderation efficiency with increasing H_2O dopant concentration agrees with the results reported in Ref. [89], but our nominal dopant concentrations required to produce a given effect differ from theirs by two-to-three orders of magnitude. Figure 122 shows IR absorption spectra of the three Kr moderators, from which we hope to tease out confirmation for our dopant concentration estimates.

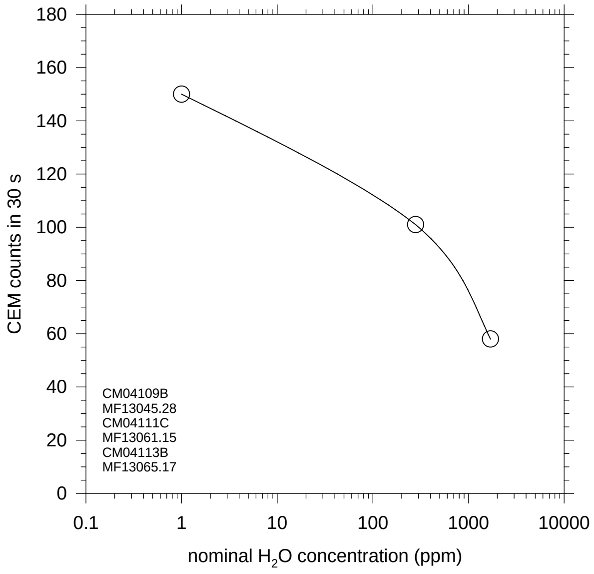

Figure 121. Dependence of CEM signal on H_2O dopant concentration in Kr moderators [CM04109B, CM04111C, CM04113B]

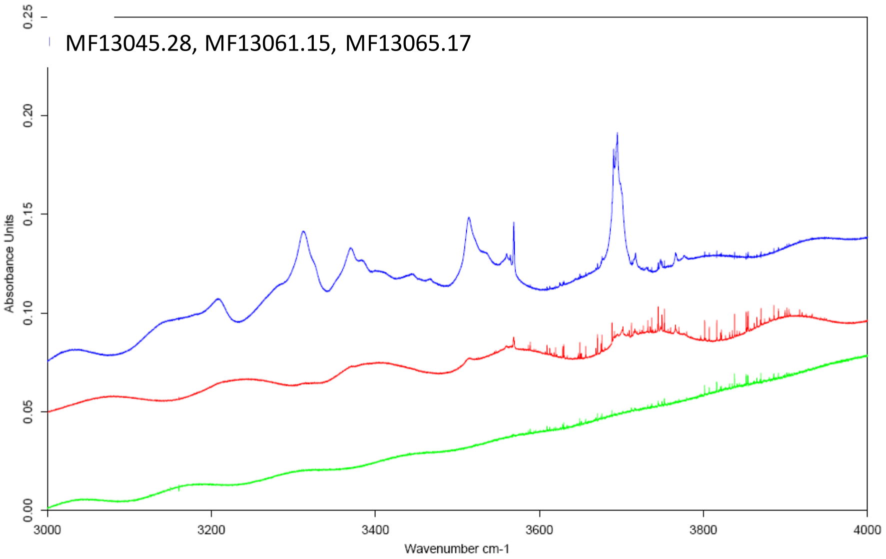

Figure 122. IR absorbance spectrum of samples depicted in Figure 121 [MF13045.28, MF13061.15, MF13065.17]

5. CONCLUSIONS

Despite all our hopes and expectations to the contrary, solid pH_2 is not a positron moderator. We did not see any influence of the residual oH_2 concentration on the effectively-zero positron moderation efficiency of our hydrogen solids. The slightly weaker appetite for slow positrons emerging from a Ne moderator exhibited by nD_2 *vs*. nH_2 solid films (Figure 118) points to the role of the molecular rovibrational states. We note that the positron-Ne total scattering cross section has a ≈ 2-eV-wide transmission "window" centered at a collision energy of ≈ 1 eV [90]. This corresponds roughly with the kinetic energies of the moderated positrons emitted from solid Ne. The positron-H_2 total scattering cross section increases dramatically for decreasing collision energies below ≈ 2 eV [88], closing off the Ne transmission/moderation window. A brief search of the literature did not turn up any positron-D_2 scattering data; it would be very interesting to see if the lower excitation energies to the D_2 rovibrational states make a noticeable difference in the energy dependence of total scattering cross section.

The application of matrix isolation spectroscopy techniques to the study of positron moderation in cryogenic solids offers real and valuable advantages. We are able to accurately determine *via* interferometry the centerline thicknesses of our moderators; an improved gas delivery geometry could yield flat, non-wedged deposits. We can also analyze the absorption spectra to quantify the amounts of isolated dopants and/or surface deposits for infrared-active species. An improved implementation should include preservation of axial symmetry between the cryogenic deposition substrate, the radiation shield, and the ion optics. Perhaps fiber optics could be used to provide optical access to the moderator through minimum sized holes in the radiation shield?

The combination of physical separation of the ^{22}Na positron source from the cryogenic deposition substrate, and the use of a simple reflection moderation geometry, offers valuable experimental advantages. For example, it enables experiments to isolate the effects of accumulated surface impurities from those of built-up radiation damage on the early time dependence of the moderation efficiency. The "grown in the dark" Ne moderator experiment depicted in Figure 59 shows an increase in moderation efficiency in the first ≈ 20 minutes of exposure to the ^{22}Na source. However, this sample had already been exposed to residual impurities in the vacuum environment for ≈ 30 minutes prior. This result illuminates the similar early-time growth in moderation efficiency reported in Ref. [89].

Finally, the single most practical result from this study is that surprisingly thin films of solid CO or H_2 can influence the moderation efficiency of a rare gas solid. Since these are the dominant residual gas species in an ultrahigh vacuum chamber, our results may serve to motivate additional efforts to mitigate their access to the cryogenic moderator in long-endurance experiments.

APPENDIX A: Positron Moderation Efficiency 1-D Model

We extend a simple one-dimensional (1-D) reflection geometry moderation model [1] to include positron moderation in transmission geometry. The main parameters of this model are the characteristic implantation depth (ℓ) for fast positrons, and the characteristic hot diffusion length (L_+) for epithermal positrons. Assuming a fast positron implantation profile:

$$P_{imp}(x) = (1/\ell)\exp(-x/\ell) \tag{A1}$$

and a surface return probability:

$$P_{ret}(x) = \exp(-x/L_+) \tag{A2}$$

we calculate the positron moderation efficiencies as a function of the moderator thickness, D. In reflection geometry:

$$P_{mod}(D) = (1/\ell)\int_0^D \quad P_{imp}(x)\, P_{ret}(x)\, dx \tag{A3}$$

$$= [L_+/(\ell + L_+)]\,[1 - \exp\{-D[(\ell + L_+)/\ell\, L_+]\}] \tag{A4}$$

which has the limit:

$$P_{mod}(D) \to L_+/(\ell + L_+) \text{ as } D \to \infty \tag{A5}$$

In transmission geometry:

$$P_{mod}(D) = (1/\ell)\int_0^D \quad P_{imp}(x)\, P_{ret}(D-x)\, dx \tag{A6}$$

$$= [L_+/(\ell - L_+)]\,[\exp(-D/\ell) - \exp(-D/L_+)] \tag{A7}$$

Setting the derivative of Equation (6) with respect to D to zero yields the optimum transmission moderator thickness:

$$D_{opt} = [\ell\, L_+/(\ell - L_+)]\, \log_e(\ell\, /L_+) \tag{A8}$$

The transmission moderator efficiency at this thickness D_{opt} reduces to:

$$P_{mod}(D_{opt}) = (\ell/L_+)\ \hat{}\ [\ell/(L_+ - \ell)] \tag{A9}$$

where the caret signifies exponentiation, *i.e.*: $a \ \hat{}\ b = a^b$.

The results plotted in Figure 4 have the functional forms shown in Equation (A5) and Equation (A9).

APPENDIX B: Naïve PIRAS Polarization Analysis

A general analysis of the polarization dependences in our experiment would require the calculation of crystal-field-perturbed rotational states for dopant molecules in hcp pH_2 solid crystallites having arbitrary orientations relative to the deposition substrate -- which is beyond the scope of this report. Instead, we discuss our doped solid pH_2 IR spectral data within the framework of a highly idealized model system, conceding that the severe simplifying assumptions and approximations employed may limit the applicability of this model to other experimental configurations.

Consider an IR beam undergoing specular reflection off a metal surface lying in the x-y plane of a right-handed coordinate system, with the beam propagation direction making incident and outgoing angles, θ, relative to the metal surface normal, $\hat{z}$. We adopt the standard notation [68] for describing the polarization of the IR beam in terms of two perpendicular components:

"*p-polarized*" for which the electric field, $\vec{E}_p = E_p \hat{e}_p$, lies in the plane of reflection, and

"*s-polarized*" for which $\vec{E}_s = E_s \hat{e}_s$ is parallel to the metal surface.

We further define the plane of reflection as the x-z plane, and $\hat{e}_s$ to be parallel to $\hat{y}$, *i.e.*:

$$\hat{e}_p \bullet \hat{z} = \sin\theta \qquad \hat{e}_s \bullet \hat{z} = 0 \qquad \text{(B1a)}$$

$$\hat{e}_p \bullet \hat{x} = \cos\theta \qquad \hat{e}_s \bullet \hat{x} = 0 \qquad \text{(B1b)}$$

$$\hat{e}_p \bullet \hat{y} = 0 \qquad \hat{e}_s \bullet \hat{y} = 1 \qquad \text{(B1c)}$$

We assume that the pH_2 solid consists of hcp crystallites with their c-axes perfectly aligned with the surface normal, so the same space-fixed x-y-z coordinate system applies to the crystal field perturbation acting on the rotating dopant molecules. In particular, we can identify transitions having a parallel (||, $\Delta M = 0$) polarization dependence relative to the hcp c-axis with transition moments pointing in the $\hat{z}$ direction, and perpendicular (⊥, $\Delta M = \pm 1$) transitions with transition moments pointing in the x-y plane.

We further assume that the weakly anisotropic solid pH_2 crystal field is a very minor perturbation to the dopant rigid-rotor wave functions for J = 0 and J = 1. More specifically, we assume that we can use the free-space relations for transition intensities between Zeeman sub-levels for the dopant R(0) [$J=1 \leftarrow J=0$] line. The electric dipole transition matrix elements, $\vec{\mu}$, for rovibrational transitions are given in a particularly convenient form for polarization-dependent problems in Ref. [91]; simplifying their notation somewhat yields for R-branch ($\Delta J = +1$) transitions:

$$\text{for } \Delta M = -1, \qquad \vec{\mu} = \tfrac{1}{2}\,\mu_R\,[(J' - M')(J' - M' - 1)]^{1/2}\,(\hat{x} + i\,\hat{y}) \qquad \text{(B2a)}$$

$$\text{for } \Delta M = +1, \qquad \vec{\mu} = -\tfrac{1}{2}\,\mu_R\,[(J' + M')(J' + M' - 1)]^{1/2}\,(\hat{x} - i\,\hat{y}) \qquad \text{(B2b)}$$

$$\text{for } \Delta M = 0, \qquad \vec{\mu} = \mu_R\,[J'^2 - M'^2]^{1/2}\,\hat{z} \qquad \text{(B2c)}$$

where: μ_R is a reduced matrix element containing the effects of all other relevant quantum numbers (*e.g.* $\mu_R = \mu_R(v, K_a, K_c)$ for an asymmetric top rotor), and J' and M' refer to the final (upper) state.

The transition probabilities are proportional [91] to the square of the inner-product of $\vec{\mu}$ and the applied electric field, $\vec{E} = E\,\hat{e}$; *i.e.*: $P \propto |\vec{\mu} \bullet \vec{E}|^2$. Thus, for the dopant R(0) transition we obtain for the polarization dependent transition probabilities:

$$P_{\|,p} \propto \mu_R^2\, E_p^2 \sin^2\theta \tag{B3a}$$
$$P_{\perp,p} \propto \mu_R^2\, E_p^2 \cos^2\theta \tag{B3b}$$
$$P_{\|,s} = 0 \tag{B3c}$$
$$P_{\perp,s} \propto \mu_R^2\, E_s^2 \tag{B3d}$$

Glossing over the steps [92] connecting these microscopic transition probabilities to the macroscopic observed experimental absorbances, A, we eliminate spectrometer-dependent terms like E_p^2 and E_s^2 yielding:

$$A_{\|,p} = k'\, \mu_R^2 \sin^2\theta \qquad = \tfrac{1}{2}\, k'\, \mu_R^2 \text{ for } \theta = 45° \tag{B4a}$$
$$A_{\perp,p} = k'\, \mu_R^2 \cos^2\theta \qquad = \tfrac{1}{2}\, k'\, \mu_R^2 \text{ for } \theta = 45° \tag{B4b}$$
$$A_{\|,s} = 0 \tag{B4c}$$
$$A_{\perp,s} = k'\, \mu_R^2 \tag{B4d}$$

where: k' is an arbitrary constant. Thus, for our present experimental configuration with $\theta = 45°$, this simple model predicts absorption intensity ratios between parallel and perpendicular polarized features of $A_{\|}(s+p) : A_{\perp}(s+p) = 1 : 3$ in perfectly unpolarized (s+p) absorption spectra, and $A_{\|}(s-p) : A_{\perp}(s-p) = -1 : 1$ in (s-p) PIRAS spectra. We can also apply this model to the transparent substrate normal incidence transmission geometry employed in the previous Edwards AFB experiments by taking $\theta = 0°$, in which case the model predicts $A_{\|,p} = A_{\|,s} = 0$; *i.e.*: no absorption features due to ||-polarized transitions should be observed.

APPENDIX C: Numerical Integration of Newtonian Dynamics with Velocity Dependent Forces

We present here an *ad-hoc* numerical integration scheme for calculating the trajectory of a charged particle in a magnetic field:

$$\vec{F} = m\ \vec{a}$$
$$\vec{F}(\vec{x}, \vec{v}) = q\ \vec{v} \times \vec{B}(\vec{x})$$

with $\vec{x}(0)$, $\vec{v}(0)$ given, which we adapted from several existing numerical integration schemes.

Euler integration:

$$x(t + \Delta t) = x(t) + v(t)\,\Delta t + ½\, a(t)\,(\Delta t)^2$$
$$v(t + \Delta t) = v(t) + a(t)\,\Delta t$$

Position Verlet:

$$x(t + \Delta t) = 2x(t) - x(t - \Delta t) + a(t)\,(\Delta t)^2$$
$$v(t) = [x(t + \Delta t) - x(t - \Delta t)] / 2\Delta t$$

Velocity Verlet:

$$x(t + \Delta t) = x(t) + v(t)\,\Delta t + ½\, a(t)\,(\Delta t)^2$$
$$v(t + \Delta t) = v(t) + ½\,[a(t) + a(t + \Delta t)]\,\Delta t$$

The Velocity Verlet equation for the future velocity requires information about future forces, which for the Lorentz force equation also requires knowledge of the future velocity. So a way must be found to provide a suitable velocity estimate for the purpose of calculated the future forces.

In the present scheme, the first timestep is taken using simple Euler integration over a sequence of greatly reduced timesteps ($\delta t \sim \Delta t/100$), yielding x(0), x(1), v(0), and v(1). The simulation is then propagated using this algorithm:

$$x(t + \Delta t) = 2x(t) - x(t - \Delta t) + a(t)\,(\Delta t)^2$$
$$v_{trial}(t + \Delta t) = v(t) + a(t)\,\Delta t$$
$$a_{trial}(t + \Delta t) = (1/m)\, F(x(t + \Delta t), v_{trial}(t + \Delta t))$$
$$v(t + \Delta t) = v(t) + ½\,[a(t) + a_{trial}(t + \Delta t)]$$

This method yields much better energy conservation than the simple Euler method.

REFERENCES

1. M. Charlton and J.W. Humberston, Positron Physics, (Cambridge University Press, Cambridge, 2001).
2. C.M. Surko and F.A. Gianturco, eds., New Directions in Antimatter Chemistry and Physics, (Kluwer, Dordrecht, Netherlands, 2001).
3. Y.C. Jean, P.E. Mallon, and D.M. Schrader, eds., Principles and Applications of Positron & Positronium Chemistry, (World Scientific Publishing, Singapore, 2003).
4. R.L. Forward and J. Davis, Mirror Matter, (iUniverse.com, Inc., Lincoln, Nebraska, 2001).
5. P.W. Cooper, Explosives Engineering, Chapter 22, (Wiley, New York, 1996).
6. R. Ramaty, J.M. McKinley, and F.C. Jones, Astrophysical J. **256**, 238 (1982). "On the theory of gamma-ray amplification through stimulated annihilation radiation."
7. E.P. Liang and C.D. Dermer, Opt. Comm. **65**, 419 (1988). "Laser cooling of positronium."
8. P.M. Platzman and A.P. Mills, Jr., Phys. Rev. B **49**, 454 (1994). "Possibilities for Bose condensation of positronium."
9. D.B. Cassidy and J.A. Golovchenko, "The Bose-Einstein condensation of positronium in submicron cavities," Ch. 6 in New Directions in Antimatter Chemistry and Physics, C.M. Surko and F.A. Gianturco eds. (Kluwer, 2001).
10. A.P. Mills, Jr., Nucl. Instr. Meth. B **192**, 107 (2002). "Positronium molecule formation, Bose-Einstein condensation and stimulated annihilation."
11. A.P. Mills Jr., D.B. Cassidy, and R.G. Greaves, Materials Science Forum **445**, 424 (2004). "Prospects for Making a Bose-Einstein-Condensed Positronium Annihilation Gamma Ray Laser."
12. D.B. Cassidy, S.H.M. Deng, R.G. Greaves, T. Maruo, N. Nishiyama, J.B. Snyder, H.K.M. Tanaka, and A.P. Mills, Jr., Phys. Rev. Lett. **95**, 195006 (2005). "Experiments with a High-Density Positronium Gas."
13. D.B. Cassidy and A.P. Mills, Jr., Nature **449**, 195 (2007). "The production of molecular positronium."
14. L. Brilloiun, Phys. Rev. **67**, 260 (1945). "A Theorem of Larmor and its importance for electrons in magnetic fields."
15. L. Turner and D.C. Barnes, Phys. Rev. Lett. **70**, 798 (1993). "Brillouin limit and beyond: a route to inertial-electrostatic confinement of a single-species plasma."
16. R.G. Greaves and C.M. Surko, AIP Conference Proceedings **CP606**, 10 (2002). "Practical limits on positron accumulation and creation of electron-positron plasmas."
17. J. Ackerman, J. Shertzer, and P. Schmelcher, Phys. Rev. Lett. **78**, 199 (1997). "Long-lived states of positronium in crossed electric and magnetic fields."
18. T. Chiueh, Chinese J. Phys. **35**, 344 (1997). "Exotic atom: double-helix positronium."
19. P. Schmelcher, J. Ackermann, J. Shertzer, Nuc. Instr. Meth. B **143**, 202 (1998). "Stabilization of matter-antimatter atoms in crossed electric and magnetic fields."
20. A.P. Mills, Jr. and E.M. Gullikson, Appl. Phys. Lett. **49**, 1121 (1986). "Solid neon moderator for producing slow positrons."
21. R. Khatri, M. Charlton, P. Sferlazzo, K.G. Lynn, A.P. Mills, Jr., and L.O. Roelling, Appl. Phys. Lett. **57**, 2374 (1990). "Improvement of rare-gas solid moderators by using conical geometry."
22. E.M. Gullikson and A.P. Mills, Jr., Phys. Rev. Lett. **57**, 376 (1986). "Positron dynamics in rare-gas solids."

23. A.P. Mills, Jr., S.S. Voris, Jr., and T.S. Andrew, Appl. Phys. Lett. **76**, 2556 (1994). “Solid Kr moderator for producing slow positrons.”
24. M.P. Petkov, K.G. Lynn, L.O. Roellig, and T.D. Troev, Appl. Surf. Sci. **116**, 13 (1997). “An investigation of positrons interacting with solid argon, krypton, and xenon.”
25. J. Jaaskelainen, T. Laine, K. Fallstrom, K. Saarinen, and P. Hautojarvi, Appl. Surf. Sci. **116**, 73 (1997). “Optimized growth conditions for solid Ar and Kr moderators in slow positron beam.”
26. A. Ozen, A.J. Garner, and G. Laricchia, Nuc. Instr. Meth. B **171**, 172 (2000). “Rare gas solid moderator for Ps beam at UCL.”
27. J.A. Venables and B.L. Smith, “Crystal Growth and Crystal Defects,” in Rare Gas Solids Vol. II, edited by M.L. Klein and J.A. Venables (Academic Press, London, 1977).
28. D.A. McQuarrie, Statistical Mechanics (Harper & Row, New York, 1976). The H_2 molecule exists in two forms: “para” (pH_2) with paired nuclear spins (I=0) and even rotational quantum numbers (J=0, 2, ...), or “ortho” (oH_2) with I=1 and odd J. The two forms interconvert very slowly in the absence of a catalyst.
29. M.R. Berman, editor, Proceedings of the High Energy Density Matter (HEDM) Contractors’ Conference held 24-26 October 2000 in Park City, UT, (Air Force Office of Scientific Research, AFRL, 2001).
30. D.R. Harshman, et al., Phys. Rev. B **36**, 8850 (1987). “Generation of slow positive muons from solid rare-gas moderators.”
31. M.C. Fujiwara, et al., Phys. Rev. Lett. **85**, 1642 (2000). “Resonant formation of dμt molecules in deuterium: an atomic beam measurement of muon catalyzed dt fusion.”
32. T.A. Porcelli, et al., Phys. Rev. Lett. **86**, 3763 (2001). “Measurement of the resonant dμt molecular formation rate in solid HD.”
33. H.L. Anderson and E.R. Cohen, “General Section,” in A Physicist’s Desk Reference, H.L. Anderson, ed. (AIP, New York, 1989).
34. I.F. Silvera, Rev. Mod. Phys. **52**, 393 (1980). “The solid molecular hydrogens in the condensed phase: Fundamentals and static properties.”
35. C. Kittel, Introduction to Solid State Physics, Sixth Edition (Wiley, New York, 1986).
36. J. Van Kranendonk, “Solid Hydrogen,” (Plenum, New York, 1983).
37. T. Oka, Annu. Rev. Phys. Chem. **44**, 299 (1993). “High-resolution spectroscopy of solid hydrogen.”
38. T. Momose and T. Shida, Bull. Chem. Soc. Jpn. **71**, 1 (1998). “Matrix-isolation spectroscopy using solid parahydrogen as the matrix: application to high-resolution spectroscopy, photochemistry, and cryochemistry.”
39. T. Momose, C. M. Lindsay, Y. Zhang, and T. Oka, Phys. Rev. Lett., **86**, 4795 (2001). “Sharp spectral lines observed in γ-ray ionized parahydrogen crystals.”
40. G.W. Collins, W.G. Unites, E.R. Mapoles, and T.P. Bernat, Phys. Rev. B **53**, 102 (1996). “Metastable structures of solid hydrogen.”
41. E.M. Gullikson and A.P. Mills, Jr., Phys. Rev. B **42**, 7695 (1990). “Positron spectroscopy of solid N_2.”
42. F.A. Gianturco and T. Mukherjee, Phys. Rev. A **55**, 1044 (1997). "Dynamical coupling effects in the vibrational excitation of H_2 and N_2 colliding with positrons."
43. F.A. Gianturco, T. Mukherjee and A. Occhigrossi, Phys. Rev. A **64**, 032715 (2001). "Computing positron annihilation in polyatomic gases: An exploratory study."
44. A. Gedanken, B. Raz, and J. Jortner, J. Chem. Phys. **59**, 2752 (1973).

"Far vacuum ultraviolet absorption of solid hydrogen."
45. N. Schwentner, F.J. Himpsel, V. Saile, M. Skibowski, W. Steinmann, and E.E. Koch, Phys. Rev. Lett. **34**, 528 (1975). "Photoemission from rare-gas solids: electron energy distributions from the valence bands."
46. K. Inoue, H. Kanzaki, and S. Suga, Solid State Comm. **30**, 627 (1979). "Fundamental absorption spectra of solid hydrogen."
47. N. Schwentner, E.E. Koch, and J. Jortner, Electronic Excitations in Condensed Rare Gases, (Springer-Verlag, Berlin, 1985).
48. L. Schmidt, Phys. Lett. **36A**, 87 (1971). "Energy losses of fast electrons in solid Ar, Ne, and H_2."
49. B.A. Wallace, Jr., and H. Meyer, J. Low Temp. Phys. **15**, 297 (1974). "The temperature dependence of the dielectric constant in solid H_2, D_2, ^4He, and Ne."
50. H.E. Hallam and G.F. Scrimshaw, "Experimental techniques and properties of matrix materials," in Vibrational Spectroscopy of Trapped Species, H.E. Hallam, ed. (Wiley, London, 1973).
51. M.J. Berger, J.S. Coursey, and M.A. Zucker, "ESTAR, PSTAR, and ASTAR: Computer programs for calculating stopping-power and range tables for electrons, protons, and helium ions (version 1.21)," available at: http://physics.nist.gov/Star National Institute of Standards and Technology, Gaithersburg, MD (1999).
52. R.K. Batra and M.L. Sehgal, Phys. Rev. B **23**, 4448 (1981). "Range of electrons and positrons in matter."
53. R.K. Batra, Nuc. Instr. Meth. B **28**, 195 (1987). "Approximate stopping power of low energy electrons and positrons in matter."
54. USAF Radioactive Materials Permit No. FL-00126-00/00AFP, Docket No. 030-00126.
55. M.E. Fajardo and S. Tam, J. Chem. Phys. **108**, 4237 (1998). "Rapid vapor deposition of millimeters thick optically transparent parahydrogen solids for matrix isolation spectroscopy."
56. S. Tam and M.E. Fajardo, Rev. Sci. Instrum. **70**, 1926 (1999). "Ortho/para hydrogen converter for rapid deposition matrix isolation spectroscopy."
57. M.E. Fajardo and S. Tam, J. Low Temp. Phys., **122**, 345 (2001). "CO/pH_2 -- a molecular thermometer."
58. H. Cember, Introduction to Health Physics, 3rd Edition, (McGraw-Hill, New York, 1996).
59. U.S. Nuclear Regulatory Commission, NRC Regulations (10 CFR). http://www.nrc.gov/reading-rm/doc-collections/cfr/part020/appb/Sodium-22.html
60. M.E. Fajardo, AFRL/RWME Standard Operating Procedure 91-126, "Guidelines for Production and Disposal of Cryogenic Solids in Bldg. 1200 Room 11."
61. J. Van Gompel, Solid State Technology **48**, 51 (2005). "Avoiding fire and explosion risks with proper H_2 exhaust management."
62. M.E. Fajardo and C.M. Lindsay, J. Chem. Phys. **128**, 014505 (2008). "Crystal field splitting of rovibrational transitions of water monomers isolated in solid parahydrogen."
63. M.E. Fajardo, C.M. Lindsay, and T. Momose, J. Chem. Phys. **130**, 244508 (2009). "Crystal Field Theory Analysis of Rovibrational Spectra of Carbon Monoxide Monomers Isolated in Solid Parahydrogen."
64. M.E. Fajardo, Chapter 6, "Matrix Isolation Spectroscopy in Solid Parahydrogen: a Primer," in Physics and Chemistry at Low Temperatures, L. Khriachtchev, Ed., (World Scientific, London, 2011).

65. S. Tam and M.E. Fajardo, Appl. Spectrosc., **55**, 1634 (2001). “Single and Double Infrared Absorptions in Rapid Vapor Deposited Parahydrogen Solids: Application to Sample Thickness Determination and Quantitative Infrared Absorption Spectroscopy.”
66. T. Momose, H. Hoshina, M. Fushitani, and H. Katsuki, Vib. Spectr. **34**, 95 (2004). “High-resolution spectroscopy and the analysis of ro-vibrational transitions of molecules in solid parahydrogen.”
67. S. Tam, M.E. Fajardo, H. Katsuki, H. Hoshina, T. Wakabayashi, and T. Momose, J. Chem. Phys. **111**, 4191 (1999). “High resolution infrared absorption spectra of methane molecules isolated in solid parahydrogen matrices.”
68. F.L. Pedrotti and L.S. Pedrotti, Introduction to Optics, (Prentice-Hall, Englewood Cliffs, NJ, 1987).
69. H.M. Roder, G.E. Childs, R.D. McCarty, and P.E. Angerhofer, Survey of the Properties of the Hydrogen Isotopes Below Their Critical Temperatures, NBS-TN-641, (U.S. Department of Commerce, Springfield, VA, 1973).
70. H.E. Hallam and G.F. Scrimshaw, “Experimental techniques and properties of matrix materials,” in Vibrational Spectroscopy of Trapped Species, edited by H.E. Hallam, (Wiley, London, 1973).
71. W. Hagen, A.G.G.M. Tielens and J.M. Greenberg, Chem. Phys. **56**, 367 (1981). “The Infrared Spectra of Amorphous Solid Water and Ice I Between 10 and 140 K.”
72. J.D. Jackson, Classical Electrodynamics, 2nd Edition, (Wiley, New York, 1975).
73. D.J. Manura, SIMION Version 8.0 User Manual, (Scientific Instrument Services, Inc., Ringoes, NJ, 2008).
74. R.A. Powell, Am. J. Phys. **46**, 1046 (1978). “Photoelectric effect: Back to basics.”
75. P.A. Anderson, Phys. Rev. **115**, 553 (1959). “Work function of gold.”
76. W.M.H. Sachtler, G.J.H. Dorgelo, and A.A. Holsher, Surf. Sci. **5**, 221 (1966). “The work function of gold.”
77. M.E. Fajardo and S. Tam, J. Chem. Phys., **115**, 6807 (2001). “Observation of the Cyclic Water Hexamer in Solid Parahydrogen.”
78. L.V. Jorgensen, J.P. Merrison, B.I. Deutch, M. Charlton, and G.O. Jones, Phys. Rev. B **52**, 12402 (1995). “Positron dynamics in surface-charged solid argon.”
79. F.M. Jacobsen, M. Petkov, and K.G. Lynn, Phys. Rev. B 57, 6998 (1998). “Electric-field-assisted moderator for generation of intense low-energy positron beams.”
80. A.P. Brodyanski, S.A. Medvedev, M. Vetter, J. Kreutz and H.J. Jodl, Phys. Rev. B **66**, 104301 (2002). “Nature of infrared-active phonon sidebands to internal vibrations: Spectroscopic studies of solid oxygen and nitrogen.”
81. H.P. Gush, W.F.J. Hare, E.J. Allin, and H.L. Welsh, Can. J. Phys. **38**, 176 (1960). “The Infrared Fundamental Band of Liquid and Solid Hydrogen.”
82. R.F. Barron, Cryogenic Systems, 2nd Edition (Oxford, New York, 1985).
83. M.S. Bergren, D. Schuh, M.G. Sceats, and S.A. Rice, J. Chem. Phys. **69**, 3477 (1978). “The OH stretching region infrared spectra of low density amorphous solid water and polycrystalline ice Ih.”
84. B.E. Wood and J.A. Roux, J. Opt. Soc. Am. **72**, 720 (1982). “Infrared optical properties of thin H_2O, NH_3, and CO_2 cryofilms.”
85. N. Schwentner, E.E. Koch, and J. Jortner, Electronic Excitations in Condensed Rare Gases, (Springer-Verlag, Berlin, 1985).
86. C. Makochekanwa, *et al.*, New J. Phys. **11**, 103036 (2009). “Total and positronium

formation cross sections for positron scattering from H_2O and HCOOH."

87. F. Arretche, K.T. Mazon, S.E. Michelin, M.M. Fujimoto, I. Iga, and M.T. Lee, Nucl. Instr. Meth. Phys Res. B **266**, 441 (2008). "Low energy elastic scattering of positrons by CO: An application of continued fractions and Schwinger variational iterative methods."
88. R. Zhang, K.L. Baluja, J. Franz, and J. Tennyson, J. Phys. B **44**, 035203 (2011). "Positron collisions with molecular hydrogen: cross sections and annihilation parameters calculated using the R-matrix with pseudo-states method."
89. M.P. Petkov, K.G. Lynn, and L.O. Roellig, J. Phys. Cond. Mat. **8**, L611 (1996). "Water-induced effects on the positron moderation efficiency of rare gas solids."
90. A.C.L. Jones, C. Makochekanwa, P. Caradonna, D.S. Slaughter, J.R. Machacek, R.P. McEachran, J.P Sullivan, S.J. Buckman, A.D. Stauffer, I. Bray, and D.V. Fursa, Phys. Rev. A **83**, 032701 (2011). "Positron scattering from neon and argon."
91. R.P. Lucht, S. Roy, T.A. Reichardt, Prog. Energy Comb. Sci. **29**, 115 (2003). "Calculation of radiative transition rates for polarized laser radiation."
92. R.C. Hilborn, Am. J. Phys. **50**, 982 (1982). "Einstein coefficients, cross sections, f-values, dipole moments, and all that."

DISTRIBUTION LIST

AFRL-RW-EG-TR-2012-096

*Defense Technical Info Center
8725 John J. Kingman Rd Ste 0944
Fort Belvoir VA 22060-6218

AFRL/RWME (6)
AFRL/RWOC-1 (STINFO Office)